Spatiotemporal transcriptome at single-cell resolution reveals key radial glial cell population in axolotl telencephalon development and regeneration

Xiaoyu Wei[1,18], Sulei Fu[2,3,18], Hanbo Li[1,4,5,18,*], Yang Liu[1,18], Shuai Wang[1,6,18], Weimin Feng[1,6,18], Yunzhi Yang[1,7,18], Xiawei Liu[4], Yan-Yun Zeng[2,3], Mengnan Cheng[1,6], Yiwei Lai[8], Xiaojie Qiu[9,10], Liang Wu[1,6], Nannan Zhang[4], Yujia Jiang[1,7], Jiangshan Xu[1,6], Xiaoshan Su[4], Cheng Peng[2,3], Lei Han[1,11,12], Wilson Pak-Kin Lou[2,3], Chuanyu Liu[1,12], Yue Yuan[1,6], Kailong Ma[1], Tao Yang[1], Xiangyu Pan[2], Shang Gao[4], Ao Chen[1,13], Miguel A. Esteban[8,14], Huanming Yang[1,15], Jian Wang[1,15], Guangyi Fan[1], Longqi Liu[1,12], Liang Chen[16,*], Xun Xu[1,17,*], Ji-Feng Fei[2,*], Ying Gu[1,6,17,19*]

[1]BGI-Shenzhen, Shenzhen 518103, China.
[2]Department of Pathology, Guangdong Provincial People's Hospital, Guangdong Academy of Medical Sciences, Guangzhou 510080, China.
[3]Key Laboratory of Brain, Cognition and Education Sciences, Ministry of Education; Institute for Brain Research and Rehabilitation, South China Normal University, Guangzhou 510631, China.
[4]BGI-Qingdao, Qingdao 266555, China.
[5]Lars Bolund Institute of Regenerative Medicine, Qingdao-Europe Advanced Institute for Life Sciences, BGI-Qingdao, Qingdao 266555, China.
[6]College of Life Sciences, University of Chinese Academy of Sciences, Beijing 100049, China.
[7]BGI College, Zhengzhou University, Zhengzhou, China.
[8]Laboratory of Integrative Biology, Guangzhou Institutes of Biomedicine and Health, Chinese Academy of Sciences, Guangzhou 510530, China.
[9]Whitehead Institute for Biomedical Research Cambridge, MA 02142, USA.
[10]Howard Hughes Medical Institute, Massachusetts Institute of Technology, Cambridge, MA 02139, USA.
[11]Shenzhen Key Laboratory of Single-Cell Omics, BGI-Shenzhen, Shenzhen 518120,

China.
[12]Shenzhen Bay Laboratory, Shenzhen 518000, China.
[13]Department of Biology, University of Copenhagen, Copenhagen DK-2200, Denmark.
[14]Institute of Stem Cells and Regeneration, Chinese Academy of Sciences, Beijing 100101, China.
[15]James D. Watson Institute of Genome Sciences, Hangzhou 310058, China.
[16]Hubei Key Laboratory of Cell Homeostasis, RNA Institute, College of Life Sciences, Wuhan University, Wuhan, 430072, China.
[17]Guangdong Provincial Key Laboratory of Genome Read and Write, Shenzhen 518120, China.
[18]These authors contributed equally to this work.
[19]Lead contact.

*Correspondence: guying@genomics.cn (Y.G.), jifengfei@gdph.org.cn (J.F.F.), xuxun@genomics.cn (X.X.), liang_chen@whu.edu.cn (L.C.), lihanbo@genomics.cn (H.L.).

SUMMARY

Brain regeneration requires a precise coordination of complex responses in a time- and region-specific manner. Identifying key cell types and molecules that direct brain regeneration would provide potential targets for the advance of regenerative medicine. However, progress in the field has been hampered largely due to limited regeneration capacity of the mammalian brain and understanding of the regeneration process at both cellular and molecular level. Here, using axolotl brain with extrodinary regeneration ability upon injury, and the SpaTial Enhanced REsolution Omics-sequencing (Stereo-seq), we reconstructed the first architecture of axolotl telencephalon with gene expression profiling at single-cell resolution, and fine cell dynamics maps throughout development and

56 regeneration. Intriguingly, we discovered a marked heterogeneity of radial glial cell (RGC)
57 types with distinct behaviors. Of note, one subtype of RGCs is activated since early
58 regeneration stages and proliferates while other RGCs remain dormant. Such RGC
59 subtype appears to be the major cell population involved in early wound healing response
60 and gradually covers the injured area before presumably transformed into the lost
61 neurons. Altogether, our work systematically decoded the complex cellular and molecular
62 dynamics of axolotl telencephalon in development and regeneration, laying the foundation
63 for studying the regulatory mechanism of brain regeneration in the future.

64 **INTRODUCTION**

65 Brain is the most complex organ that controls emotion, memory, learning and many other
66 functions, the brain in mammals, including human, has very limited regeneration
67 capability, which even declines along development (Diotel et al., 2020; Kaslin et al., 2008;
68 Tanaka and Ferretti, 2009), making researches or efforts on repairing of the injured brain
69 extremely challenge. In contrast, some lower vertebrates such as teleost fish and
70 salamanders preserve great ability of tissue regeneration (Joven and Simon, 2018;
71 Kroehne et al., 2011; Lust and Tanaka, 2019; Maden et al., 2013). Among them, axolotl
72 (*ambystoma mexicanum*), a tetrapod salamander species has been extensively studied
73 (Amamoto et al., 2016; Echeverri and Tanaka, 2002; Gerber et al., 2018; Li et al., 2021a;
74 Maden et al., 2013). Over a hundred years ago, the first forebrain regeneration in axolotls
75 was observed in larvae (Burr, 1916). Similar regeneration phenotypes were documented
76 as well in sex matured (adult) axolotls after removal of a large proportion of
77 telencephalons (Amamoto et al., 2016; Maden et al., 2013). Amazingly, recent studies

78 revealed that all lost cortical cell types, including neurons, could be reproduced at the
79 lesion (Amamoto et al., 2016). As the telencephalon anatomy in axolotls and some other
80 related salamander species is similar to that in mammals from the evolutionary point of
81 view (González et al., 2017; Joven and Simon, 2018), in which the ventricular neural stem
82 cells (NSCs) and neurons are located adjacent to the central lumen and peripheral pial
83 surface respectively, Therefore, axolotls serve as an excellent models for studying the
84 brain, in particular cortex regeneration, the discoveries of which may provide important
85 insights in understanding the regeneration process in mammals.

86 Previous studies in varied regenerative species including axolotls have shown that
87 ventricular radial glia cells (RGCs) respond to injury and contribute to brain regeneration
88 (Berg et al., 2010; Joven and Simon, 2018; Kirkham et al., 2014). RGCs in adult
89 salamanders are essentially the ancestor cells that give rise to nearly all cell types in the
90 brain during early embryonic development (Merkle et al., 2004; Todd E. Anthony, 2004),
91 and are maintained in the ventricular zone (VZ) (González et al., 2017). In contrast, most
92 NSCs in mammals, except those in subventricular zone and hippocampal dentate gyrus,
93 are almost completely consumed once the brain development is established. Under
94 homeostatic state, dividing RGCs are sparsely located along the entire telencephalic VZ
95 in axolotls, but only in a few confined VZ regions in red spotted newts. There are two
96 groups of RGCs identified in telencephalon in red spotted newt, slow dividing and
97 transient amplifying RGCs. The first group represents stem cell-like population, which
98 express(Joven and Simon, 2018; Joven et al., 2018). Glial fibrillary acidic protein (GFAP)
99 and glutamine synthetase, and show BrdU label-retaining property; the second group is
100 located at the proliferative hot spots in VZ and frequently divide (Kirkham et al., 2014).

101 Upon injury, RGCs can be reactivated and expanded to broader areas in VZ. While both
102 RGC groups could be detected close to lesion in red spotted newt, whether and how they
103 contribute to brain regeneration is not clear (Kirkham et al., 2014; Maden et al., 2013). So
104 far, only a few molecular signaling pathways that activate RGC and contribute to brain
105 regeneration have been identified from salamanders and fish, such as Notch, FGF, and
106 Gata3 (Kirkham et al., 2014; Kishimoto et al., 2012; Kizil et al., 2012). Interestingly, these
107 signals are generally involved in brain development, implying that brain development and
108 regeneration may share similarity in molecular regulation. Further investigation of this
109 possibility and deeper understanding of brain regeneration requires more advanced
110 technologies for systematic characterization of cell dynamics and the molecular
111 expression in each cell type.

112 Many methods distinct in capturing strategy, resolution, and throughput, have been
113 recently developed to obtain spatially resolved transcriptomic profiles of individual cells in
114 a given tissue (Chen et al., 2021; Chen et al., 2015; Eng et al., 2019; Lubeck et al., 2014;
115 Marx, 2021; Rodriques et al., 2019; Ståhl et al., 2016). However, one of the major
116 technical challenges in the field is how to accurately assign a sequencing area to the
117 physical location of each cell. Considering the complexity of the brain structure in general,
118 well-defining of single cells will be essential to promote data accuracy and new
119 discoveries. Mapping of the mouse brain or human cortex with spatial transcriptomics has
120 been reported previously using barcoded slides (Maynard et al., 2021; Ortiz et al., 2020),
121 but the resolution of these maps is limited by the diameters of the sequencing spots (100
122 μm or 55 μm, respectively). Data at such a resolution can only provide the average
123 expression profiling for a mixture of over dozens of cells, which encumbers detailed

124 investigation in regions with subtle networks of different cell types and molecular signals.
125 In addition, the sequential fluorescence *in situ* hybridization (seqFISH+) (Eng et al., 2019)
126 and multiplexed error-robust FISH (MERFISH) (Xia et al., 2019) have been developed for
127 spatial profiling of gene expression of single cells, but their application may be restricted
128 by the relative low throughput and the requirement of special equipment.

129 Taking advantages of a newly developed spatial-temporal transcriptomics
130 approach—SpaTial Enhanced REsolution Omics-sequencing (Stereo-seq) (Chen et al.,
131 2021) with the highest profiling resolution to date, we report here a *in situ* single-cell gene
132 expression atlas and global cell dynamics in axolotl forebrain throughout development
133 and the injury induced regeneration. We further identified the major brain RGCs
134 participating in the pallium regeneration and establish molecular programs potentially
135 involved in the activation of these cells and discovered presumably similar cell fate
136 transition between telencephalon development and regeneration. Overall, our study
137 provides comprehensive data sources for future investigation of the cellular and molecular
138 mechanisms of brain regeneration.

139 RESULTS

140 Establishment of spatial transcriptome profile of axolotl brain at single-cell 141 resolution

142 To first identify the individual cell types with precise location and transcriptome
143 information in axolotl telencephalon, we prepared frozen sections of the adult axolotl
144 telencephalon, followed by the Stereo-seq analysis on the entire section simultaneously

145 (Chen et al., 2021) (Figure 1A). Considering the size of the axolotl cells (Herrick, 1948;
146 Roth and Walkowiak, 2015; Westhoff and Roth, 2002), we collected coronal brain
147 sections at 20 μm thickness to capture roughly a single-cell layer. As the Stereo-seq is
148 based on DNA nanoball (DNB) sequencing technology (Porreca, 2010), for which each
149 DNB spot on the chip is 220 nm in diameter and the center-to-center distance of two
150 adjacent spots is 500 or 715 nm, we were able to capture transcripts at sub-cellular level
151 (Figure 1A and Figure S1A).

152 We then attempted to define single cells on tissue sections by taking the advantage
153 of the nucleic acid staining on cryosections to highlight the nucleus (Figure 1B), in which
154 freshly transcribed mRNAs undergoing mRNA processing, including intron splicing are
155 enriched (Gaidatzis et al., 2015; Gray et al., 2014; Zeisel et al., 2011). Indeed, intron-
156 containing unspliced-transcript enriched areas overlapped nicely with stained nucleic acid
157 signals, but are separated from spliced-transcript covered regions (Figure 1B, left panels),
158 suggesting that the image of nucleic acid staining can be used to define the nucleus
159 region. Inspired by this fact, we further employed watershed algorithm to our stereo-seq
160 data to isolate the transcriptome in each DNA-staining defined area (Figure 1B, right
161 panels), thus generating the spatial transcriptomic atlas of axolotl telencephalon at single-
162 nucleus resolution. Each nucleus contains about 850 DNB spots, 6297 UMIs and 1682
163 genes on average (Table S1 and Figure S3 A-B). This high-resolution tool empowers us
164 to delicately investigate diverse expression patterns of critical genes, with high similarity
165 to *in situ* hybridization results (Figure S1B).

166 Using these data, we first performed unsupervised clustering analysis that considers
167 both physical positions and global gene expression of individually deduced nucleus
168 (details in methods). In total, we obtained six clusters of cells that show a patterned
169 distribution on the brain section (Figure 1C), consistent with previous anatomical
170 characterization of axolotl telencephalon, including ventricular zone (VZ), dorsal pallium
171 (DP), medial pallium (MP), lateral pallium (LP), striatum and septum (González et al.,
172 2017; Joven and Simon, 2018; Lazcano et al., 2021). To comprehensively dissect the cell
173 type composition in the entire brain section, we next conducted unsupervised clustering
174 analysis solely based on gene expression with Seurat (v4.0.2) (Hao et al., 2021). To this
175 end, we categorized all identified nucleus into 15 cell types (Figure 1D) and further
176 mapped them onto the telencephalon section according to the spatial information of each
177 cell (Figure 1E). Cell identities were then determined by known marker genes in other
178 species (Figure S2A; Table S2), and the spatial location of each cell type was further
179 confirmed with the marker gene distribution results, which show great similarity to *in situ*
180 hybridization (ISH) data (Figure S2B). For example, Stereo-seq based expression of
181 classical excitatory neuron marker *Neurod6*, inhibitory neuron marker *Gad1* and RGC
182 marker *Gfap* are almost identical to *in situ* hybridization results (Figure 1F).

183 As expected, all major brain cell types are present in distinct locations (Figure 1E
184 and Figure S3C-E). Of note, there are three types of excitatory neurons enriched in
185 pallium, named as dorsal pallium excitatory neuron (DPEX), medial pallium excitatory
186 neuron (MPEX) and *Nptx*$^{+}$ lateral pallium excitatory neuron (NPTXEX); In contrast, four
187 types of inhibitory neurons, including striatum inhibitory neuron (StriatumIN), *Scgn*$^{+}$
188 inhibitory neuron (SCGNIN), medium spiny neuron (MSN) and basket cell (BKC) are

189 enriched in striatum or septum regions, physically separated from regions of excitatory
190 neurons (Figure 1E). Remarkably, a fifth type of inhibitory neurons, *Sst*$^{+}$ inhibitory neuron
191 (SSTIN), were individually dispersed within the pallium regions, intermingled with
192 excitatory neurons (Figure 1G and Figure S3E), consistent with previous study that *Sst*
193 was expressed in scattered cells across DP and MP (Amamoto et al., 2016). Again, such
194 exquisite distinction of cell types in space strongly endorsed the capability of Stereo-seq
195 in realizing spatial transcriptome profiling of individual nuclei.

196 During brain development, neurons are formed by differentiation of neuron stem cells,
197 or RGCs specifically for axolotl, which are also believed as the major contributing cell
198 population for regeneration (Maden et al., 2013; Noctor et al., 2001). While it is known
199 that axolotl RGCs mostly reside in the VZ region, we identified three clusters of cells
200 located separately along the VZ regions with commonly high expression level of RGC
201 specific markers genes, including *Sox2*, *Gfap*, *Nes*, *Vim*, *Fabp7* and *Slc1a3* (Figure S4),
202 therefore named as *Wnt*$^{+}$ radial glial cell (WNTRGC) along the medial pallium side, *Sfrp1*$^{+}$
203 radial glial cell (SFRP1RGC) and *Ccnd1*$^{+}$ radial glial cell (CCND1RGC) according to their
204 unique marker gene expression (Figure 1E). The distinct gene expression profile of each
205 RGC type may suggest discrete functions. Indeed, CCND1RGCs highly express *Nes,*
206 *Sox2,* cell cycle and ribosome related genes (Figure S2A; Table S2), suggesting they are
207 potentially the progenitor cells for adult axolotl telencephalon maintenance (Barna, 2013;
208 Bernal and Arranz, 2018; Calegari et al., 2005; Eming et al., 2014; Niu et al., 2015).

209 Other cell types identified included cholinergic, monoaminergic and peptidergic
210 neuron (CMPN) and telecephalic neuroblast (NBL) in the septum, choroid plexus cells

211 (CP) and vascular leptomeningeal cells in the out layer of the section (VLMC) (Figure 1E
212 and Figure S2A). Altogether, with high-resolution stereo-seq, we provide a spatial cell
213 atlas of axolotl telencephalon and transcriptome information for each cell, laying a cellular
214 and molecular foundation for further development and regeneration studies. The
215 interactive data portal can be browsed at https://db.cngb.org/stomics/artista.

216 **Cellular dynamics of RGCs throughout axolotl telencephalon development**

217 It has been reported that in axolotls, RGCs in VZ region are responsible for brain
218 development and regeneration, up on receiving stage-dependent developmental and
219 injury cue (Amamoto et al., 2016; Maden et al., 2013). To more comprehensively
220 understand cellular dynamics occurred during axolotl brain development, we carried out
221 a series of spatial transcriptome analyses on sections of developmental (stage 44, 54,
222 and 57), juvenile, adult, and metamorphosed axolotl forebrains (Figure 2A). Unsupervised
223 clustering analysis based on gene expression with Seurat was applied to each section
224 and in total 33 cell types were annotated coordinately across sections by their
225 differentially expressed marker genes (Figure 2A, Figure S5A-C and S6; Table S1 and
226 Table S2). In addition to the cell types identified in adult telencephalon (Figure 1), we also
227 discovered 14 immature/intermediate cell types containing marker genes of both
228 progenitor and differentiated cells (Figure 2A-B).

229 Most notably, we found a subpopulation of RGCs present in dominance throughout
230 developmental stages, but were decreased in number and disappeared after juvenile
231 stage (Figure 2A-B and Figure S7-S11). They expressed embryonic markers such as
232 *Fzd5* and *Sox1*, and were named as development related RGCs (DRGCs). SFRP1RGCs,

233 WNTRGCs and CCND1RGCs defined in adult telencephalon started to be detected since
234 stage 54 and gradually became dominant RGC populations in designated locations from
235 juvenile stage (Figure 2A-B). Along with DRGCs, immature neurons that expressed
236 neuron lineage markers and *Stmn2*, *Tubb6, Dcx* were also detected at early
237 developmental stages, the number of which progressively declined from stages 44 to 57
238 (Figure 2A-B and Figure S7-S11). Interestingly, the developmental intermediate
239 progenitor cells (DIPCs) that co-expressed both RGC and immature neuron markers were
240 discovered with similar temporal pattern as DRGCs and immature neurons (Figure 2A-B
241 and Figure S7-S11), confirming the potential cell transition from RGCs to immature
242 neurons as previously suggested (Noctor et al., 2001). In contrast to these developmental
243 cell types, mature neurons, including subtypes of excitatory neurons and inhibitory
244 neurons were gradually enriched, and the total number was increased from juvenile stage
245 (Figure 2A-B and Figure S7-S11). This result nicely recapitulates the cellular dynamics of
246 telencephalon development reported previously (Joven and Simon, 2018), suggesting
247 that neurogenesis of axolotl telencephalon massively declines from juvenile stage, after
248 which inactive SFRP1RGCs and WNTTGCs become WNTRGC made up the dominant
249 population of RGCs, while DRGCs like CCND1RGCs only took up a small portion.

250 To further characterize the stemness and proliferation activity of RGCs in different
251 VZ regions along the development, we analyzed the expression level of composite gene
252 modules defining neural stemness, cell cycle and translation activity (methods, Table S3),
253 all of which can help reveal the diverse aspects of stem cells (Figure 2C) (Fu et al., 2021;
254 Temple, 2001). Overall, cells expressing high level of three gene modules were basically
255 overlapped, distributed around the VZ, yet extended to the peripheral regions during early

256 developmental stages, consistent with the fact of fast expansion of the brain size yet less
257 neuron maturation in axolotl (Figure 2C) (Schreckenberg and Jacobson, 1975). Started
258 from juvenile stage, cells positive for neural stemness, cell cycle and translation module
259 gene expression significantly dropped in number and became restricted to the VZ region.
260 Eventually, these active progenitor cells were enriched to the ventral area of the VZ region
261 in adult, suggesting cells in this areas are responsible for adult brain maintenance similar
262 to previous reports (Maden et al., 2013).

263 In contrast to the axolotl, the mouse has very limited regenerative ability upon brain
264 cortex injury. To gain more insights into the molecular differences in stem cells between
265 the axolotl and mouse brain, we compared the cellular and molecular dynamics of NSCs
266 in mouse to that of RGCs in developing axolotl brains. Previously published single-cell
267 RNA-seq data of developing mouse neocortex from Paola Arlotta lab were integrated with
268 Stereo-seq data of developing axolotl telencephalons via Seurat (Figure S12 A-B) (Di
269 Bella et al., 2021). Identified mouse NSCs and the combination of RGCs and DIPCs in
270 axolotl were then compared. Interestingly, RGCs were relatively abundant in the VZ of
271 axolotl brains, and their ratio sustained roughly even in adulthood (Figure 2D). Moreover,
272 axolotl RGCs constantly expressed neural stemness module throughout the entire
273 developmental and adult stages (Figure 2E). In contrast, NSCs in mouse brain gradually
274 declined at later embryonic stages as well as after birth, accompanied with the degressive
275 activity of neural stemness module (Figure 2D-E). These differences including the number
276 and regeneration potential of stem cells between axolotl and mouse may partially explain
277 the high regenerative capability of axolotl brains, which is absent in adult mammals.

278 **Injury specific RGCs contribute to pallium regeneration in axolotl**

279 While axolotls harbor amazing regenerative capacity of the brain upon injury (Amamoto
280 et al., 2016), the type of cells and their origins, as well as the underlying molecular events
281 that direct the regeneration process and rebuild the exon network to recover the function
282 are largely unknown. We next applied Stereo-seq to dissect the cellular and molecular
283 dynamics during brain regeneration. Using a brain regeneration model established
284 previously (Amamoto et al., 2016), in which a reproducible portion of the dorsal pallium in
285 left telencephalic hemisphere of 11 cm length axolotl was removed by surgery, we
286 collected brain tissues at 2, 5, 10, 15, 20, 30 and 60 days post injury (DPI) for Stereo-seq
287 analysis, respectively (Figure 3A). Such efforts allowed us to investigate both immediate
288 wound responses and chronic tissue regeneration process. By unsupervised clustering
289 analysis based on gene expression with Seurat to each section (Figure S13A-D), we
290 annotated cell types coordinately across sections by marker genes used in the
291 developmental analysis (Figure S14). In total, 23 clusters were identified, including injury-
292 specific cell populations that were not present during development (Figure 3A and Figure
293 S13D). In line with previous reports that the injured site can be recovered to undetectable
294 level in morphology in about 4 to 5 weeks (Amamoto et al., 2016), our data further
295 revealed both cell types and their spatial distribution were basically recovered at 60 DPI
296 in comparison with uninjured and the intact lateral side of injured brains (Figure 3A and
297 Figure S13D).

298 Interestingly, we captured a new type of RGC enriched at the edge of wound region,
299 but not in the intact right side of telencephalon sections from 2 to 20 DPI (Figure 3A-B

300 and Figure S15A-B). This injury specific RGCs featured the high expression level of
301 genes, such as *Nes, Krt18, Tnc and Ccna2* (Figure 3A-B and Figure S15C; Table S2),
302 which indicate their stem cell state and high proliferation activity, and we therefore named
303 this RGC type as reactivate RGCs (REARGCs). Strikingly, the number of REARGCs
304 appeared to be significantly increased in the VZ along the medium and lateral pallium
305 region and eventually covered the whole wound area around 20 DPI, and disappeared
306 after 30 DPI (Figure 3B, Figure S13D and Figure S16-S22). Unlike brain wound healing
307 process in mammals, during which microglias and macrophages are the first line of cell
308 types responsible for injury site filling (Li et al., 2021b), REARGCs appeared to be the
309 dominant cell type in the wound area between 2 and 20 DPI, suggesting they may be
310 involved in multiple aspects of tissue regeneration process (Figure 3A-B).

311 Indeed, the detailed transcriptome examination of REARGCs from 2 to 20 DPI
312 showed two waves of functional module induction. The first is early and transient
313 expression of wound response related genes (Module 1), including *Tgfbi, Runx1, Tnc,*
314 *Cxcr4* and *Hmox1* at 2 DPI at the wound edge, which were rapidly downregulated
315 thereafter (Figure 3C-D). the second wave featured by continuous induction of
316 proliferation related genes (Module 2) in REARGCs from 10 to 20 DPI when REARGCs
317 and immature NPTXEXs expanded in number (Figure 3C-D and Figure S13D; Table S4).
318 The proliferation feature of REARGCs was further confirmed by EDU staining on sections
319 of 10 DPI and 15 DPI, which showed significant enrichment of EDU positive cells
320 extended from injury site along the VZ region, in comparison with uninjured site (Figure
321 3E). In contrast, other RGC types retained a moderate and constant expression level of
322 cycling related genes on average throughout regeneration stages. Altogether, our findings

323 here suggest that REARGCs may play dual roles in both early inflammatory response to
324 the wound and then switch to cell propagation to cover the injured region.

325 **Cellular dynamics from REARGCs to NPTXEXs in injury-induced pallium**
326 **regeneration**

327 The above results elicit an intriguing hypothesis that REARGCs, but not other RGCs, are
328 the major progenitor cell population that differentiates and restores lost neurons,
329 particularly NPTXEXs. If so, we would expect to capture cell clusters that are between
330 REARGCs and NPTXEXs in terms of differentiation state. To better test the hypothesis
331 and to avoid that our fine sectioning procedure may not capture all types of cells within a
332 single section, we chose to dissect the regenerating telencephalon at 15 DPI along the
333 rostral-caudal axis and made three more consecutive sections from wound center
334 towards the caudal direction in addition to the 15 DPI-1 section shown in Fig 3, including
335 one on the wound edge and two more sections at the closed area for stereo-seq analysis
336 (Figure 4A).

337 By combining data of all four sections, a total of 25 cell types were identified (Figure
338 4A, Figure S23A-D and S24). NPTXEXs were the major cell population lost at the lesion
339 of the injured hemisphere compared to uninjured lateral side in 15 DPI-1 to 4 sections.
340 REARGCs covered the injury regions in all 4 sections (Figure 3A, Figure 4A and Figure
341 S23D). Interestingly, the NPTXEX population showed a high-to-low spatial gradient from
342 the remote regions in 15 DPI-4 section to the center of the injured area in 15 DPI-1 section
343 (Figure 3A, Figure 4A and Figure S23D), which is consistent with previous micro-CT
344 scanned axolotl regeneration data (Amamoto et al., 2016). These data suggested that the

345 reconstitution of lost neurons probably occurs in accompany with the conjunction of injury
346 edges, the process of which may initiate from the peripheral region towards the center of
347 incision.

348 We then explored how lost NPTXEXs were restored around the injury site. As
349 expected, the newly formed NPTXEXs in 15 DPI-4 section were nicely located adjacent
350 to immature NPTXEXs and REARGCs, suggesting a possible transition between these
351 cell types (Figure 4A). Excitingly, a regenerative specific cluster of cells were identified in
352 an intermediate state between REARGCs and immature NPTXEXs and therefore named
353 as regeneration intermediate progenitor cells 1 (RIPC1) (Figure 4A; Table S2). They
354 expressed both REARGC markers including *Vim*, *Nes*, *Krt18*, *S100a10* and immature
355 NPTXEX markers including *Ankrd1*, *Stmn4*, *Nptx1* (Figure 4B-C). Expression of cyclin
356 inhibitors *Cdkn1a* and *Cdkn1c* was upregulated in RIPC1 and further upregulated in
357 immature NPTXEXs compared to REARGCs (Dutto et al., 2015; Mademtzoglou et al.,
358 2018), suggesting the proliferation is slowing down along the potential transition axis of
359 REARGC-DIPC1-immature NPTXEX (Figure 4B-C). Thus, our data revealed four nicely
360 adjacent cell layers of REARGCs, RIPC1s, immature NPTXEXs, and mature NPTXEXs,
361 respectively (Figure 4D and Figure S25-S27), inspiring us with a potential linage transition
362 for neurogenesis.

363 Indeed, cell type based (Figure 4E) and pseudotime based (Figure 4F) RNA velocity
364 analyses on the 15 DPI-4 section also suggested a similar putative lineage transition from
365 REARGCs to RIPC1s, then to immature NPTXEXs and eventually NPTXEXs. Similar
366 observation was made on sections of 15 DPI-2 and -3, too (Figure S28A-C and Figure

367 S28 F-H). To dissect our velocity results in more details, we calculated the genes that
368 show patterned expression change along the pseudotime axis (Figure 4G, Figure S28D
369 and I), which were consistent with their gene function in the putative lineage transition,
370 such like the descending of *Nes* and the ascending of *Cdkn1c* (Figure 4H, Figure S28E
371 and J). In summary, our results imply a potential scenario that REARGCs proliferate to
372 cover the wounding site of injured axolotl telencephalon, then convert or differentiate into
373 RIPCs and eventually produce immature neurons and reconstruct the lost tissue.

374 **Comparison of the NPTXEX formation processes in development and regeneration**

375 The nicely ordered cell layer distribution and potential lineage transition discovered at
376 injury site are similar to those in the developmental brain, thus prompting us to further
377 compare these two processes. Notably, DRGCs, DIPCs and immature NPTXEXs arrayed
378 from VZ to pallium region were observed at as early as stage 44 (Figure 5B). When the
379 mature NPTXEXs appeared at stage 57, four nicely adjacent cell layers of DRGCs,
380 RIPC1s, immature NPTXEXs, and mature NPTXEXs were observed with high similarity
381 to that in 15 DPI-4 section (Figure 5A-B), indicating a possible recapitulation of NPTXEX
382 development during the injury-induced regeneration. To further test this possibility, all
383 types of RGCs in the dorsal left telencephalon from developmental stage 44, 54 and 57,
384 as well as 15 DPI-4 and control section in injury model were pooled, and applied to
385 correlation analysis. Indeed, the results showed the gene expression pattern of
386 REARGCs is mostly correlated with DRGCs in Stage 57, rather than other RGC types
387 from the same section (Figure 5C). In addition, the spatial expression heatmap of key
388 markers such as *Nes*, *Nptx1* and *Cdkn1c* are much alike between 15 DPI-4 and Stage 57

389 (Figure 4C, Figure 5D-E, Figure S29 A-C). The RNA velocity analysis has simulated
390 parallel lineage transition trajectories to generate NPTXEXs in developmental and
391 regenerative processes, from RGCs to IPCs to immature neurons to mature neurons
392 (Figure 4E, Figure 5F-H and Figure S29 A-C).

393 We further used potential DRGC to NPTXEX transition at Stage 57 to represent
394 developmental neurogenesis, and potential REARGC to NPTXEX transition of 15 DPI-4
395 to represent the regenerative neurogenesis, and comprehensively assess the molecular
396 dynamics of these two potential transition processes. We examined the gene expression
397 patterns in the four related cell types along each process, and classified eight groups of
398 gene expression patterns showing similar or opposite trends (Figure 5I; Table S5).
399 Pathway enrichment analysis on these patterned expressing genes revealed that in both
400 development and regeneration, pathways involved in neuronal differentiation, migration,
401 maturation, communication and synaptic activities were up-regulated. However,
402 pathways related to proliferation, cell cycle progression and factors promoting these
403 processes such as translation initiation, RNA splicing were both down-regulated (Figure
404 5J). These results fit the expected notion that the stemness and proliferation were
405 declined with the onset of neurogenesis (Figure 5J). Interestingly, protein ubiquitination,
406 chromatin organization, mTOR signaling and transcriptional regulation by TP53 were
407 found specifically upregulated in regeneration, suggesting possible immune and
408 metabolism strategies to control the rapid cell growth during regeneration. In addition, we
409 also observed a regeneration specific rise in activities of autophagy, as well as a
410 regeneration specific decline in activities of response to wound and stress (Figure 5J),
411 reflecting a possible transition of molecular machinery from wound response in REARGC

412 to neuron regeneration. Besides the enriched pathways, we also identified hundreds of
413 regenerative specific genes (Table S6). Overall, our data suggested that regeneration to
414 certain extent is the re-initiation of development, but also exhibits its unique features.
415 Though majority of them showed expression pattern as expected, such as *JunD* and *Tnc*
416 that are known to be involved in nervous system regeneration (Chen et al., 2010; Raivich
417 et al., 2004), several unexpected or functionally unknown genes were discovered, such
418 as filament reorganizational *Krt18*, protein phosphorylation related *S100a10*, tumor
419 suppressor *Tagln2* and *Tnfsf10*, and endothelial cell activator *Ankrd1* (Figure S30), which
420 may be interesting targets in following functional studies of brain regeneration.

421 Altogether, our detailed comparison of spatial transcriptomes revealed great
422 similarity in both spatial distribution and enriched molecular pathway between
423 development and regeneration, suggesting regeneration of axolotl brain may partially
424 recapitulate neurogenesis in brain development through differentiation of stem/progenitor
425 cells with similar molecular regulations.

426 **DISCUSSION**

427 **Dynamic cell atlas of axolotl telencephalon through development and regeneration**
428 **at single cell resolution**

429 The goal of regenerative medicine in the brain is to restore not only the intricate tissue
430 architecture and cell composition of the injured region, but also the molecular and cellular
431 homeostasis and functions of recovered brains. While we have learned much about the
432 natural regeneration process by studying various types of animal models, especially the
433 highly regenerative fish and axolotls, key questions including whether the brain of these

models can be fully regenerated both anatomically and functionally, how progenitor cells take the regenerative responsibility and how gene activity orchestrates cellular responses upon jury remain unanswered. To this end, a complete set of knowledge regarding the cellular and molecular profiling during development and regeneration in regenerative models is needed in the first place. Though a cellular map of the pallium has been previously built by *in situ* hybridization with a few marker genes in axolotls (Amamoto et al., 2016), more comprehensive cell type identification and their spatial organization and gene activity dynamics in the context of development and regeneration for mechanistic investigation is still lacking.

Taking the advantage of our Stereo-seq and the single nucleus extraction method developed in this study, we successfully established the first single cell level spatial-transcriptomic atlas of axolotl telencephalon, a marked advancement in resolution and throughput in comparison with the brain atlas data in previous studies (Maynard et al., 2021; Ortiz et al., 2020). The single cell level transcriptomics displayed on Stereo-seq sections also empowered us to elucidate the spatial-temporal relationship between diverse cell types in regeneration, between development and regeneration, the knowledge of which is essential but not yet clear. Furthermore, the large size of our stereo-seq chip allowed us to capture the entire telencephalon on the same section, with the left hemisphere injured but the right one uninjured for direct comparison. With these technical advantages, our data provided inspiring information to several important questions in brain regeneration, revealing the key cell populations and their dynamics in the regeneration niche, suggesting a possible strategy for lost tissue reconstitution by

456 lineage-transition from injury-specific RGCs, and elucidating that the injury-induced
457 regeneration partially recapitulate the neuron developmental hierarchy.

458 **Diversification of RGC subtypes in VZ region through development and**
459 **identification of transient activated RGCs involved in brain regeneration**

460 RGCs are thought to be ancestor cells that give rise to all cells in brain development
461 and maintained in the VZ region of adult amphibian, featuring by positive staining of BrdU
462 (Joven et al., 2018; Kirkham et al., 2014). Accordingly, four subtypes of RGCs are
463 identified in our study in normal axolotl telencephalon development and maturation.
464 DRGCs that are dominantly distributed along VZ during developmental stages, are shown
465 to be gradually substituted by three locally restricted RGC subtypes (Figure 2A-B),
466 indicating a possible lineage maturation trace of these endogenous neural progenitor cells.
467 Though a decrease of early embryonic markers, the three RGC subtypes in homeostasis
468 retained their feature of NSCs and cell cycle markers, which show similarity to the
469 ependymoglial cells and radial glial cells previously identified in newts and zebrafish,
470 respectively (Lust and Tanaka, 2019). In the red spotted newts, two types of
471 ependymoglial cells, quiescent type I ependymoglial cells and proliferating type II
472 ependymoglial cells, have been reported unevenly distributed along ventricle (Berg et al.,
473 2010; Kirkham et al., 2014). In contrast, we diversified the RGCs in hemostasis based on
474 a combination of whole transcriptome features with their specific localizations, instead of
475 mainly on proliferation status (Figure 2A), thus leading to different classification of RGCs
476 along VZ region. The CCND1RGC, one of the three RGC subtypes in homeostasis stages,
477 is characterized with high cycling gene expression. It is majorly distributed in the VZ

478 region adjacent to the dorsal pallium and to the bed nucleus of the stria terminalis region
479 defined as proliferative hot spots in other salamander species (Kirkham et al., 2014) (Berg
480 et al., 2010), raising the possibility that the CCND1RGCs may share similarity with
481 previously identified type II ependymoglial cells in these spots.

482 Upon injury, the amphibian brain regeneration is accomplished mainly by resident
483 RGCs/ependymoglial cells through activation and differentiation in response to
484 environmental cues (Berg et al., 2010; Joven et al., 2018; Kirkham et al., 2014), yet how
485 such sequential process is regulated and if other types of cells participate remains largely
486 elusive. By identification of the REARGC and presentation of its dynamic regenerative
487 function, our work not only support the injury-specific appearance of cells with elevated
488 proliferation capacity around the lesion sites (Amamoto et al., 2016; Kirkham et al., 2014),
489 but also indicate that these amplifying RGCs may serve as the cell origin of de novo
490 neurogenesis (Amamoto et al., 2016; Berg et al., 2010; Kirkham et al., 2014).

491 **Regeneration through REARGCs largely mimics early telencephalon development**
492 **with DRGC in axolotl**

493 More intriguingly, by comparing our regeneration and development data, it becomes
494 quite clear that REARGCs are in a state similar to DRGCs in terms of gene expression
495 profile and pathway enrichment (Figure 5C and 5J), such as the elevated expression of
496 translation related genes, the typical characteristic of stem cell undergoing active
497 proliferation (Baser et al., 2017). As DRGCs appear from the earliest stage of
498 development we sampled, and presumably give rise to other RGC types and neurons in
499 adulthood, it represents a more primitive type of stem cells with higher multipotency. On

500 the other hand, since DRGCs appear to be consumed in adulthood according to our data,
501 it is mostly likely that REARGCs are originated from resident adult RGCs by
502 reprogramming, though it remains to be determined which type of RGCs are activated
503 and reprogrammed to REARGCs.

504 As previously suggested, a few possible REARGC origins exist (Amamoto et al.,
505 2016; Berg et al., 2010; Kirkham et al., 2014). The first is the local WNTRGCs or
506 SFRP1RGCs at the lesion site that respond to injury and immediately converted to
507 REARGCs for early wound healing response; The second likely origin is CCND1RGCs,
508 which might be the previously defined proliferative hot spot RGCs responsible for brain
509 neuron maintenance in homeostasis state (Berg et al., 2010; Kirkham et al., 2014). It is
510 possible that REARGCs are directly converted from CCND1RGCs in the VZ region
511 adjacent to the dorsal pallium, where the incision takes place, or originate from ventral
512 CCND1RGCs migrating to the injury site within two days (Figure 3B), the evidence of
513 which requires further investigations. It is of note that at 10 and 15 DPI, more RGCs at
514 the wound area harbor high EdU labeling activity than that at the VZ region (Figure 3E),
515 suggesting REARGCs may locally replenish its own population, consistent with previous
516 reports (Amamoto et al., 2016). In any case, future VZ-region specific labeling or
517 functional perturbation assay are required to eventually elucidate how RGCs at different
518 regions function during regeneration.

519 **Comparison of molecular and cellular features between axolotl brain regeneration**
520 **and mammalian brain injury recovery**

521 Inflammation/immune-responses have been reported to be critical to lead to a
522 successful regeneration (Kyritsis et al., 2012). Unlike the axolotl, lesion in mammalian

523 adult brains often leads to tissue loss and cystic scar formation, with very limited functional
524 recovery (Hagberg et al., 2012). Only low-cycling/quiescent NSCs are identified in defined
525 areas of postnatal mammalian brains, and they are generally difficult to be activated to
526 give rise to proper cell types to repair brain lesion (Furutachi et al., 2015; Llorens-
527 Bobadilla et al., 2015; Yang et al., 2007). The pro-inflammatory molecules secreted at the
528 lesion following hypoxia insult are thought to be detrimental to neurogenesis in mammals,
529 and such negative effects are elevated by the long-term persistence of glial scar (Silver
530 and Miller, 2004). Interestingly, a transit wave of wound-response is also observed in
531 REARGCs at the edge of the lesion site during cortex regeneration, which represented
532 by the upregulation of inflammation and hypoxia related genes at 2 and 5 DPI (Figure 3C-
533 D). It suggests a similar early response in axolotl as those in mammalian system. In
534 contrast to the sustained inflammation in injured mammalian brain, REARGCs in the
535 injured axolotl pallium decrease their activity in wound-response and transform their
536 molecular features into proliferation around 10 DPI (Figure 3C-E), raising the possibility
537 that they may start to function as NSCs to initiate de novo neurogenesis, the process of
538 which is further proved by the nicely arranged cell layers re-exhibiting in the
539 developmental process (Figure 5). Based on these observations, we predicted that axolotl
540 REARGCs may play dual roles in injury-induced brain regeneration: firstly, respond to
541 early wound insults and then expand to reconstitute lost neurons. The injury-specific
542 REARGC population and the well-controlled transition between two functions may provide
543 key mechanism to balance inflammation versus neurogenesis, which endows axolotl the
544 capacity of neuronal regeneration.

545 In summary, our work provides the most comprehensive atlas of the axolotl
546 telencephalon to date. Such large-scale efforts not only prompt to redefine the
547 subpopulation of radial glial cells based on whole transcriptome feature, but also start to
548 reveal their dynamic transition and functions in development and regeneration with
549 significant similarity at molecular level. In the future, advanced technology with higher
550 resolution and RNA capture capability, as well as accurate cell membrane border
551 definition strategies, will enable the identification of cell types and transcript features in a
552 more accurate way. Moreover, as injury-induced regeneration would be joint behaviors in
553 different regions, including cells from the olfactory bulb, yet limitation may exist for full
554 recovery (Maden et al., 2013) (Amamoto et al., 2016). Therefore, it could be of great
555 interest in the future study to perform continues sections that enable 3D reconstruction of
556 multiple brain regions in a longer regeneration time, which would help display the
557 networks of neuron projections and connections during regeneration and to investigate
558 whether they are rebuild completely. 3D map can also let us investigate whether
559 molecular and cellular cues of regeneration are polarized along rostro-caudal axis.

560

561 **REFERENCES**

562

563 Altschul, S.F., Madden, T.L., Schäffer, A.A., Zhang, J., Zhang, Z., Miller, W., and
564 Lipman, D.J. (1997). Gapped BLAST and PSI-BLAST: a new generation of protein
565 database search programs. Nucleic acids research *25*, 3389-3402.
566 Amamoto, R., Huerta, V.G., Takahashi, E., Dai, G., Grant, A.K., Fu, Z., and Arlotta, P.
567 (2016). Adult axolotls can regenerate original neuronal diversity in response to brain
568 injury. eLife *5*.
569 Barna, M. (2013). Ribosomes take control. Proceedings of the National Academy of
570 Sciences of the United States of America *110*, 9-10.
571 Barton, R.A., and Harvey, P.H. (2000). Mosaic evolution of brain structure in mammals.
572 Nature *405*, 1055-1058.
573 Baser, A., Skabkin, M., and Martin-Villalba, A. (2017). Neural Stem Cell Activation and
574 the Role of Protein Synthesis. Brain Plast *3*, 27-41.
575 Berg, D.A., Kirkham, M., Beljajeva, A., Knapp, D., Habermann, B., Ryge, J., Tanaka,
576 E.M., and Simon, A. (2010). Efficient regeneration by activation of neurogenesis in

577 homeostatically quiescent regions of the adult vertebrate brain. Development *137*,
578 4127-4134.
579 Bernal, A., and Arranz, L. (2018). Nestin-expressing progenitor cells: function, identity
580 and therapeutic implications. Cellular and Molecular Life Sciences *75*, 2177-2195.
581 Bullmore, E., and Sporns, O. (2012). The economy of brain network organization.
582 Nature Reviews Neuroscience *13*, 336-349.
583 Calegari, F., Haubensak, W., Haffner, C., and Huttner, W.B. (2005). Selective
584 lengthening of the cell cycle in the neurogenic subpopulation of neural progenitor cells
585 during mouse brain development. The Journal of neuroscience : the official journal of
586 the Society for Neuroscience *25*, 6533-6538.
587 Chen, A., Liao, S., Cheng, M., Ma, K., Wu, L., Lai, Y., Yang, J., Li, W., Xu, J., Hao, S.*,*
588 *et al.* (2021). Large field of view-spatially resolved transcriptomics at nanoscale
589 resolution. bioRxiv, 2021.2001.2017.427004.
590 Chen, J., Joon Lee, H., Jakovcevski, I., Shah, R., Bhagat, N., Loers, G., Liu, H.Y.,
591 Meiners, S., Taschenberger, G., Kügler, S.*, et al.* (2010). The extracellular matrix
592 glycoprotein tenascin-C is beneficial for spinal cord regeneration. Mol Ther *18*, 1769-
593 1777.
594 Chen, K.H., Boettiger, A.N., Moffitt, J.R., Wang, S., and Zhuang, X. (2015). RNA
595 imaging. Spatially resolved, highly multiplexed RNA profiling in single cells. Science
596 (New York, NY) *348*, aaa6090.
597 Di Bella, D.J., Habibi, E., Stickels, R.R., Scalia, G., Brown, J., Yadollahpour, P., Yang,
598 S.M., Abbate, C., Biancalani, T., Macosko, E.Z.*, et al.* (2021). Molecular logic of cellular
599 diversification in the mouse cerebral cortex. Nature *595*, 554-559.
600 Diotel, N., Lübke, L., Strähle, U., and Rastegar, S. (2020). Common and Distinct
601 Features of Adult Neurogenesis and Regeneration in the Telencephalon of Zebrafish
602 and Mammals. Frontiers in neuroscience *14*, 568930.
603 Dobin, A., Davis, C.A., Schlesinger, F., Drenkow, J., Zaleski, C., Jha, S., Batut, P.,
604 Chaisson, M., and Gingeras, T.R. (2013). STAR: ultrafast universal RNA-seq aligner.
605 Bioinformatics *29*, 15-21.
606 Dutto, I., Tillhon, M., Cazzalini, O., Stivala, L.A., and Prosperi, E. (2015). Biology of the
607 cell cycle inhibitor p21(CDKN1A): molecular mechanisms and relevance in chemical
608 toxicology. Archives of toxicology *89*, 155-178.
609 Echeverri, K., and Tanaka, E.M. (2002). Ectoderm to mesoderm lineage switching
610 during axolotl tail regeneration. Science (New York, NY) *298*, 1993-1996.
611 Eming, S.A., Martin, P., and Tomic-Canic, M. (2014). Wound repair and regeneration:
612 mechanisms, signaling, and translation. Science translational medicine *6*, 265sr266.
613 Eng, C.-H.L., Lawson, M., Zhu, Q., Dries, R., Koulena, N., Takei, Y., Yun, J., Cronin, C.,
614 Karp, C., Yuan, G.-C.*, et al.* (2019). Transcriptome-scale super-resolved imaging in
615 tissues by RNA seqFISH+. Nature *568*, 235-239.
616 Font, E., Desfilis, E., Pérez-Cañellas, M.M., and García-Verdugo, J.M. (2001).
617 Neurogenesis and neuronal regeneration in the adult reptilian brain. Brain, behavior and
618 evolution *58*, 276-295.
619 Frackowiak, R.S.J. (2004). Introduction. In Human Brain Function (Second Edition),
620 R.S.J. Frackowiak, K.J. Friston, C.D. Frith, R.J. Dolan, C.J. Price, S. Zeki, J.T.
621 Ashburner, and W.D. Penny, eds. (Burlington: Academic Press), pp. xv-xvi.

Fu, J., Warmflash, A., and Lutolf, M.P. (2021). Stem-cell-based embryo models for fundamental research and translation. Nature Materials *20*, 132-144.
Furutachi, S., Miya, H., Watanabe, T., Kawai, H., Yamasaki, N., Harada, Y., Imayoshi, I., Nelson, M., Nakayama, K.I., Hirabayashi, Y.*, et al.* (2015). Slowly dividing neural progenitors are an embryonic origin of adult neural stem cells. Nat Neurosci *18*, 657-665.
Gaiano, N., Nye, J.S., and Fishell, G. (2000). Radial glial identity is promoted by Notch1 signaling in the murine forebrain. Neuron *26*, 395-404.
Gaidatzis, D., Burger, L., Florescu, M., and Stadler, M.B. (2015). Analysis of intronic and exonic reads in RNA-seq data characterizes transcriptional and post-transcriptional regulation. Nature biotechnology *33*, 722-729.
Gerber, T., Murawala, P., Knapp, D., Masselink, W., Schuez, M., Hermann, S., Gac-Santel, M., Nowoshilow, S., Kageyama, J., Khattak, S.*, et al.* (2018). Single-cell analysis uncovers convergence of cell identities during axolotl limb regeneration. Science (New York, NY) *362*.
González, A., López, J.M., Morona, R., and Moreno, N. (2017). The Organization of the Central Nervous System of Amphibians. In Evolution of Nervous Systems, pp. 141-170.
Gray, J.M., Harmin, D.A., Boswell, S.A., Cloonan, N., Mullen, T.E., Ling, J.J., Miller, N., Kuersten, S., Ma, Y.C., McCarroll, S.A.*, et al.* (2014). SnapShot-Seq: a method for extracting genome-wide, in vivo mRNA dynamics from a single total RNA sample. PloS one *9*, e89673.
Hagberg, H., Gressens, P., and Mallard, C. (2012). Inflammation during fetal and neonatal life: implications for neurologic and neuropsychiatric disease in children and adults. Ann Neurol *71*, 444-457.
Hansen, D.V., Lui, J.H., Parker, P.R.L., and Kriegstein, A.R. (2010). Neurogenic radial glia in the outer subventricular zone of human neocortex. Nature *464*, 554-561.
Hao, Y., Hao, S., Andersen-Nissen, E., Mauck, W.M., 3rd, Zheng, S., Butler, A., Lee, M.J., Wilk, A.J., Darby, C., Zager, M.*, et al.* (2021). Integrated analysis of multimodal single-cell data. Cell *184*, 3573-3587.e3529.
Herrick, C.J. (1948). The brain of the tiger salamander, Ambystoma tigrinum (Chicago, IL, US: University of Chicago Press).
Joven, A., and Simon, A. (2018). Homeostatic and regenerative neurogenesis in salamanders. Progress in neurobiology *170*, 81-98.
Joven, A., Wang, H., Pinheiro, T., Hameed, L.S., Belnoue, L., and Simon, A. (2018). Cellular basis of brain maturation and acquisition of complex behaviors in salamanders. Development (Cambridge, England) *145*.
Kaslin, J., Ganz, J., and Brand, M. (2008). Proliferation, neurogenesis and regeneration in the non-mammalian vertebrate brain. Philosophical transactions of the Royal Society of London Series B, Biological sciences *363*, 101-122.
Kirkham, M., Hameed, L.S., Berg, D.A., Wang, H., and Simon, A. (2014). Progenitor cell dynamics in the Newt Telencephalon during homeostasis and neuronal regeneration. Stem Cell Reports *2*, 507-519.
Kishimoto, N., Shimizu, K., and Sawamoto, K. (2012). Neuronal regeneration in a zebrafish model of adult brain injury. Disease models & mechanisms *5*, 200-209.

Kizil, C., Kyritsis, N., Dudczig, S., Kroehne, V., Freudenreich, D., Kaslin, J., and Brand, M. (2012). Regenerative Neurogenesis from Neural Progenitor Cells Requires Injury-Induced Expression of Gata3. Developmental cell *23*, 1230-1237.
Kroehne, V., Freudenreich, D., Hans, S., Kaslin, J., and Brand, M. (2011). Regeneration of the adult zebrafish brain from neurogenic radial glia-type progenitors. Development (Cambridge, England) *138*, 4831-4841.
Kumar, L., and M, E.F. (2007). Mfuzz: a software package for soft clustering of microarray data. Bioinformation *2*, 5-7.
Kyritsis, N., Kizil, C., Zocher, S., Kroehne, V., Kaslin, J., Freudenreich, D., Iltzsche, A., and Brand, M. (2012). Acute inflammation initiates the regenerative response in the adult zebrafish brain. Science (New York, NY) *338*, 1353-1356.
La Manno, G., Soldatov, R., Zeisel, A., Braun, E., Hochgerner, H., Petukhov, V., Lidschreiber, K., Kastriti, M.E., Lönnerberg, P., Furlan, A.*, et al.* (2018). RNA velocity of single cells. Nature *560*, 494-498.
Lazcano, I., Cisneros-Mejorado, A., Concha, L., Ortiz-Retana, J.J., Garza-Villarreal, E.A., and Orozco, A. (2021). MRI- and histologically derived neuroanatomical atlas of the Ambystoma mexicanum (axolotl). Sci Rep *11*, 9850.
Li, H., Wei, X., Zhou, L., Zhang, W., Wang, C., Guo, Y., Li, D., Chen, J., Liu, T., Zhang, Y.*, et al.* (2021a). Dynamic cell transition and immune response landscapes of axolotl limb regeneration revealed by single-cell analysis. Protein & cell *12*, 57-66.
Li, Z., Xiao, J., Xu, X., Li, W., Zhong, R., Qi, L., Chen, J., Cui, G., Wang, S., Zheng, Y.*, et al.* (2021b). M-CSF, IL-6, and TGF-β promote generation of a new subset of tissue repair macrophage for traumatic brain injury recovery. Science advances *7*.
Llorens-Bobadilla, E., Zhao, S., Baser, A., Saiz-Castro, G., Zwadlo, K., and Martin-Villalba, A. (2015). Single-Cell Transcriptomics Reveals a Population of Dormant Neural Stem Cells that Become Activated upon Brain Injury. Cell Stem Cell *17*, 329-340.
Lubeck, E., Coskun, A.F., Zhiyentayev, T., Ahmad, M., and Cai, L. (2014). Single-cell *in situ* RNA profiling by sequential hybridization. Nature methods *11*, 360-361.
Lust, K., and Tanaka, E.M. (2019a). A Comparative Perspective on Brain Regeneration in Amphibians and Teleost Fish. Dev Neurobiol *79*, 424-436.
Lust, K., and Tanaka, E.M. (2019b). A Comparative Perspective on Brain Regeneration in Amphibians and Teleost Fish. Dev Neurobiol *79*, 424-436.
Mademtzoglou, D., Asakura, Y., Borok, M.J., Alonso-Martin, S., Mourikis, P., Kodaka, Y., Mohan, A., Asakura, A., and Relaix, F. (2018). Cellular localization of the cell cycle inhibitor Cdkn1c controls growth arrest of adult skeletal muscle stem cells. eLife *7*.
Maden, M., Manwell, L.A., and Ormerod, B.K. (2013). Proliferation zones in the axolotl brain and regeneration of the telencephalon. Neural Dev *8*, 1.
Malcolm Maden, L.A.M.a.B.K.O. (2013). Proliferation zones in the axolotl brain and regeneration of the telencephalon. Neural development *8*.
Marx, V. (2021). Method of the Year: spatially resolved transcriptomics. Nature methods *18*, 9-14.
Maynard, K.R., Collado-Torres, L., Weber, L.M., Uytingco, C., Barry, B.K., Williams, S.R., Catallini, J.L., 2nd, Tran, M.N., Besich, Z., Tippani, M.*, et al.* (2021a). Transcriptome-scale spatial gene expression in the human dorsolateral prefrontal cortex. Nat Neurosci *24*, 425-436.

Maynard, K.R., Collado-Torres, L., Weber, L.M., Uytingco, C., Barry, B.K., Williams, S.R., Catallini, J.L., Tran, M.N., Besich, Z., Tippani, M.*, et al.* (2021b). Transcriptome-scale spatial gene expression in the human dorsolateral prefrontal cortex. Nature Neuroscience *24*, 425-436.

McHedlishvili, L., Mazurov, V., Grassme, K.S., Goehler, K., Robl, B., Tazaki, A., Roensch, K., Duemmler, A., and Tanaka, E.M. (2012). Reconstitution of the central and peripheral nervous system during salamander tail regeneration. Proceedings of the National Academy of Sciences of the United States of America *109*, E2258-2266.

Merkle, F.T., Tramontin, A.D., García-Verdugo, J.M., and Alvarez-Buylla, A. (2004). Radial glia give rise to adult neural stem cells in the subventricular zone. Proceedings of the National Academy of Sciences of the United States of America *101*, 17528-17532.

Niu, W., Zang, T., Smith, Derek K., Vue, Tou Y., Zou, Y., Bachoo, R., Johnson, Jane E., and Zhang, C.-L. (2015). SOX2 Reprograms Resident Astrocytes into Neural Progenitors in the Adult Brain. Stem cell reports *4*, 780-794.

Noctor, S.C., Flint, A.C., Weissman, T.A., Dammerman, R.S., and Kriegstein, A.R. (2001). Neurons derived from radial glial cells establish radial units in neocortex. Nature *409*, 714-720.

Ortiz, C., Navarro, J.F., Jurek, A., Martin, A., Lundeberg, J., and Meletis, K. (2020a). Molecular atlas of the adult mouse brain. Sci Adv *6*, eabb3446.

Ortiz, C., Navarro, J.F., Jurek, A., Märtin, A., Lundeberg, J., and Meletis, K. (2020b). Molecular atlas of the adult mouse brain. Science advances *6*, eabb3446.

Porreca, G.J. (2010). Genome sequencing on nanoballs. Nature biotechnology *28*, 43-44.

Qiu, X., Zhang, Y., Hosseinzadeh, S., Yang, D., Pogson, A.N., Wang, L., Shurtleff, M., Yuan, R., Xu, S., Ma, Y.*, et al.* (2021). Mapping Transcriptomic Vector Fields of Single Cells. bioRxiv, 696724.

Raichle, M.E., and Mintun, M.A. (2006). BRAIN WORK AND BRAIN IMAGING. *29*, 449-476.

Raivich, G., Bohatschek, M., Da Costa, C., Iwata, O., Galiano, M., Hristova, M., Nateri, A.S., Makwana, M., Riera-Sans, L., Wolfer, D.P.*, et al.* (2004). The AP-1 transcription factor c-Jun is required for efficient axonal regeneration. Neuron *43*, 57-67.

Rodriques, S.G., Stickels, R.R., Goeva, A., Martin, C.A., Murray, E., Vanderburg, C.R., Welch, J., Chen, L.M., Chen, F., and Macosko, E.Z. (2019). Slide-seq: A scalable technology for measuring genome-wide expression at high spatial resolution. Science (New York, NY) *363*, 1463-1467.

Roerdink, J.B.T.M., and Meijster, A. (2000). The Watershed Transform: Definitions, Algorithms and Parallelization Strategies. Fundamenta Informaticae *41*, 187-228.

Roth, G., and Walkowiak, W. (2015). The Influence of Genome and Cell Size on Brain Morphology in Amphibians. Cold Spring Harbor perspectives in biology *7*, a019075.

Schloissnig, S., Kawaguchi, A., Nowoshilow, S., Falcon, F., Otsuki, L., Tardivo, P., Timoshevskaya, N., Keinath, M.C., Smith, J.J., Voss, S.R.*, et al.* (2021). The giant axolotl genome uncovers the evolution, scaling, and transcriptional control of complex gene loci. Proceedings of the National Academy of Sciences of the United States of America *118*.

Schreckenberg, G.M., and Jacobson, A.G. (1975). Normal stages of development of the axolotl, Ambystoma mexicanum. Developmental biology *42*, 391-399.

Siebert, S., Farrell, J.A., Cazet, J.F., Abeykoon, Y., Primack, A.S., Schnitzler, C.E., and Juliano, C.E. (2019). Stem cell differentiation trajectories in Hydra resolved at single-cell resolution. Science (New York, NY) *365*.

Silver, J., and Miller, J.H. (2004). Regeneration beyond the glial scar. Nat Rev Neurosci *5*, 146-156.

Smith, K.M., Ohkubo, Y., Maragnoli, M.E., Rasin, M.R., Schwartz, M.L., Sestan, N., and Vaccarino, F.M. (2006). Midline radial glia translocation and corpus callosum formation require FGF signaling. Nat Neurosci *9*, 787-797.

Ståhl, P.L., Salmén, F., Vickovic, S., Lundmark, A., Navarro, J.F., Magnusson, J., Giacomello, S., Asp, M., Westholm, J.O., Huss, M.*, et al.* (2016). Visualization and analysis of gene expression in tissue sections by spatial transcriptomics. Science (New York, NY) *353*, 78-82.

Tanaka, E.M., and Ferretti, P. (2009). Considering the evolution of regeneration in the central nervous system. Nature Reviews Neuroscience *10*, 713-723.

Tasoulis, D.K., Plagianakos, V.P., and Vrahatis, M.N. (2006). Unsupervised clustering in mRNA expression profiles. Computers in biology and medicine *36*, 1126-1142.

Temple, S. (2001). The development of neural stem cells. Nature *414*, 112-117.

Todd E. Anthony, C.K., Gord Fishell, and Nathaniel Heintz (2004). Radial Glia Serve as Neuronal Progenitors in All Regions of the Central Nervous System. Neuron *41*, 881-890.

van der Walt, S., Schönberger, J.L., Nunez-Iglesias, J., Boulogne, F., Warner, J.D., Yager, N., Gouillart, E., and Yu, T. (2014). scikit-image: image processing in Python. PeerJ *2*, e453.

Westhoff, G., and Roth, G. (2002). Morphology and projection pattern of medial and dorsal pallial neurons in the frog Discoglossus pictus and the salamander Plethodon jordani. The Journal of comparative neurology *445*, 97-121.

Xia, C., Fan, J., Emanuel, G., Hao, J., and Zhuang, X. (2019). Spatial transcriptome profiling by MERFISH reveals subcellular RNA compartmentalization and cell cycle-dependent gene expression. Proceedings of the National Academy of Sciences of the United States of America *116*, 19490-19499.

Yang, Z., Covey, M.V., Bitel, C.L., Ni, L., Jonakait, G.M., and Levison, S.W. (2007). Sustained neocortical neurogenesis after neonatal hypoxic/ischemic injury. Ann Neurol *61*, 199-208.

Zeisel, A., Köstler, W.J., Molotski, N., Tsai, J.M., Krauthgamer, R., Jacob-Hirsch, J., Rechavi, G., Soen, Y., Jung, S., Yarden, Y.*, et al.* (2011). Coupled pre-mRNA and mRNA dynamics unveil operational strategies underlying transcriptional responses to stimuli. Molecular systems biology *7*, 529.

ACKNOWLEDGMENTS

This work was supported by the Guangdong Provincial Key Laboratory of Genome Read and Write (2017B030301011), the National Natural Science Foundation of China (32171289, 31970619) and the Innovative Research Group Program of Hubei Province (2020CFA017). Ji-Feng Fei was supported by the National Key R&D Program of China

(2019YFE0106700), the Natural Science Foundation of China (31970782), Project of Department of Education of Guangdong Province (2018KZDXM027), Key-Area Research and Development Program of Guangdong Province (2018B030332001, 2019B030335001) and Guangdong-Hong Kong-Macao-Joint Laboratory Program (2019B121205005).

AUTHOR CONTRIBUTIONS

X.W., G.Y., J.F.F., X.X., C.L. and H.L. conceived the idea; G.Y., J.F.F., X.X., C.L. and H.L. supervised the work; X.W., S.F., H.L. and J.F.F. designed the experiment; S.F. , X.L. and N.Z. performed the majority of the experiments with the help from M.C., J.J., J.X., Y.Z., P.L., X.S. and C.P.; X.W., Y.L., S.W., W.F. and Y.Y. performed data analysis; M.K. and T.Y. performed database construction; Y.L., X.Q., L.W., L.H., L.C., Y.Y., X.P., S.G., A.C., M.A.E., H.Y., J.W., G.F. and L.L. gave the relevant advice; H.L., Y.G., L.C., J.F.F. and X.W. wrote the manuscript with input from all authors. All other authors contributed to the work. All authors read and approved the manuscript for submission.

DECLARATION OF INTERESTS

Employees of BGI have stock holdings in BGI. All other authors declare no competing interests.

RESOURCE AVAILABILITY

Lead contact

Further information and requests for the resources and reagents may be directed to the corresponding author Ying Gu (guying@genomics.cn)

Material availability

All materials used for Stereo-seq are commercially available.

Data and code availability

830 All raw data generated by Stereo-seq have been deposited to CNGB Nucleotide
831 Sequence Archive (accession code: CNP0002068
832 (*https://db.cngb.org/search/project/CNP0002068*). Any additional information is available
833 from the corresponding authors upon reasonable request.

834 **METHODS**

835

836 **Animal care**

837 The d/d Strain of *Ambystoma mexicanum* used in this study was originally obtained from
838 Elly M. Tanaka laboratory (Research Institute of Molecular Pathology, Vienna Biocenter,
839 Vienna, Austria). Animals were housed and bred at 18-20°C in fresh water under standard
840 conditions. All relevant procedures of animal experiments were carried out in accordance
841 with the animal welfare legislation in China, with local approval from the Biomedical
842 Research Ethics Committee of Guangdong Provincial People's Hospital.

843

844 **Brain injury**

845 10-13cm juvenile axolotls were used for brain injury experiments. Axolotl brain injury was
846 performed as described previously (Amamoto et al., 2016). Briefly, animals were firstly
847 anesthetized in 0.03% ethyl-p-aminobenzoate solution (E1501, Sigma-Aldrich, St.Louis,
848 MO), followed by surgeries to create rectangular cranial skin/skull flaps and expose the
849 left telencephalon of each experimental animal using scalpels and spring scissors. Finally,
850 a square-shaped (size 0.5mm x 0.5mm) piece of dorsal telencephalon tissue was
851 removed for each animal to generate brain damage. To accurately determine the injury
852 site, the incisions were placed right in between the olfactory bulb and choroid plexus on
853 the left telencephalon of animals. After the injury, the cranial skin/skull flaps were restored
854 without suture.

855

856 **Tissue collection**

857 For stereo-seq cryosection, brain samples from three developmental stages (Stage 44,
858 stage 54, stage 57), juvenile, adult and metamorphosed animals, and seven regenerative
859 stages (2 days post injury (2 DPI), 5 DPI, 10 DPI, 15 DPI, 20 DPI, 30 DPI, 60 DPI) were

860 collected from ethyl-p-aminobenzoate anaesthetized d/d axolotls. Brain samples were
861 immediately snap-frozen in Tissue-Tek OCT (4583, Sakura, Torrance, CA) with liquid
862 nitrogen prechilled isopentane and then transferred to -80°C refrigerator for storage
863 before further operation. To minimize RNA degradation, the entire dissection procedure
864 was performed on ice, and the tissue collection was completed within 30 minutes.
865 For *in situ* hybridization and EdU detection, we collected additional brains from juvenile
866 and adult d/d axolotls for cryosection. Brain samples were first fixed with MEMFA for 3
867 days, then transferred into 30% sucrose prepared in 1× PBS for 24 hours and finally
868 embedded in Tissue-Tek OCT with dry-ice. The OCT blocks were stored in -80°C freezer
869 before cryosection.
870
871 **Tissue cryosection**
872 For cryosection collection, the working area of the freezing microtome (CM1950, Leica,
873 Wetzlar, Germany) were sequentially cleaned with RNase Zap (AM9780, Invitrogen,
874 Waltham, MA) and DPEC (40718, Sigma-Aldrich, St. Louis, MO)-treated water. After the
875 machine is completely dried, we set the machine temperature to -25°C for cryosection.
876 We collected 20-μm coronal cryosections for Stereo-seq, and 10-μm coronal cryosections
877 for *in situ* hybridization and EdU detection, according to manufactory's instructions.
878
879 **Stereo-seq tissue fixation and ssDNA staining**
880 For Stereo-seq cryosection collection, tissue sections were directly adhered to the Stereo-
881 seq chip surface. The sections on chips were incubated at 37°C for 3 minutes, followed
882 by methanol fixation for 30 minutes at -20°C. Then the sections on chips were stained
883 with nucleic acid dye (Thermo fisher, Q10212) for ssDNA visualization. Images of ssDNA
884 were acquired with a Ti-7 Nikon Eclipse microscope.
885
886 **Stereo-seq libraries construction**
887 Tissue sections placed on the chip were permeabilized using 0.1% pepsin (Sigma, P7000)
888 in 0.01 M HCl buffer and incubated at 37°C for 12 minutes. RNA released from the
889 permeabilized tissue and captured by the DNA nanoball (DNB) was reverse transcribed
890 at 42°C overnight. Tissue sections were digested with tissue removal buffer (10 mM Tris-

891 HCl, 25 mM EDTA, 100 mM NaCl, 0.5% SDS) at 37°C for 30 minutes after reverse
892 transcription. cDNA-containing chips were then subjected to Exonuclease I (NEB,
893 M0293L) treatment for 1 hour at 37°C and cDNAs were amplified with KAPA HiFi Hotstart
894 Ready Mix (Roche, KK2602). PCR reactions were conducted as follow: 95°C for 5
895 minutes, 15 cycles at 98°C for 20 seconds, 58°C for 20 seconds, 72°C for 3 minutes and
896 a final incubation at 72°C for 5 minutes. The concentrations of the resulting PCR products
897 were quantified by Qubit™ dsDNA Assay Kit (Thermo, Q32854). A total of 20 ng of DNA
898 were then fragmented with in-house Tn5 transposase at 55°C for 10 minutes, after which
899 the reactions were stopped by the addition of 0.02% SDS. Fragmentation products were
900 amplified with KAPA HiFi Hotstart Ready Mix. The reaction flow was: 1 cycle of 95°C 5
901 minutes, 13 cycles of (98°C 20 seconds, 58°C 20 seconds and 72°C 30 seconds) and 1
902 cycle of 72°C 5 minutes. PCR products were purified and used to generate DNB, then
903 sequenced (35 bp for read 1, 100 bp for read 2) on a MGI DNBSEQ-T1 sequencer.
904
905 ***In situ* hybridization**
906 Total cDNA was prepared using the RNA mixture from axolotl brain tissues at different
907 stages. Target genes were amplified with total cDNA as template, and synthesized
908 oligonucleotides harboring T7 promoter as primers. The PCR products were used as
909 template to synthesize Dig-labelled antisense RNA probes by *in vitro* transcription. The
910 *in situ* hybridization was performed on 10-μm axolotl brain coronal cryosection as
911 previously described (*Knapp et al., 2013*). Briefly, air-dried slides were washed by 0.1%
912 Tween in 1 × PBS for 5 minutes for three times, then by 0.3% Triton in 1 × PBS for 20
913 minutes at room temperature. For pre-hybridization, slides were immersed in
914 hybridization buffer (10% dextran, 5 × SSC, 50% formamide, 0.1% Tween, 1 mg/ml yeast
915 RNA, 100 μg/ml heparin, 1 x Denhardt's solution, 0.1% CHAPS and 5 mM EDTA) at 60°C
916 for at least 30 minutes. Then, slides were incubated in hybridization buffer containing 500
917 ng/ml antisense RNA probes at 60°C overnight. After hybridization, excessive RNA
918 probes were removed by washing twice with post-hybridization buffer (5 × SSC, 50%
919 formamide and 0.1% Tween) for 30 minutes at 60°C twice, followed by wash buffer (2 ×
920 SSC, 50% formamide and 0.1% Tween) for 30 minutes at 60°C. The slides were then
921 washed with 0.2 × SSC buffer (0.2 × SSC and 0.1% Tween) for 30 minutes at 60°C once

922 and room temperature once, followed by TNE buffer (10mM Tris pH7.5, 500 mM NaCl, 1
923 mM EDTA) for 10 minutes twice. Next, RNase A treatment was performed (Sigma, R4642)
924 in TNE buffer for 1 hour at 37°C. RNase A was removed by washing with TNE buffer for
925 10 minutes twice. For sample blocking, slides were incubated with MAB buffer (100 mM
926 maleic acid, 150 mM NaCl, 0.1% Tween and pH was adjusted to pH 7.5 with NaOH) for
927 5 minutes twice and 20 minutes once, followed by incubation with blocking buffer (Roche,
928 11096176001) at room temperature for 1 hour. Then sections were incubated with Anti-
929 DIG-AP fab antibody (Roche, 11093274910) prepared in blocking buffer overnight at 4°C.
930 Afterwards, slides were washed five times with MAB buffer for 10 minutes at room
931 temperature and once in freshly-prepared AP buffer (100 mM Tris pH 9.5, 50 mM $MgCl_2$,
932 100 mM NaCl and 0.1% Tween). Finally, we used BM purple (Roche, 11442074001)
933 substrate for signal visualization and the reaction was stopped with 1 mM EDTA in 1 ×
934 PBS. Primers used for antisense RNA probe synthesis are listed in Table S7.
935
936 **EdU labeling**
937 For *in vivo* cell proliferation detection during brain regeneration, a single pulse of EDU
938 (A10044, Thermo Fisher Scientific, Waltham, MA, 10 μg EdU per gram of body weight)
939 was intraperitoneally injected into animals 6 hours prior to sample collection. EdU
940 detection was performed according to the manufacturer's protocol of the Click iT Plus
941 EdU Alexa fluor 594 imaging kit (C10339, Thermo Fisher Scientific, Waltham, MA).
942
943 **Stereo-seq raw data processing**
944
945 Stereo-seq fastq files were generated from a MGI DNBSEQ-T1 sequencer. Read 1
946 contained CID and MID sequences (CID: 1-25bp, MID: 26-35bp), while read 2 contained
947 the cDNA sequence. Retained reads were then aligned to the reference genome
948 AmexG_v6.0 (Schloissnig et al., 2021) via STAR (Dobin et al., 2013). Mapped reads with
949 MAPQ ⩾ 10 were annotated, then calculated by handleBam (available at
950 https://github.com/BGIResearch/handleBam). Reads overlapped more than 50% with the
951 exon region were counted as exon transcripts. Reads overlapped less than 50% with the
952 exon region yet possess overlapped sequences with the adjacent intron sequence were

953 annotated as intron transcripts, otherwise as intergenic transcripts. UMIs with both the
954 same CID and gene locus was collapsed, and 1 base pair of mismatches to correct
955 sequencing was allowed for PCR errors. Finally, the exonic reads were used to generate
956 a CID-containing expression profile matrix.
957
958 **Circling method for single cell identification of Stereo-seq data**
959 The ssDNA images were used to identify the nuclei region via scikit-image python
960 package (version 0.18.1) (van der Walt et al., 2014). Global threshold was applied to filter
961 background noise and Gaussian-weighted local threshold was calculated to process gray
962 images into binary images, with block size of 41 and offset of 0.03. To segment cell nuclei
963 with overlapped regions, the exact Euclidean distance transformation was performed.
964 Labels representing different cell nuclei were transferred to pinpoint DNBs corresponding
965 to spatial positions by watershed algorithm (Roerdink and Meijster, 2000).
966
967 **Unsupervised spatially-constrained clustering of Stereo-seq data**
968 The raw count matrices of axolotl adult telencephalon samples were normalized by
969 SCTransform function in Seurat (v4.0.2) (Hao et al., 2021), and spatial information was
970 taken into consideration for unsupervised clustering by custom script. In brief, the mean
971 values of x-axis and y-axis on bins of each single-nuclei cell were calculated as single-
972 nuclei cell space coordinates. Spatial k-nearest neighbor graph $G_{spatial}^{k1}$ (k_1 = 6) was
973 built via Squidpy and then took the union with the k-nearest neighbor graph $G_{expression}^{k2}$
974 based on transcriptomic data (k_2 is by default set to be 30). The combined graph
975 ($G^{combined} = G_{spatial}^{k1} \cup G_{expression}^{k2}$) was then used as input for leiden clustering at
976 resolution of 0.5. The adult telencephalon brain regions were identified based on
977 anatomical structure (González et al., 2017; Lazcano et al., 2021).
978
979 **Single cell level clustering and annotation of Stereo-seq**
980 Reads captured by DNBs were summarized based on the results of cell segmentation to
981 obtain the single cell level gene expression matrices for downstream analysis. Nuclei with
982 UMIs number less than 200 were discarded. The raw count matrices were then
983 normalized by SCTransform function in Seurat (v4.0.2) to eliminate sequencing depth

984 effects. Reference-based integration was applied along with reciprocal PCA (RPCA) to
985 integrate all slides to avoid potential batch effects. Cluster analysis was performed by
986 FindClusters function in Seurat (v4.0.2) with resolution of 2. Clustering results were
987 displayed by uniform manifold approximation and projection (UMAP) dimension reduction
988 analysis. Major cell types were annotated based on marker gene sets. Visualization of
989 spatial plots in single-DNB resolution with cell boundary were performed by custom script.
990

991 **Gene Module analysis**

992 Gene module expression score was calculated to evaluate the expression level of
993 individual cells regarding predefined gene sets. Stemness, cell cycle *and* translation
994 scores of each cell were calculated by AddModuleScore function with default parameters
995 (ctrl = 100，nbin = 24) implemented in the Seurat (v4.0.2) R package (Hao et al., 2021),
996 with respective gene sets manually selected from GO, BIOCARTA, PID, REACTOME and
997 KEGG databases. The detailed gene lists can be found in Table S3.
998

999 **Construction of one-to-one orthologous between axolotl and mouse**

1000 To optimize the gene annotation of axolotl, a gene ortholog table was created with the
1001 mouse genome as the reference gene list. 46,581 axolotl protein coding genes were
1002 identified from the AmexG_v6.0 genome (Schloissnig et al., 2021). Mouse reference
1003 genome and GFF file (GRCm39) were downloaded from NCBI, the longest transcript of
1004 each mouse gene was picked by an in-house Perl script. From which, 22,173 mouse
1005 protein coding genes were identified. The orthologous genes were inferred using blastp
1006 (Altschul et al., 1997) of the axolotl proteins vs. the mouse proteins. As a result, 20,650
1007 one-to-one orthologous genes were identified between axolotl and mouse, which were
1008 used for functional annotation of axolotl in the follow-up analysis.
1009

1010 **Mouse data processing**

1011 To compare the expression of stemness related genes in developmental stages between
1012 axolotl and mouse, we used the published matrix data and metadata of mammalian
1013 cerebral cortex atlas from the Single Cell Portal
1014 (https://singlecell.broadinstitute.org/single_cell/study/SCP1290/molecular-logic-of-

cellular-diversification-in-the-mammalian-cerebral-cortex) (Di Bella et al., 2021). The count matrices were then normalized by SCTransform function in Seurat (v4.0.2) to eliminate sequencing depth effects. Highly variable genes within the homeotic genes in both axolotl and mouse were identified by SelectIntegrationFeatures function of Seurat (v4.0.2). Based on that, axolotl development data and the mouse cerebral cortex atlas were integrated by FindAnchors and IntegrateData functions of Seurat (v4.0.2) with default dimensionality of 30.

Mfuzz analysis

Stereo-seq SCT normalized gene expression for cells from the same stage was aggregated to form a pseudo-bulk gene expression matrix. Prior to clustering, genes with expression < 0.5 at all stages were removed. The normalized data of the remaining genes was then Z-score transformed before executing the c-means fuzzy clustering the time-course regeneration data, with two centers and a cluster membership threshold of 0.8 (Kumar and M, 2007).

RNA velocity analysis

RNA velocity was performed by Dynamo following the instructions at https://dynamo-release.readthedocs.io/ (Qiu et al., 2021). The relative abundance of nascent (unspliced) and mature (spliced) mRNA can be exploited to estimate the rates of gene splicing and degradation. The unspliced and spliced raw count matrices were calculated by Velocity according to annotation file and bam file processed and annotated by handleBam (bin-point label was substituted by cell ID) (La Manno et al., 2018). Unspliced and spliced raw count matrix of regeneration-related cell types were extracted to process by *recipe_monocle* function in Dynamo (Qiu et al., 2021). Highly expressed genes with significant MoranI index were selected as feature genes to perform dimension reduction via UMAP with default parameters. Then, kinetic parameters and gene-wise RNA velocity vectors were estimated on the normalized matrix, which were projected into the visualized spatial plot to retain spatial information. Streamlines were used to visualize the velocity vector flows on specific regeneration-related cell types in injured dorsal region of telencephalic sections.

1046 To facilitate the understanding of related genes determining the fate of target cells,
1047 the continuous vector field in the UMAP space and spatial space were established by the
1048 vf VectorField function depending on sparseVFC to learn the high dimensional vector field
1049 in the expression space from sparse single nuclei cell velocity vector robustly. Next,
1050 based on the learned vf VectorField function, ddhodge function was applied on our data
1051 to obtain UMAP pseudotime and spatial pseudotime. Finally, the gene expression
1052 dynamics vector field was visualized along the pseudotime, and genes with significant
1053 spatio-temporal expressional preference were selected.
1054
1055 **FIGURE LEGENDS**
1056
1057 **Figure 1. Stereo-seq visualizes spatial transcriptome profile of axolotl**
1058 **telencephalon at single-cell resolution**
1059 (A) Schematic diagram of Stereo-seq for axolotl telencephalon. *Step 1*, sample collection
1060 and frozen section preparation of the adult axolotl telencephalon. *Step 2*, *in situ* RNA
1061 capture from tissue placed on the chip. *Step 3*, cDNA amplification, library construction
1062 and sequencing.
1063 (B) Overlaying spatially assigned spliced- (red) and unspliced-transcripts (green) with
1064 corresponding ssDNA staining picture (left). Single-nucleus were defined based on
1065 ssDNA staining and represented by different colors (right).
1066 (C) Unsupervised spatially constraint clustering analysis considering location information
1067 of individually deduced nucleus at single-cell resolution. Cells were colored by region
1068 annotation. DP, dorsal pallium. MP, medial pallium. LP, lateral pallium. VZ, ventricular
1069 zone.
1070 (D) UMAP visualization of all cells profiled in adult axolotl telencephalon section. The
1071 colors correspond to the 15 identified cell types.
1072 (E) Spatial distribution of cell types identified in adult axolotl telencephalon section at
1073 single-cell resolution. Cell types are annotated by colored cubes.
1074 (F) Spatial visualization of selected gene expression on Stereo-seq map (top) and their
1075 correspondent *in situ* hybridization image (bottom). *Neurod6,* excitatory neuron marker;
1076 *Gad1,* inhibitory neuron marker; and *Gfap,* radial glial cell marker.

1077 (G) Distribution of SSTIN cells in the medial pallium region of adult axolotl telencephalon.
1078 Putative SSTIN cells are colored by green and signified by white arrow (left). Single cells
1079 highly express *Sst* gene are signified by white arrow (right).
1080 See also Figure S1-S4
1081
1082 **Figure 2. Spatio-temporal transcriptomic atlas of developmental, juvenile, adult and**
1083 **metamorphosis axolotl telencephalons at single-cell resolution**
1084 (A) Schematic diagram of sample collection (left). Unsupervised clustering of the axolotl
1085 telencephalon sections at stage 44 (St.44), stage 54 (St.54), stage 57 (St.57), juvenile
1086 (Juv.), Adult and metamorphosis (Meta.). Cell types are distinguished by colors. Scale
1087 bars, 500 μm (right).
1088 (B) Dotplot showing the ratio dynamic of cell types in the axolotl telencephalon from St.44,
1089 St.54, St.57, Juv., Adult and Meta.
1090 (C) Violin plot (left) and spatial visualization (right) of gene module expression defining
1091 NSC (neural stem cell), Cell cycle and Translation captured by Stereo-seq at different
1092 stages of axolotl telencephalon development.
1093 (D) Bar plot represents the cell ratio dynamic of NSC in the development process of
1094 axolotl and mouse.
1095 (E) Violin plot of gene module expression defining NSC at different stages in axolotl
1096 telencephalon development and in mouse embryonic development.
1097 See also Figure S5-S12
1098
1099 **Figure3. Spatiotemporal transcriptomic atlas of axolotl brain regeneration at**
1100 **single-cell resolution**
1101 (A) Schematic diagram of samples collection (upper left). Spatial visualization of cell types
1102 identified on the axolotl telencephalon sections at homeostatic and regenerative stages
1103 at single-cell resolution. Cell types are annotated by colored cubes on top. The squares
1104 indicate the regions analyzed in B and D. Scale bars, 200 μm. DPI, day post injury.
1105 (B) Spatial visualization of cell distribution in VZ zone (upper) and key marker expression
1106 (bottom) in the injured part of adult axolotl telencephalon section across 2DPI, 5DPI,
1107 10DPI, 15DPI, 20DPI. Cell types are annotated by colored cubes on top.

1108 (C) Expression level of two gene modules in REARGC and other RGC cells from 2 DPI
1109 to 20 DPI (left). Heatmap reflecting the expression of genes from different modules (right).
1110 List of representative key markers in two modules, respectively (middle).
1111 (D) Left panel: Spatial visualization of REARGCs of two different states in the injured
1112 regions of adult axolotl telencephalon from 2 DPI to 20 DPI. Cell state is distinguished by
1113 the gene modules in C. Right panel: Spatial visualization of Cell cycle module expression
1114 from 2 DPI to 20 DPI.
1115 (E) EdU staining indicating the proliferating cells in 10 DPI and 15 DPI.
1116 See also Figure S13-S22
1117
1118 **Figure4. Dynamics of regeneration related cells in differentially recovered sections**
1119 **at 15 DPI reveal potential lineage transition process during regeneration**
1120 (A) Positions of 4 continuous sections at 15 DPI (top left) and respective 3D display (top
1121 middle). Spatial visualization of cell types identified in 4 continuous axolotl telencephalon
1122 sections at 15 DPI at single-cell resolution (bottom). Cell types are annotated by colored
1123 cubes on top. Scale bars, 500 μm.
1124 (B) Bubble plot reflecting the expression dynamics of marker gene defining REARGCs,
1125 RIPC1s and immature NPTXEXs, which are major cell types involved in axolotl
1126 telencephalon regeneration.
1127 (C) Spatial visualized heatmap showing the expression pattern of key markers for
1128 regenerative related cells in the injury area of section 15 DPI-2, 15 DPI-3 and 15 DPI-4.
1129 (D) Spatial visualization exhibiting the cell type distribution around the regenerating site
1130 in 15 DPI-4.
1131 (E-F) RNA velocity streamline plots showing the predicted trajectory of cell lineage
1132 transition in the regenerating region of axolotl telencephalon. Areas are colored by either
1133 annotated cell clusters (E) or pseudotime (F).
1134 (G) Expression heatmap of genes with high transitional activities in a pseudo-temporal
1135 order accord with the regeneration process.
1136 (H) Scatter plot showing the pseudotime kinetics of *Nes*, *S100a10*, *Ankrd1*, *Nptx1*, *Satb1*
1137 and *Cdkn1c* in regenerating cell types.
1138 See also Figure S23-S27

1139

1140 **Figure5. Comparison of neurogenesis in development and regeneration process**

1141 (A-B) Spatial distribution of RGCs, IPCs, immature NPTXEXs and NPTXEXs in the dorsal
1142 pallium of left hemisphere at 15 DPI-4 (A), and at St.44, St.54, St.57 and Juv. (B).

1143 (C) Heatmap represents the correlation between different RGC types across four
1144 developmental or regenerative stages.

1145 (D) Spatial distribution of dorsal pallium cell types in the left hemisphere of axolotl
1146 telencephalon, cells potentially involved in the development of NPTXEX are framed by
1147 white dash line. Cell types are annotated by colored cubes on top.

1148 (E) Spatial visualized expression of key markers for cells involved in NPTXEX
1149 development.

1150 (F) RNA velocity streamline plot showing the predicted dorsal pallium development
1151 trajectory in the left hemisphere of axolotl telencephalon at St.57 .

1152 (G-H) RNA velocity streamline plot showing the predicted lineage transition trajectory of
1153 RGCs, IPCs, immature NPTXEXs and NPTXEXs at St.57 (G) and 15 DPI-4 (H).

1154 (I) Left panel: Heatmap of gene expression during NPTXEX development and
1155 regeneration. Eight distinct groups of genes were sorted by their expression dynamic
1156 pattern. Right panel: Line plot depicting standardized Stereo-seq signal by fuzzy cluster
1157 analysis for eight groups, with green lines representing the expression dynamics of each
1158 individual gene and the orange line representing the integrated pattern of each group at
1159 Stage 57 and 15 DPI (right). Names of eight groups are listed on top right. Dev UP&Reg
1160 UP, co-upregulation in development and regeneration. Dev UP&Reg Down, upregulation
1161 in development while downregulation in regeneration. Dev UP&Reg None, upregulation
1162 in development while no significant change in regeneration. Dev Down&Reg Down, co-
1163 downregulation in development and regeneration. Dev Down&Reg UP, downregulation
1164 in development while upregulation in regeneration. Dev Down&Reg None,
1165 downregulation in development while no significant change in regeneration. Dev
1166 None&Reg UP, no significant change in development while upregulation in regeneration.
1167 Dev None&Reg Down, no significant change in development while downregulation in
1168 regeneration.

1169 (J) Barplot exhibiting the representative GO enrichment pathways of Dev UP&Reg UP,
1170 Dev Down&Reg Down, Dev None&Reg UP and Dev None&Reg Down in I.
1171 See also Figure S28-S30
1172 **Figure S1. Stereo-seq at single-cell resolution, related to Figure 1**
1173 (A) The arrangement of DNB array used to capture mRNA in single nucleus.
1174 (B) Images of ssDNA staining, spatial visualization of cell types, spatial visualization of
1175 gene expression and corresponding *in situ* hybridization of *Nptx1*, *Slc1a3* and *Cck*.
1176
1177 **Figure S2. Spatial visualization of marker genes in the adult axolotl telencephalon,**
1178 **related to Figure 1**
1179 (A) Heatmap showing the mean expression of DEGs between the 15 cell types in Figure
1180 1D and E.
1181 (B) Spatial visualization of representative cell type markers in adult axolotl telencephalon
1182 section at single-cell resolution (left). *In situ* hybridization of representative cell type
1183 markers in axolotl telencephalon section (right).
1184
1185 **Figure S3. Cell type distribution of adult axolotl telencephalon, related to Figure 1**
1186 (A-B) Boxplot showing the count number of UMIs (transcripts) (A) and genes (B) captured
1187 by Stereo-seq in 15 cell types of adult axolotl telencephalon, related to Figure 1D and E.
1188 (C) Barplot exhibiting the number of single-nucleus for each cell type analyzed in Figure
1189 1.
1190 (D) Pie chart reflecting the ratio of each cell type detected in adult axolotl telencephalon.
1191 (E) Spatial distribution of each cell type on adult axolotl telencephalon section, cell types
1192 are colored as annotated in Figure 1.
1193
1194 **Figure S4. Stereo-seq identifies ventricular zone (VZ) cells in the adult axolotl**
1195 **telencephalon, related to Figure 1**
1196 Spatial visualization of radial glial marker expression in VZ on adult axolotl telencephalon
1197 section. Expression of markers are exhibited at single-cell resolution (left). Integrated
1198 expression of 6 markers is displayed as unified gene module (right).
1199

1200 **Figure S5. Unsupervised clustering of cells in axolotl telencephalon development,**
1201 **related to Figure 2**
1202 (A) UMAP showing the clusters in each stage in Figure 2. 33 cell types are identified and
1203 annotated as in Figure 2A.
1204 (B) UMAP showing the integration of 33 cell types across different stages.
1205 (C) UMAP showing the distribution of cells from each sampling stage in Figure 2. Red
1206 dots represent the cells from the corresponding time point, gray dots represent all the
1207 other cells.
1208
1209 **Figure S6. Markers of cell cluster in axolotl telencephalon, related to Figure 2**
1210 Heatmap showing the normalized expression of marker genes for the indicated
1211 anatomical structures of the axolotl telencephalon sections profiled by Stereo-seq in
1212 Figure 2A.
1213
1214 **Figure S7, S8, S9, S10, S11. Global spatial profiling of cell types, related to Figure**
1215 **2**
1216 Spatial visualization of cell type distribution in different axolotl telencephalon sections
1217 profiled by Stereo-seq in Figure 2A. Cells were colored by their annotation.
1218
1219 **Figure S12. Comparative analysis of NSC between axolotl and mouse, related to**
1220 **Figure 2**
1221 (A) UMAP of integrated axolotl Stereo-seq data and mouse single-cell RNA-seq data.
1222 (B-C) UMAP visualization of cell types identified in axolotl data (B) and mouse data(C).
1223 (D) UMAP visualization of mouse embryonic neural stem cells at each stage profiled by
1224 single-cell RNA-seq. Red dots represent neural stem cells at each stage, gray dots
1225 represent other cells at respective stage.
1226
1227 **Figure S13. Cell dynamics of axolotl telencephalon regeneration, related to Figure**
1228 **3**
1229 (A) UMAP visualizing the clusters at each stage. 23 cell types are identified and annotated
1230 as in Figure 3A.

(B) UMAP showing the integration of 23 cell types across different stages.
(C) UMAP showing the distribution of cells from each sampling stage in Figure 3A. Red dots represent the cells from the corresponding time point, gray dots represent all the other cells.
(D) Dotplot showing the cell ratio dynamics from control to 60 DPI during axolotl telencephalon regeneration. Red dots represent cellular ratio in injured hemisphere, blue dots represent cellular ratio in uninjured hemisphere, dot size reflect the ratio.

Figure S14. Markers of cell clusters across axolotl telencephalon sections at regenerative stages, related to Figure3

Heatmap showing the normalized expression of marker genes of 23 cell types from axolotl telencephalon sections at regenerative stages profiled by Stereo-seq in Figure 3A.

Figure S15, S16, S17, S18, S19, S20, S21, S22 Global spatial profiling of cell types at regenerative stages, related to Figure 3

Spatial visualization of cell type distribution at different axolotl telencephalon regenerative stages profiled by Stereo-seq in Figure 3A. Cells were colored by their annotation.

Figure S23. Unsupervised clustering of cells across continuous sections at 15 DPI, related to Figure 4

(A) UMAP visualization of clusters in each section at 15 DPI. 25 cell types are identified and annotated as in Figure 4.
(B) UMAP showing the integration of 25 cell types across different sections.
(C) UMAP showing the distribution of cells from each sampling section in Figure 4A. Red dots represent the cells from the corresponding time point, gray dots represent all the other cells.
(D) Dotplot showing the cell ratio dynamics in different regeneration sections at 15 DPI. Red dots represent cellular ratio in injured hemisphere, blue dots represent cellular ratio in uninjured hemisphere, dot size reflect the ratio.

Figure S24. Markers of cell clusters across continuous sections at 15 DPI, related to Figure 4

Heatmap showing the normalized expression of marker genes for 25 cell types in 4 neighbor axolotl telencephalon sections at 15 DPI profiled by Stereo-seq in Figure 4A.

Figure S25, S26, S27. Global spatial profiling of cell types across continuous sections at 15 DPI , related to Figure 4

Spatial visualization of cell type distribution in neighbor regenerating sections of the axolotl telencephalon at 15 DPI profiled by Stereo-seq in Figure 4A. Cells were colored by their annotation.

Figure S28. RNA velocity analysis of 15 DPI-2 and 15 DPI-3, related to Figure 4

(A) Spatial visualization of cell types involved in regeneration around the injured site of 15DPI-2(A).

(B-C) RNA velocity streamline plots simulating the regeneration trajectory of 15DPI-2. Cells are colored by their annotation(B) or pseudotime (C).

(D) Expression heatmap of genes with high transitional activity in a pseudo-temporal order in section 15 DPI-2.

(E) Scatter plots showing the pseudotime kinetics of *Nes*, *Tnc*, *Tubb6*, *Cdkn1a*, *Ankrd1* and *Nptx1* in different cell types of 15 DPI-2.

(F) Spatial visualization of cell types involved in regeneration around the injured site of 15 DPI-3(F).

(G-H) RNA velocity streamline plots simulating the regeneration trajectory of 15 DPI-3. Cells are colored by their annotation (G) or pseudotime (H).

(I) Expression heatmap of genes with high transitional activity in a pseudo-temporal order in section15 DPI-3.

(J) Scatter plots showing the pseudotime kinetics of *S100a10*, *Nes*, *Cdkn1c*, *Cdkn1a*, *Nptx1*and *Ankrd1* in different cell types of 15 DPI-3.

FigureS29. Neurogenesis trajectory analysis of axolotl telencephalon at different developmental stages

1292 (A-C) Spatial visualization of cells involved in telencephalon development at stage 44 (A),
1293 stage 54 (B) and juvenile (C) (left). Expression of key marker genes at stage 44 (A), stage
1294 54 (B) and juvenile (C) (middle). RNA velocity streamline plots showing the predicted
1295 lineage transition trajectory at stage 44 (A), stage 54 (B) and juvenile (C) (right).
1296
1297 **FigureS30. DEGs between development and regeneration**
1298 Spatial visualization of the expression of *JunD, Tnc, Krt18*, *S100a10*, *Tagln2, Tnfsf10* and
1299 *Ankrd1* in sections of stage 57 and 15 DPI-4.
1300
1301 **TABLE LEGENDS**

1302 **Table S1. Description of all samples profiled, cell types and top 20 marker genes.**

1303 **Table S2. Gene list for cluster annotation.**

1304 **Table S3. Gene list of three gene modules defining NSC, cell cycle and**
1305 **translation.**

1306 **Table S4. Gene list of two gene modules in REARGC from 2 to 20 DPI.**

1307 **Table S5. Gene list of the eight patterned groups during development and**
1308 **regeneration processes.**

1309 **Table S6. DEGs of left dorsal pallium region between regeneration and**
1310 **development.**

1311 **Table S7. Primer sequences for ISH.**

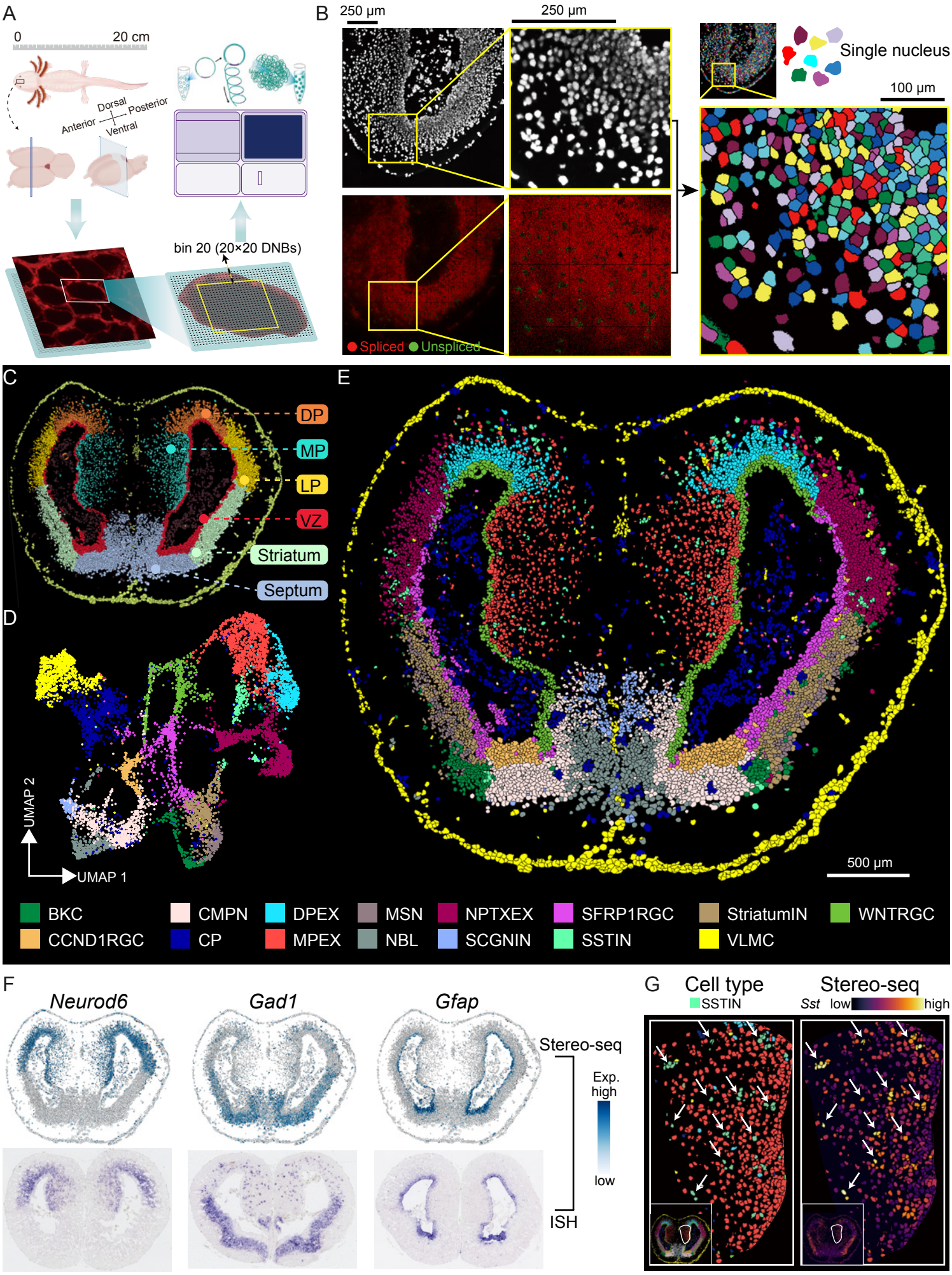
A
0
20 cm
Dorsal
Posterior
Anterior
Ventral
bin 20 (20×20 DNBs)
B
250 μm
250 μm
Single nucleus
100 μm
Spliced
Unspliced
C
DP
MP
LP
VZ
Striatum
Septum
D
UMAP 2
UMAP 1
E
500 μm
BKC
CCND1RGC
CMPN
CP
DPEX
MPEX
MSN
NBL
NPTXEX
SCGNIN
SFRP1RGC
SSTIN
StriatumIN
VLMC
WNTRGC
F
Neurod6
Gad1
Gfap
Stereo-seq
ISH
Exp.
high
low
G
Cell type
SSTIN
Stereo-seq
Sst
low
high

Figure 1

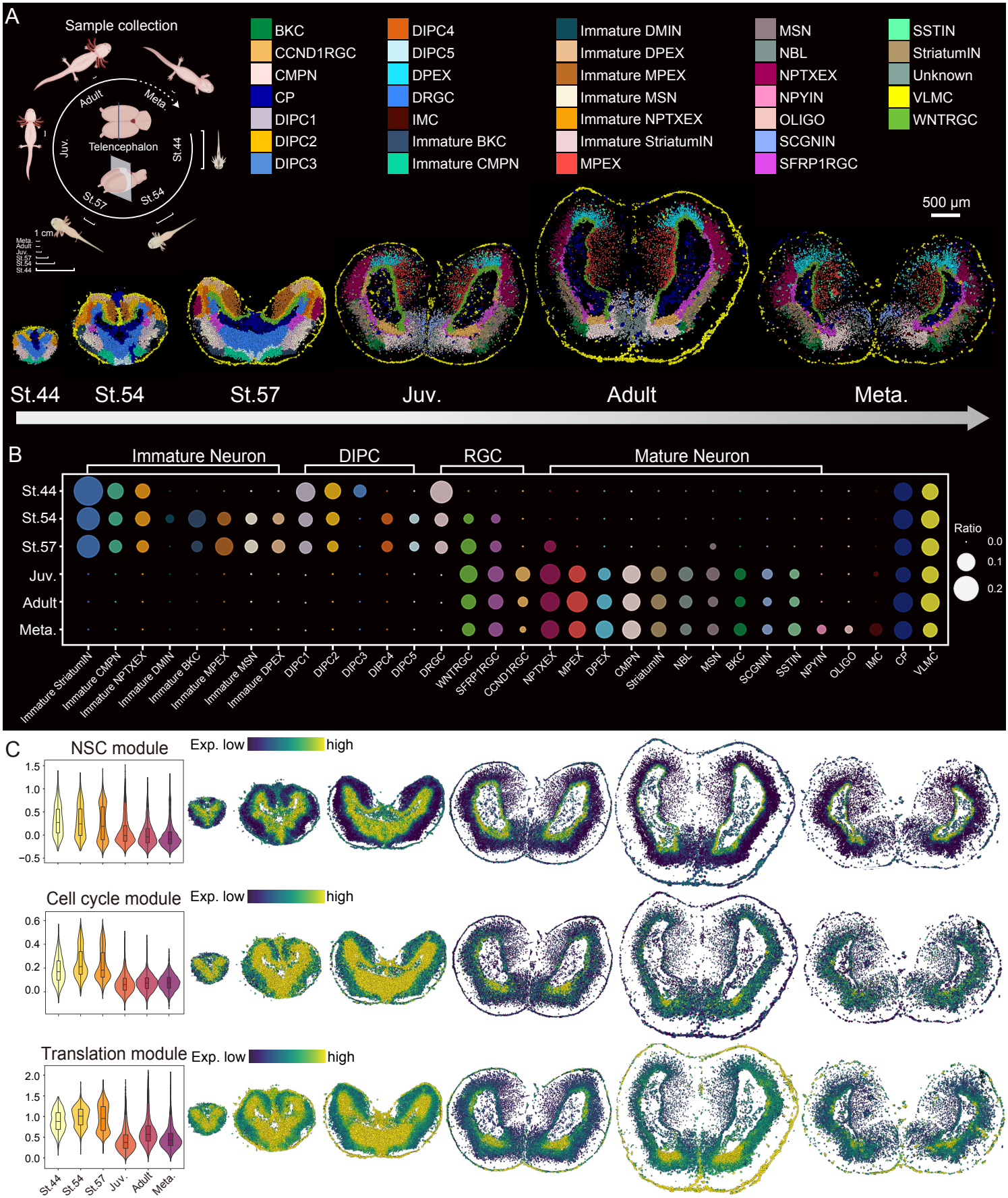
A
Sample collection
Adult
Meta.
Juv.
Telencephalon
St.44
St.57
St.54
1 cm
BKC
CCND1RGC
CMPN
CP
DIPC1
DIPC2
DIPC3
DIPC4
DIPC5
DPEX
DRGC
IMC
Immature BKC
Immature CMPN
Immature DMIN
Immature DPEX
Immature MPEX
Immature MSN
Immature NPTXEX
Immature StriatumIN
MPEX
MSN
NBL
NPTXEX
NPYIN
OLIGO
SCGNIN
SFRP1RGC
SSTIN
StriatumIN
Unknown
VLMC
WNTRGC
500 μm
St.44
St.54
St.57
Juv.
Adult
Meta.
B
Immature Neuron
DIPC
RGC
Mature Neuron
Ratio
0.0
0.1
0.2
Immature StriatumIN
Immature CMPN
Immature NPTXEX
Immature DMIN
Immature BKC
Immature MPEX
Immature MSN
Immature DPEX
DIPC1
DIPC2
DIPC3
DIPC4
DIPC5
DRGC
WNTRGC
SFRP1RGC
CCND1RGC
NPTXEX
MPEX
DPEX
CMPN
StriatumIN
NBL
MSN
BKC
SCGNIN
SSTIN
NPYIN
OLIGO
IMC
CP
VLMC
C
NSC module
Exp. low
high
Cell cycle module
Translation module
St.44
St.54
St.57
Juv.
Adult
Meta.
D
NSC Ratio
Axolotl
Mouse
E
NSC gene module expression
Axolotl
Mouse
Development
Development

Figure 2

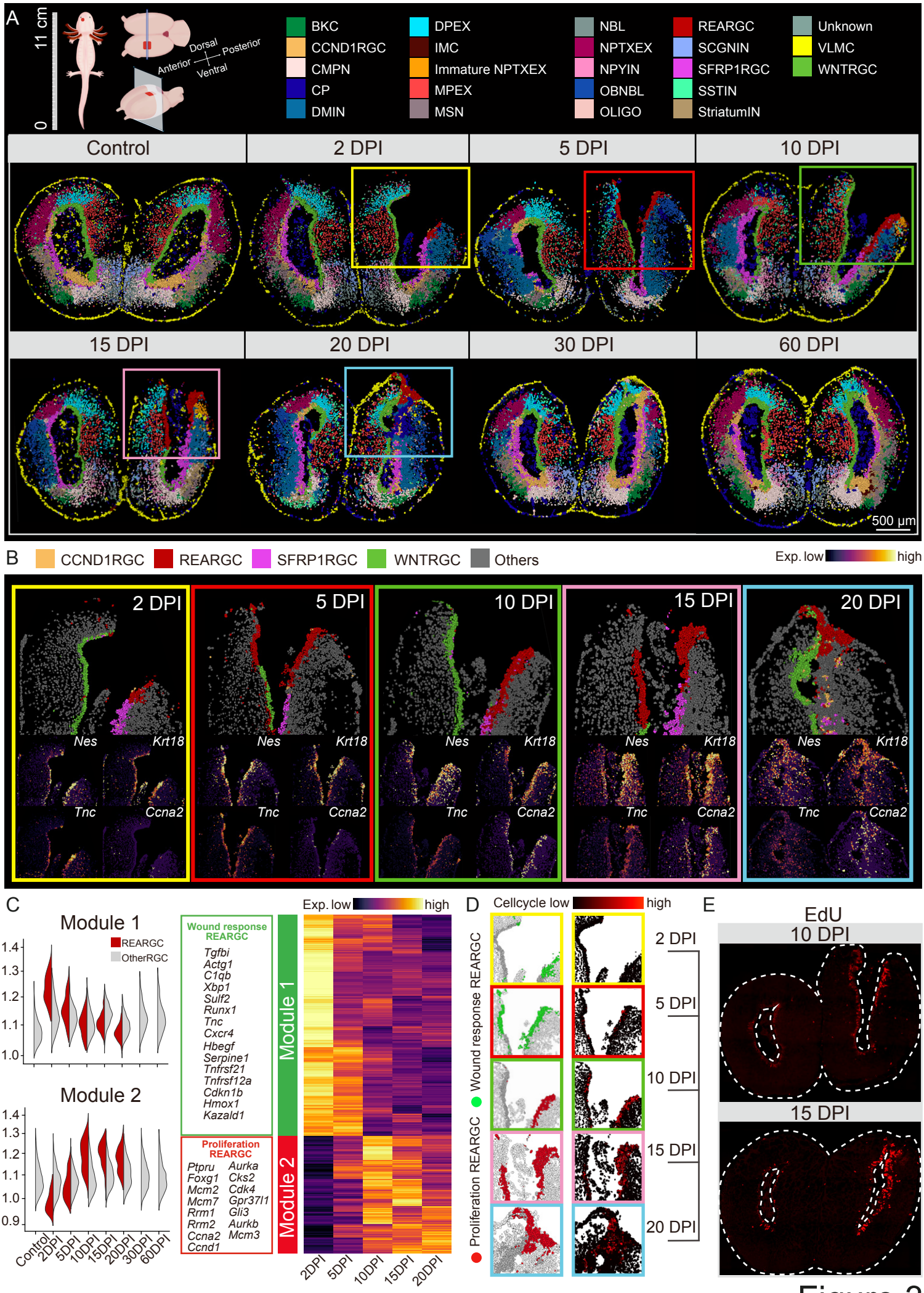
A
11 cm
0
Dorsal
Posterior
Anterior
Ventral
BKC
CCND1RGC
CMPN
CP
DMIN
DPEX
IMC
Immature NPTXEX
MPEX
MSN
NBL
NPTXEX
NPYIN
OBNBL
OLIGO
REARGC
SCGNIN
SFRP1RGC
SSTIN
StriatumIN
Unknown
VLMC
WNTRGC
Control
2 DPI
5 DPI
10 DPI
15 DPI
20 DPI
30 DPI
60 DPI
500 µm
B
CCND1RGC
REARGC
SFRP1RGC
WNTRGC
Others
Exp. low
high
2 DPI
5 DPI
10 DPI
15 DPI
20 DPI
Nes
Krt18
Tnc
Ccna2
C
Module 1
REARGC
OtherRGC
Module 2
Control
2DPI
5DPI
10DPI
15DPI
20DPI
30DPI
60DPI
Wound response REARGC
Tgfbi
Actg1
C1qb
Xbp1
Sulf2
Runx1
Tnc
Cxcr4
Hbegf
Serpine1
Tnfrsf21
Tnfrsf12a
Cdkn1b
Hmox1
Kazald1
Proliferation REARGC
Ptpru
Foxg1
Mcm2
Mcm7
Rrm1
Rrm2
Ccna2
Ccnd1
Aurka
Cks2
Cdk4
Gpr37l1
Gli3
Aurkb
Mcm3
Module 1
Module 2
Exp. low
high
D
Cellcycle low
high
Wound response REARGC
Proliferation REARGC
2 DPI
5 DPI
10 DPI
15 DPI
20 DPI
E
EdU
10 DPI
15 DPI

Figure 3

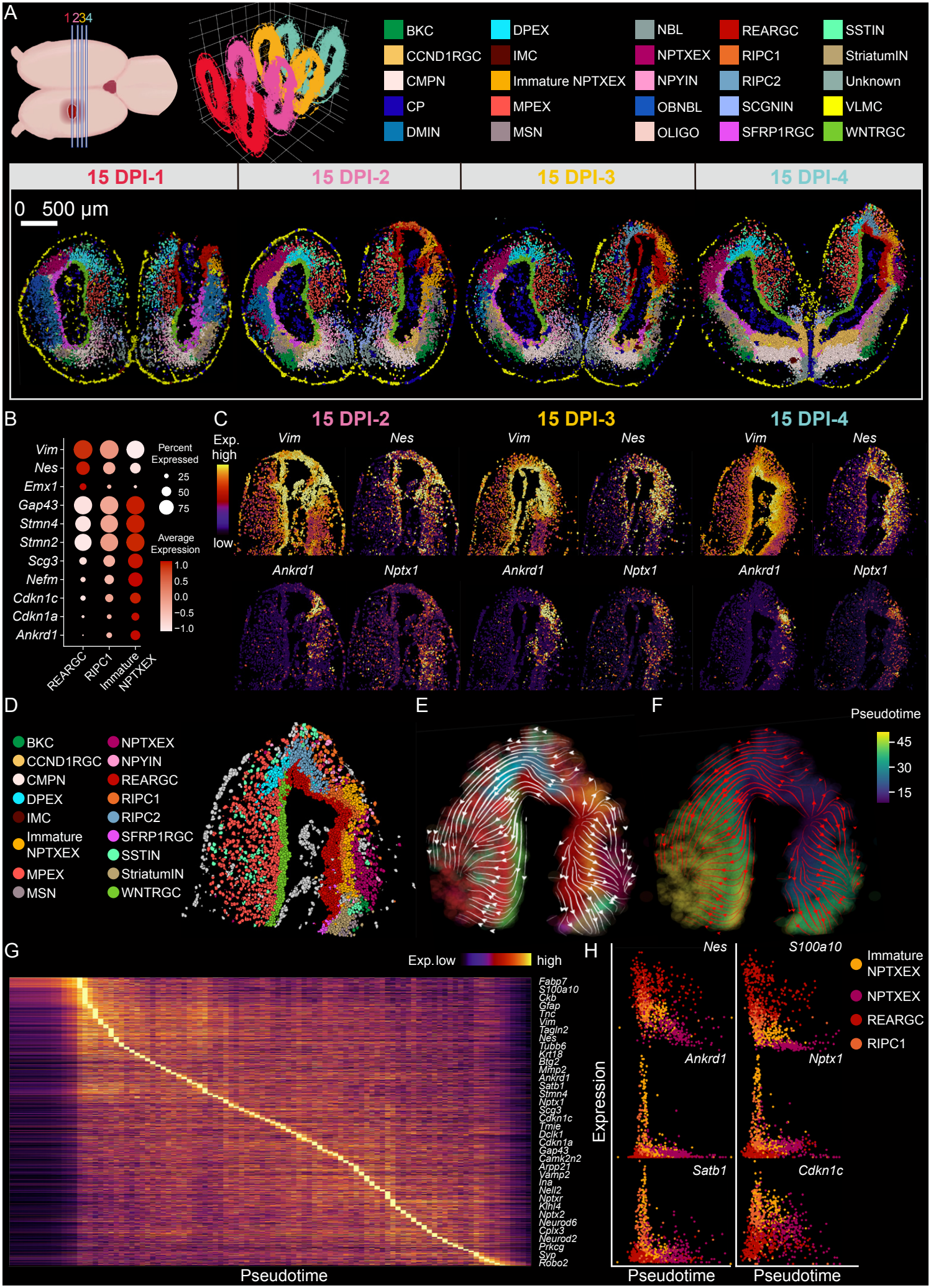
A
1 2 3 4
BKC
CCND1RGC
CMPN
CP
DMIN
DPEX
IMC
Immature NPTXEX
MPEX
MSN
NBL
NPTXEX
NPYIN
OBNBL
OLIGO
REARGC
RIPC1
RIPC2
SCGNIN
SFRP1RGC
SSTIN
StriatumIN
Unknown
VLMC
WNTRGC
15 DPI-1
15 DPI-2
15 DPI-3
15 DPI-4
0 500 µm
B
Vim
Nes
Emx1
Gap43
Stmn4
Stmn2
Scg3
Nefm
Cdkn1c
Cdkn1a
Ankrd1
REARGC
RIPC1
Immature NPTXEX
Percent Expressed
25
50
75
Average Expression
1.0
0.5
0.0
−0.5
−1.0
C
Exp. high
low
15 DPI-2
15 DPI-3
15 DPI-4
Vim
Nes
Ankrd1
Nptx1
D
BKC
CCND1RGC
CMPN
DPEX
IMC
Immature NPTXEX
MPEX
MSN
NPTXEX
NPYIN
REARGC
RIPC1
RIPC2
SFRP1RGC
SSTIN
StriatumIN
WNTRGC
E
F
Pseudotime
45
30
15
G
Exp. low
high
Fabp7
S100a10
Ckb
Gfap
Tnc
Vim
Tagln2
Nes
Tubb6
Krt18
Btg2
Mmp2
Ankrd1
Satb1
Stmn4
Nptx1
Scg3
Cdkn1c
Tmie
Dclk1
Cdkn1a
Gap43
Camk2n2
Arpp21
Vamp2
Ina
Nell2
Nptxr
Klhl4
Nptx2
Neurod6
Cplx3
Neurod2
Prkcg
Syp
Robo2
Pseudotime
H
Nes
S100a10
Ankrd1
Nptx1
Satb1
Cdkn1c
Expression
Immature NPTXEX
NPTXEX
REARGC
RIPC1
Pseudotime
Pseudotime

Figure 4

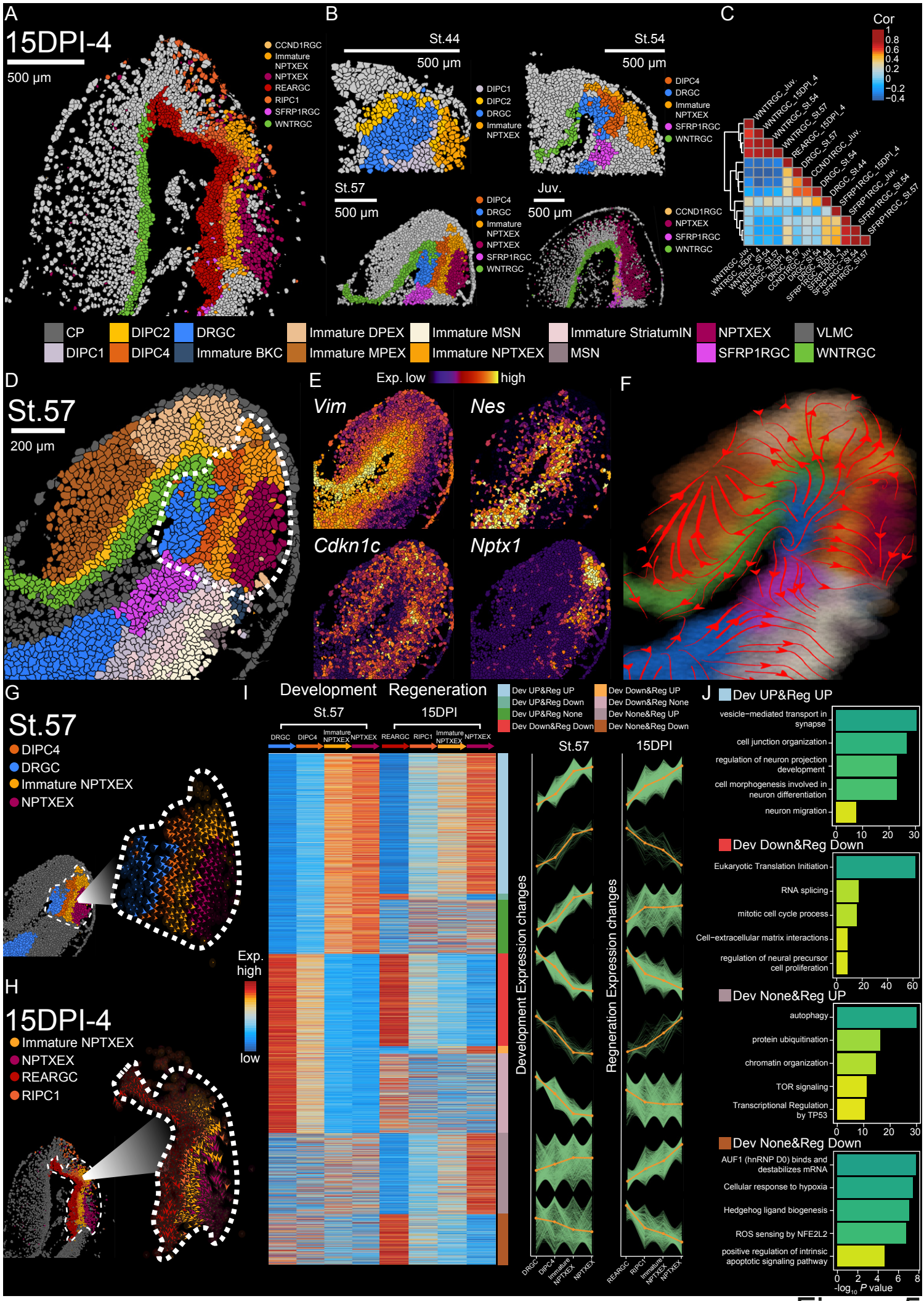
A
15DPI-4
500 µm
CCND1RGC
Immature NPTXEX
NPTXEX
REARGC
RIPC1
SFRP1RGC
WNTRGC
B
St.44
500 µm
DIPC1
DIPC2
DRGC
Immature NPTXEX
St.54
500 µm
DIPC4
DRGC
Immature NPTXEX
SFRP1RGC
WNTRGC
St.57
500 µm
DIPC4
DRGC
Immature NPTXEX
NPTXEX
SFRP1RGC
WNTRGC
Juv.
500 µm
CCND1RGC
NPTXEX
SFRP1RGC
WNTRGC
C
Cor
1
0.8
0.6
0.4
0.2
0
−0.2
−0.4
WNTRGC_Juv.
WNTRGC_15DPI_4
WNTRGC_St.54
WNTRGC_St.57
REARGC_St.57
REARGC_15DPI_4
DRGC_St.57
CCND1RGC_Juv.
DRGC_St.54
DRGC_St.44
SFRP1RGC_15DPI_4
SFRP1RGC_Juv.
SFRP1RGC_St.54
SFRP1RGC_St.57
CP
DIPC1
DIPC2
DIPC4
DRGC
Immature BKC
Immature DPEX
Immature MPEX
Immature MSN
Immature NPTXEX
Immature StriatumIN
MSN
NPTXEX
SFRP1RGC
VLMC
WNTRGC
D
St.57
200 µm
E
Exp. low
high
Vim
Nes
Cdkn1c
Nptx1
F
G
St.57
DIPC4
DRGC
Immature NPTXEX
NPTXEX
H
15DPI-4
Immature NPTXEX
NPTXEX
REARGC
RIPC1
Exp.
high
low
I
Development
Regeneration
St.57
15DPI
DRGC
DIPC4
Immature NPTXEX
NPTXEX
REARGC
RIPC1
Immature NPTXEX
NPTXEX
Dev UP&Reg UP
Dev UP&Reg Down
Dev UP&Reg None
Dev Down&Reg Down
Dev Down&Reg UP
Dev Down&Reg None
Dev None&Reg UP
Dev None&Reg Down
Development Expression changes
Regneration Expression changes
J
Dev UP&Reg UP
vesicle−mediated transport in synapse
cell junction organization
regulation of neuron projection development
cell morphogenesis involved in neuron differentiation
neuron migration
0
10
20
30
Dev Down&Reg Down
Eukaryotic Translation Initiation
RNA splicing
mitotic cell cycle process
Cell−extracellular matrix interactions
regulation of neural precursor cell proliferation
0
20
40
60
Dev None&Reg UP
autophagy
protein ubiquitination
chromatin organization
TOR signaling
Transcriptional Regulation by TP53
0
10
20
30
Dev None&Reg Down
AUF1 (hnRNP D0) binds and destabilizes mRNA
Cellular response to hypoxia
Hedgehog ligand biogenesis
ROS sensing by NFE2L2
positive regulation of intrinsic apoptotic signaling pathway
0
2
4
6
8
-log10 P value

Figure 5

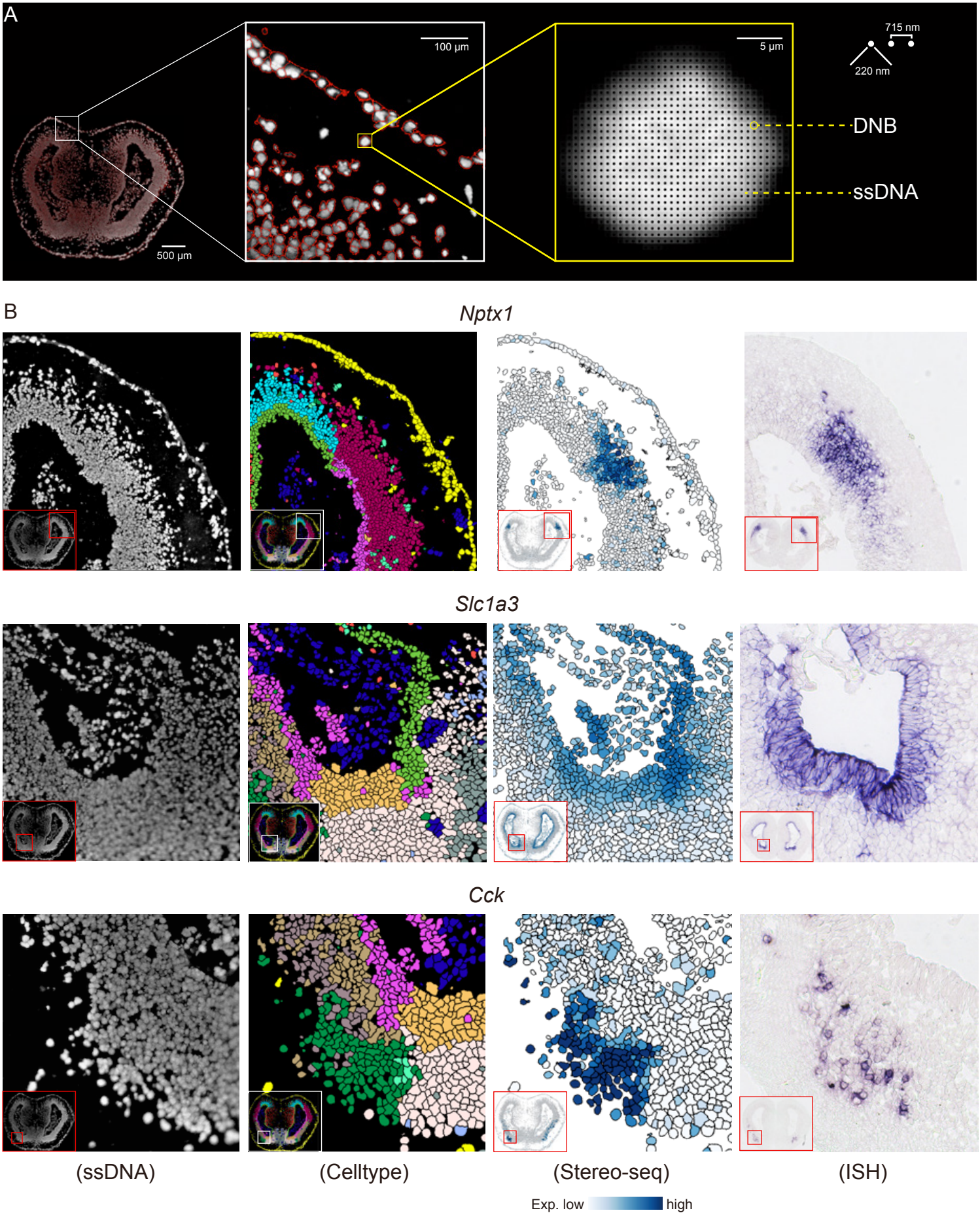
A
500 µm
100 µm
5 µm
715 nm
220 nm
DNB
ssDNA
B
Nptx1
Slc1a3
Cck
(ssDNA)
(Celltype)
(Stereo-seq)
(ISH)
Exp. low
high

Figure S1

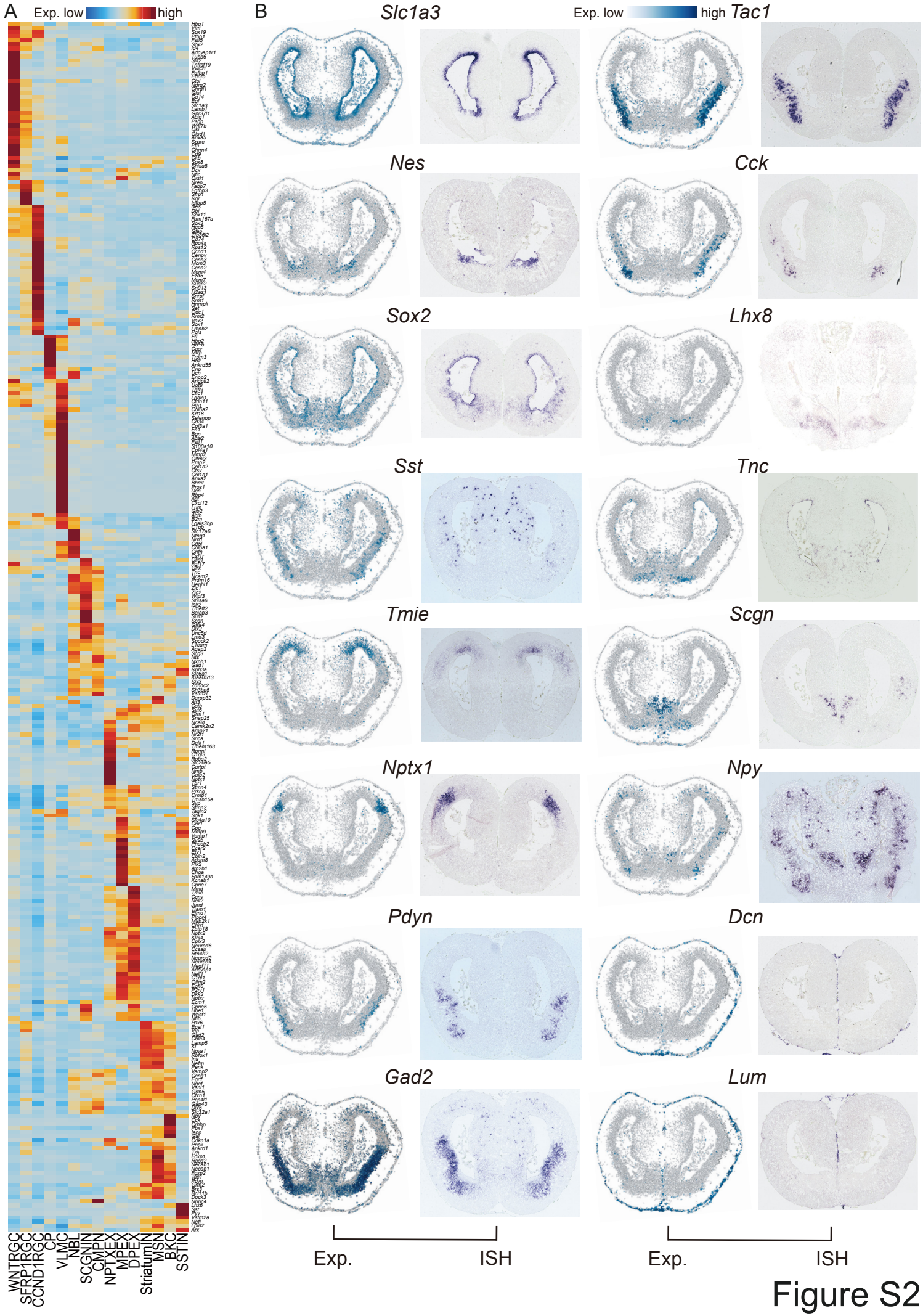
A
Exp. low
high
WNTRGC
SFRP1RGC
CCND1RGC
CP
VLMC
NBL
SCGNIN
CMPN
NPTXEX
MPEX
DPEX
StriatumIN
MSN
BKC
SSTIN
B
Slc1a3
Exp. low
high
Tac1
Nes
Cck
Sox2
Lhx8
Sst
Tnc
Tmie
Scgn
Nptx1
Npy
Pdyn
Dcn
Gad2
Lum
Exp.
ISH
Exp.
ISH

Figure S2

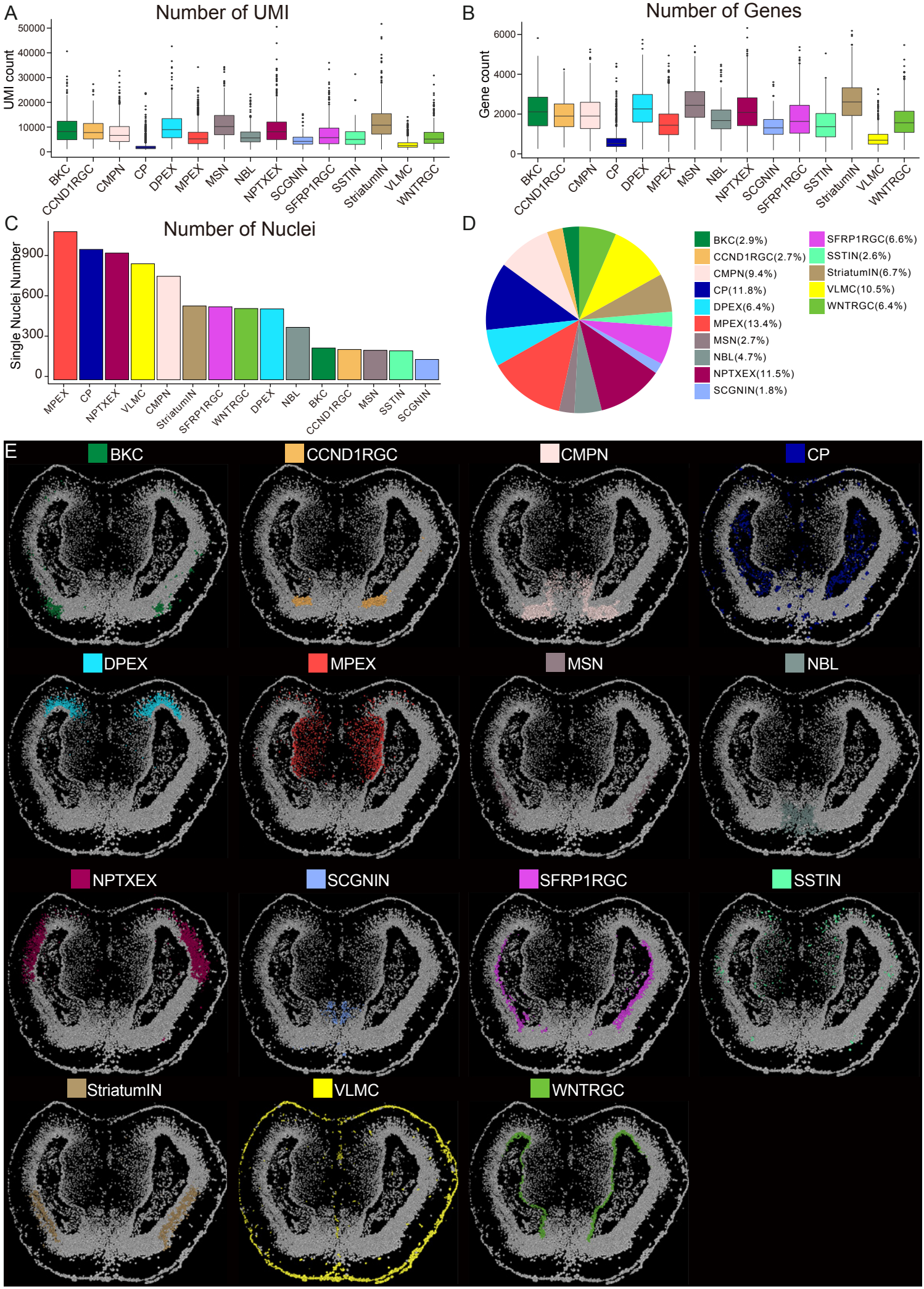
A
Number of UMI
UMI count
50000
40000
30000
20000
10000
0
BKC
CCND1RGC
CMPN
CP
DPEX
MPEX
MSN
NBL
NPTXEX
SCGNIN
SFRP1RGC
SSTIN
StriatumIN
VLMC
WNTRGC
B
Number of Genes
Gene count
6000
4000
2000
0
C
Number of Nuclei
Single Nuclei Number
900
600
300
0
MPEX
CP
NPTXEX
VLMC
CMPN
StriatumIN
SFRP1RGC
WNTRGC
DPEX
NBL
BKC
CCND1RGC
MSN
SSTIN
SCGNIN
D
BKC(2.9%)
CCND1RGC(2.7%)
CMPN(9.4%)
CP(11.8%)
DPEX(6.4%)
MPEX(13.4%)
MSN(2.7%)
NBL(4.7%)
NPTXEX(11.5%)
SCGNIN(1.8%)
SFRP1RGC(6.6%)
SSTIN(2.6%)
StriatumIN(6.7%)
VLMC(10.5%)
WNTRGC(6.4%)
E
BKC
CCND1RGC
CMPN
CP
DPEX
MPEX
MSN
NBL
NPTXEX
SCGNIN
SFRP1RGC
SSTIN
StriatumIN
VLMC
WNTRGC

Figure S3

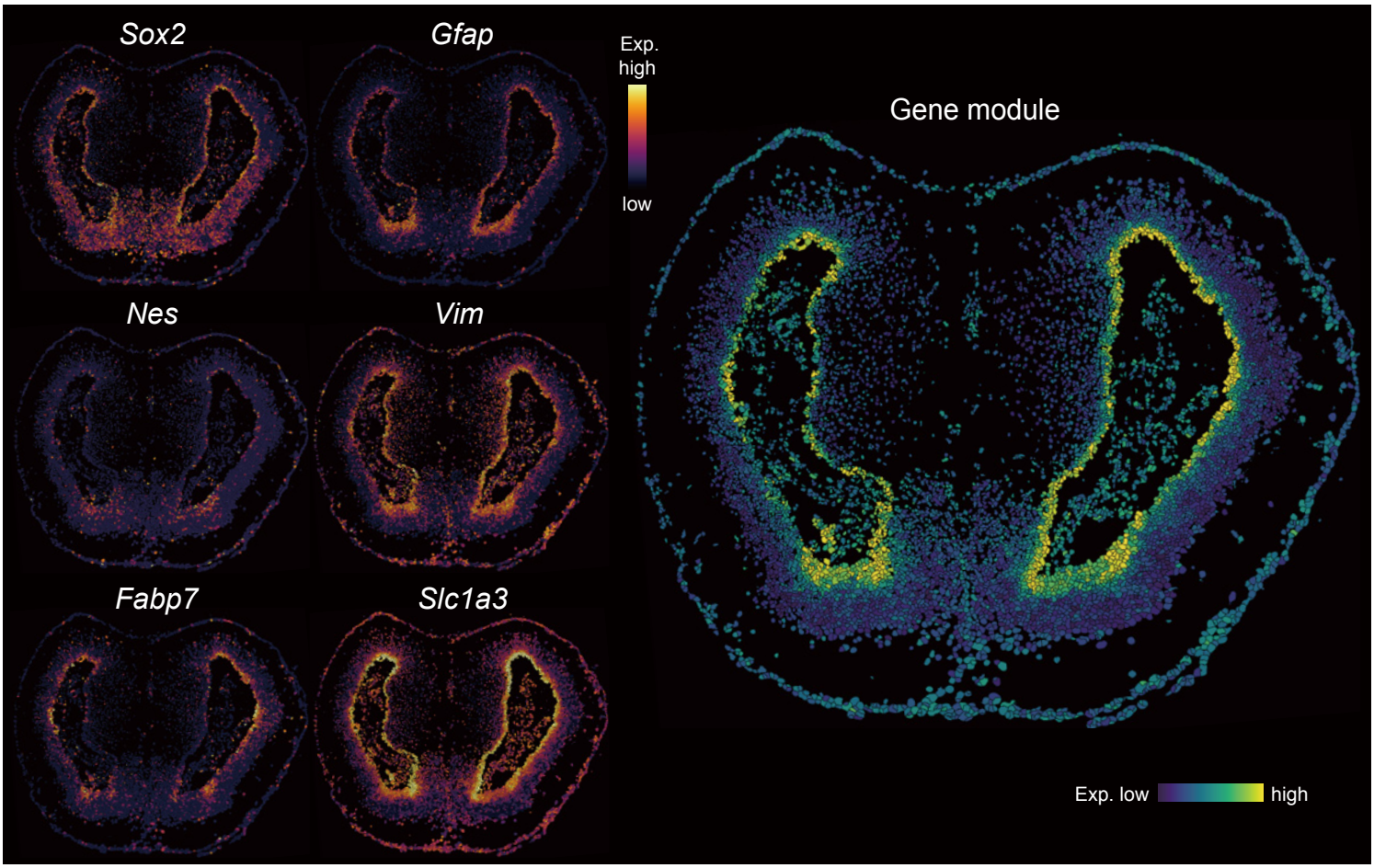
Sox2
Gfap
Nes
Vim
Fabp7
Slc1a3
Exp.
high
low
Gene module
Exp. low
high

Figure S4

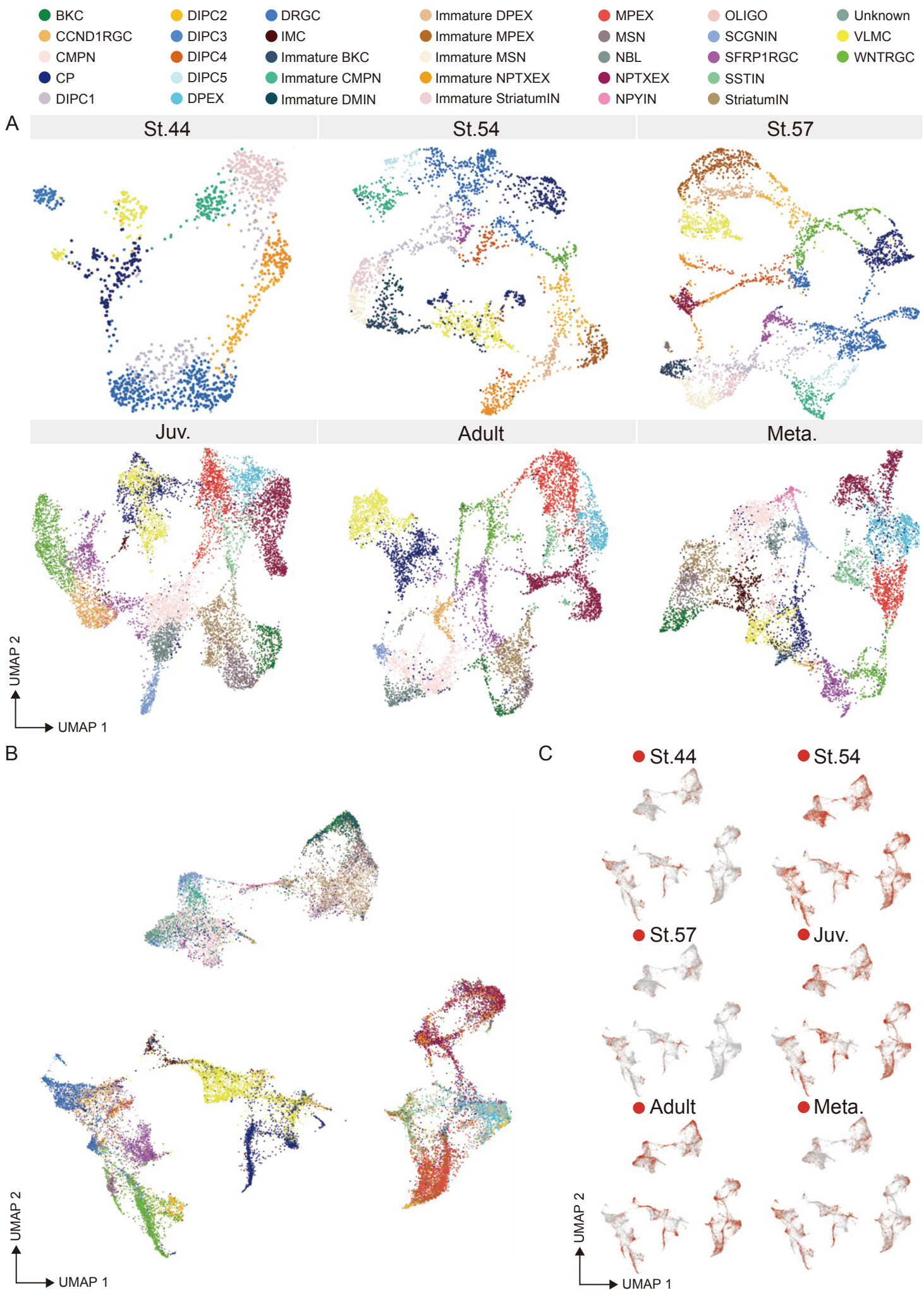
BKC
CCND1RGC
CMPN
CP
DIPC1
DIPC2
DIPC3
DIPC4
DIPC5
DPEX
DRGC
IMC
Immature BKC
Immature CMPN
Immature DMIN
Immature DPEX
Immature MPEX
Immature MSN
Immature NPTXEX
Immature StriatumIN
MPEX
MSN
NBL
NPTXEX
NPYIN
OLIGO
SCGNIN
SFRP1RGC
SSTIN
StriatumIN
Unknown
VLMC
WNTRGC
A
St.44
St.54
St.57
Juv.
Adult
Meta.
UMAP 2
UMAP 1
B
UMAP 2
UMAP 1
C
St.44
St.54
St.57
Juv.
Adult
Meta.
UMAP 2
UMAP 1

Figure S5

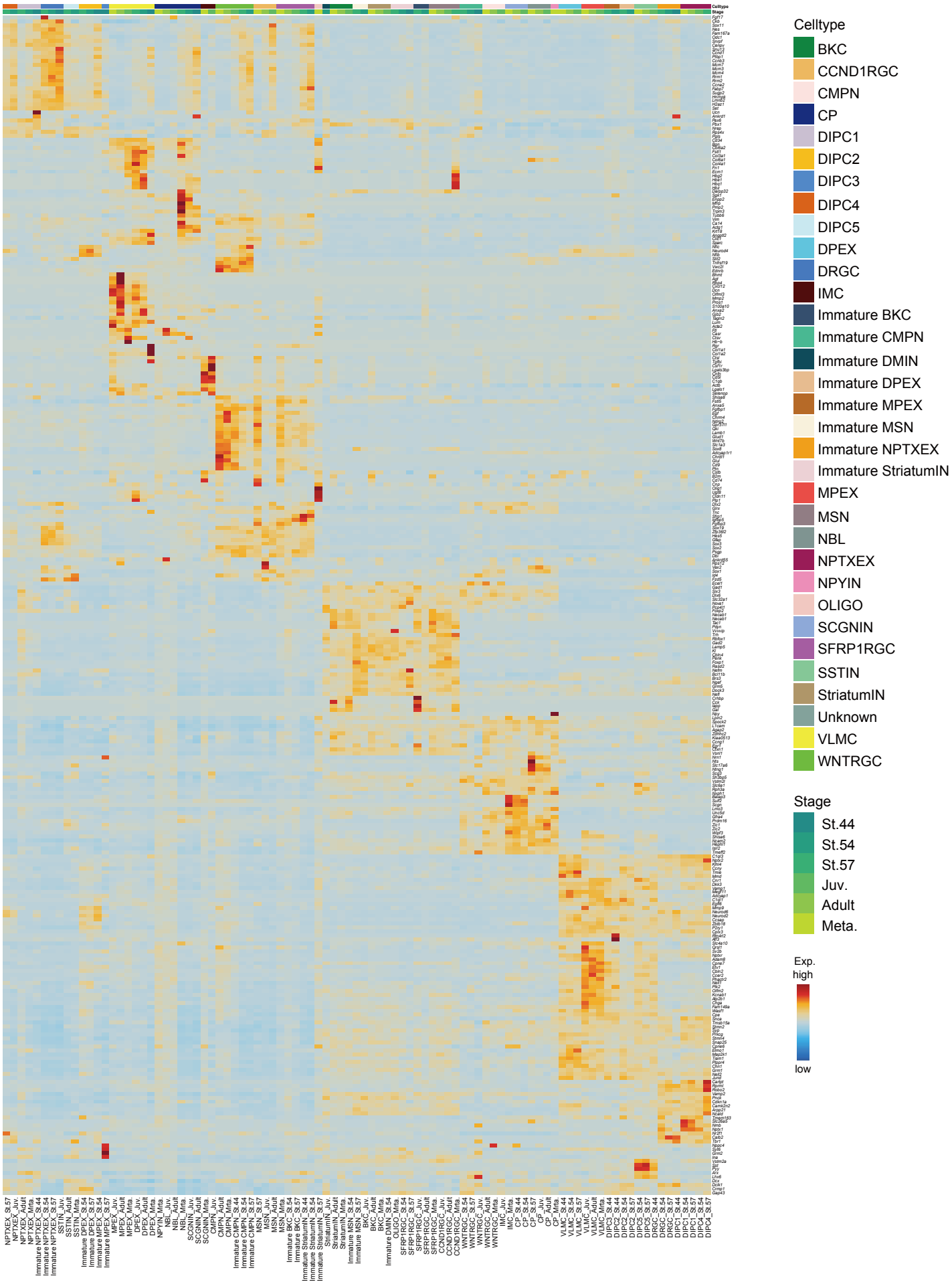
Celltype
Stage
Celltype
BKC
CCND1RGC
CMPN
CP
DIPC1
DIPC2
DIPC3
DIPC4
DIPC5
DPEX
DRGC
IMC
Immature BKC
Immature CMPN
Immature DMIN
Immature DPEX
Immature MPEX
Immature MSN
Immature NPTXEX
Immature StriatumIN
MPEX
MSN
NBL
NPTXEX
NPYIN
OLIGO
SCGNIN
SFRP1RGC
SSTIN
StriatumIN
Unknown
VLMC
WNTRGC
Stage
St.44
St.54
St.57
Juv.
Adult
Meta.
Exp.
high
low

Figure S6

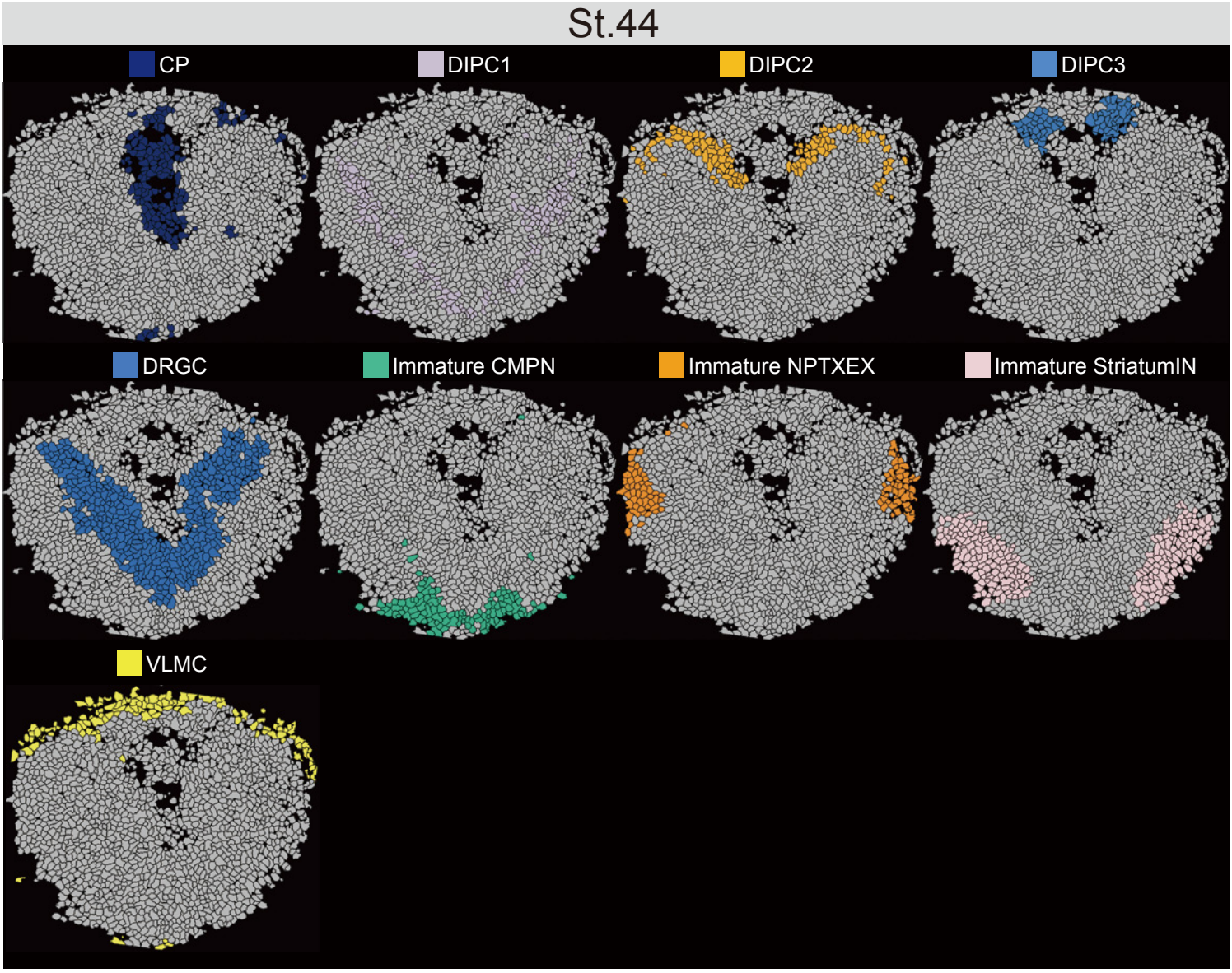
St.44
CP
DIPC1
DIPC2
DIPC3
DRGC
Immature CMPN
Immature NPTXEX
Immature StriatumIN
VLMC

Figure S7

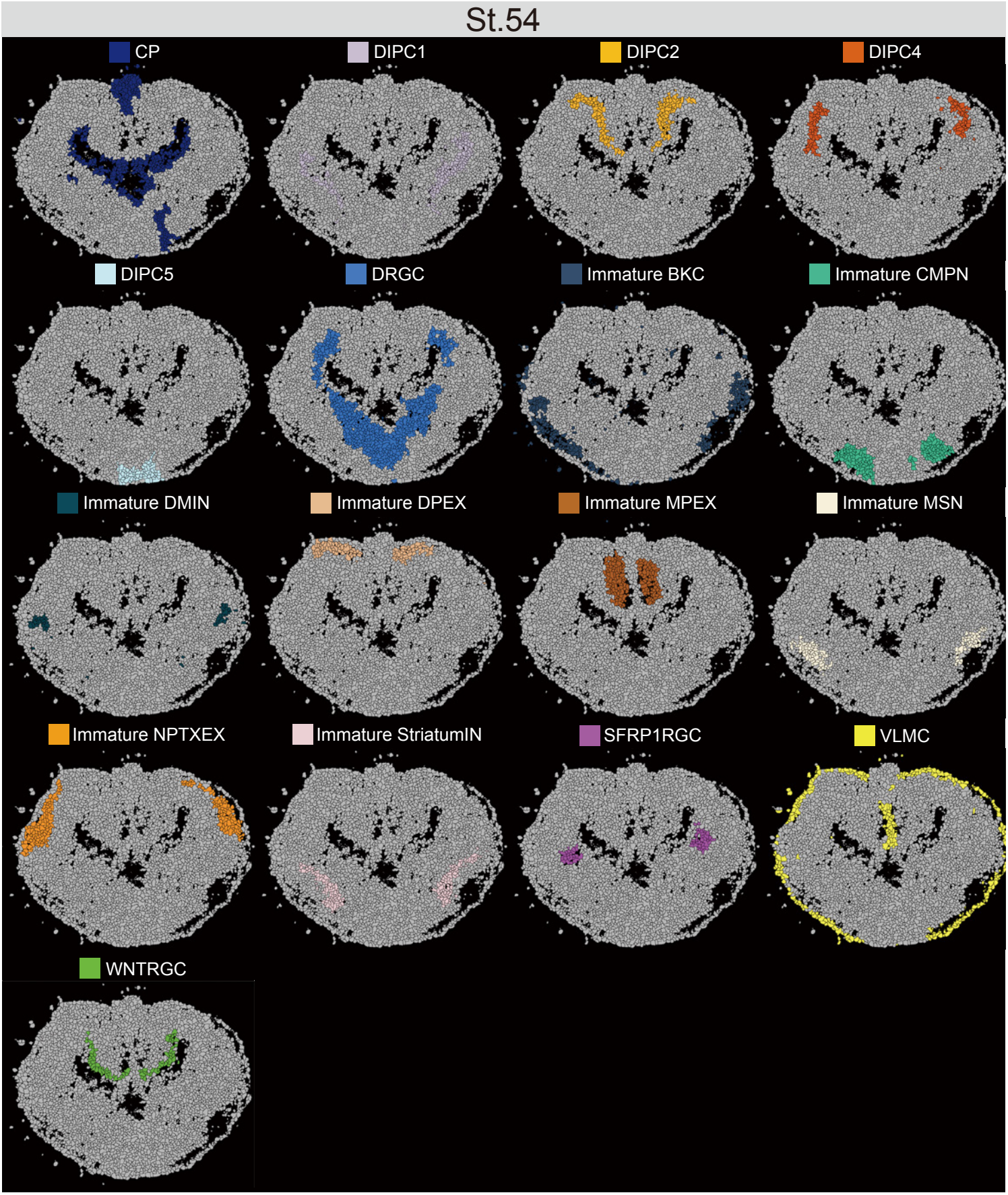
St.54
CP
DIPC1
DIPC2
DIPC4
DIPC5
DRGC
Immature BKC
Immature CMPN
Immature DMIN
Immature DPEX
Immature MPEX
Immature MSN
Immature NPTXEX
Immature StriatumIN
SFRP1RGC
VLMC
WNTRGC

Figure S8

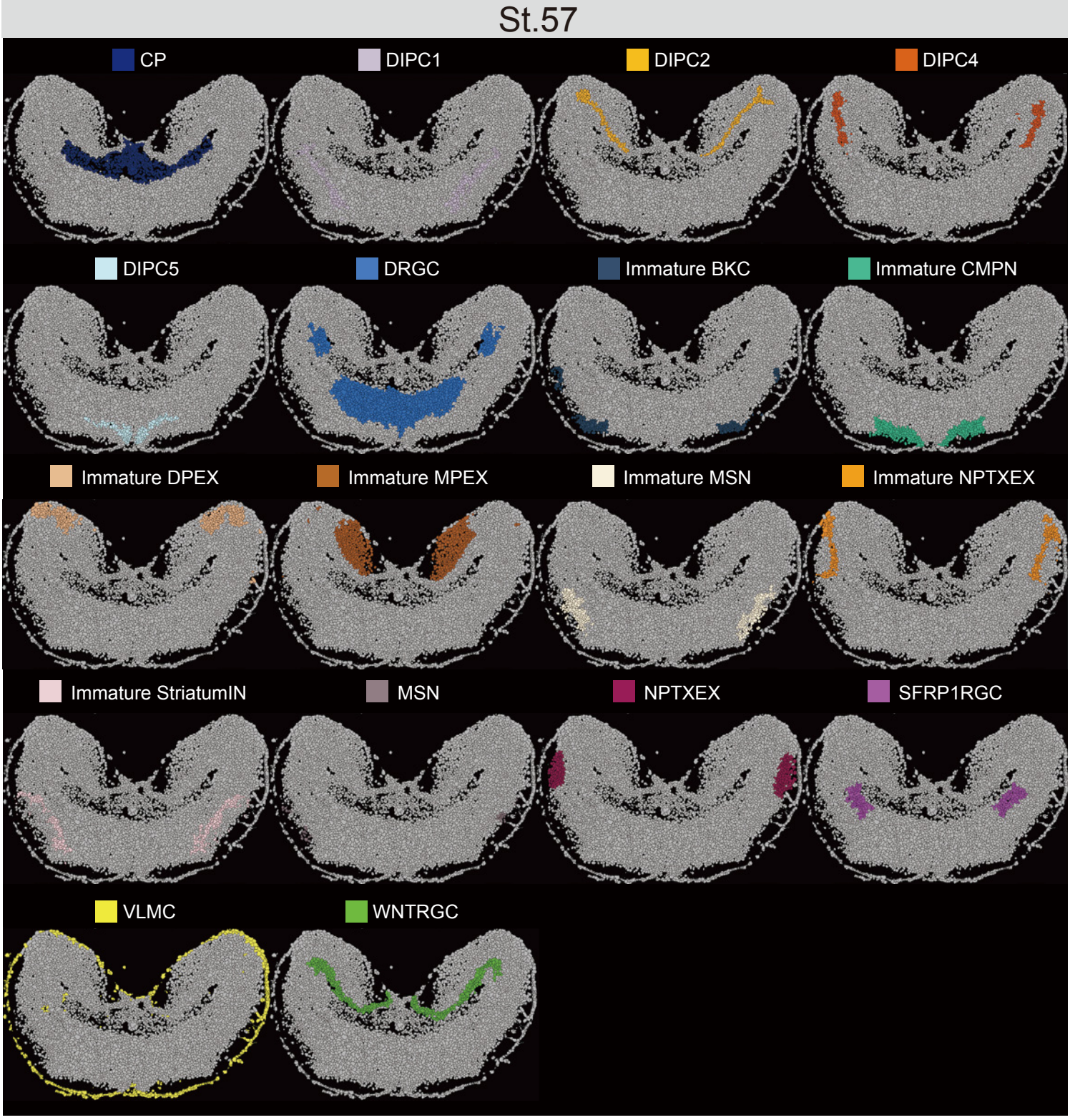
St.57
CP
DIPC1
DIPC2
DIPC4
DIPC5
DRGC
Immature BKC
Immature CMPN
Immature DPEX
Immature MPEX
Immature MSN
Immature NPTXEX
Immature StriatumIN
MSN
NPTXEX
SFRP1RGC
VLMC
WNTRGC

Figure S9

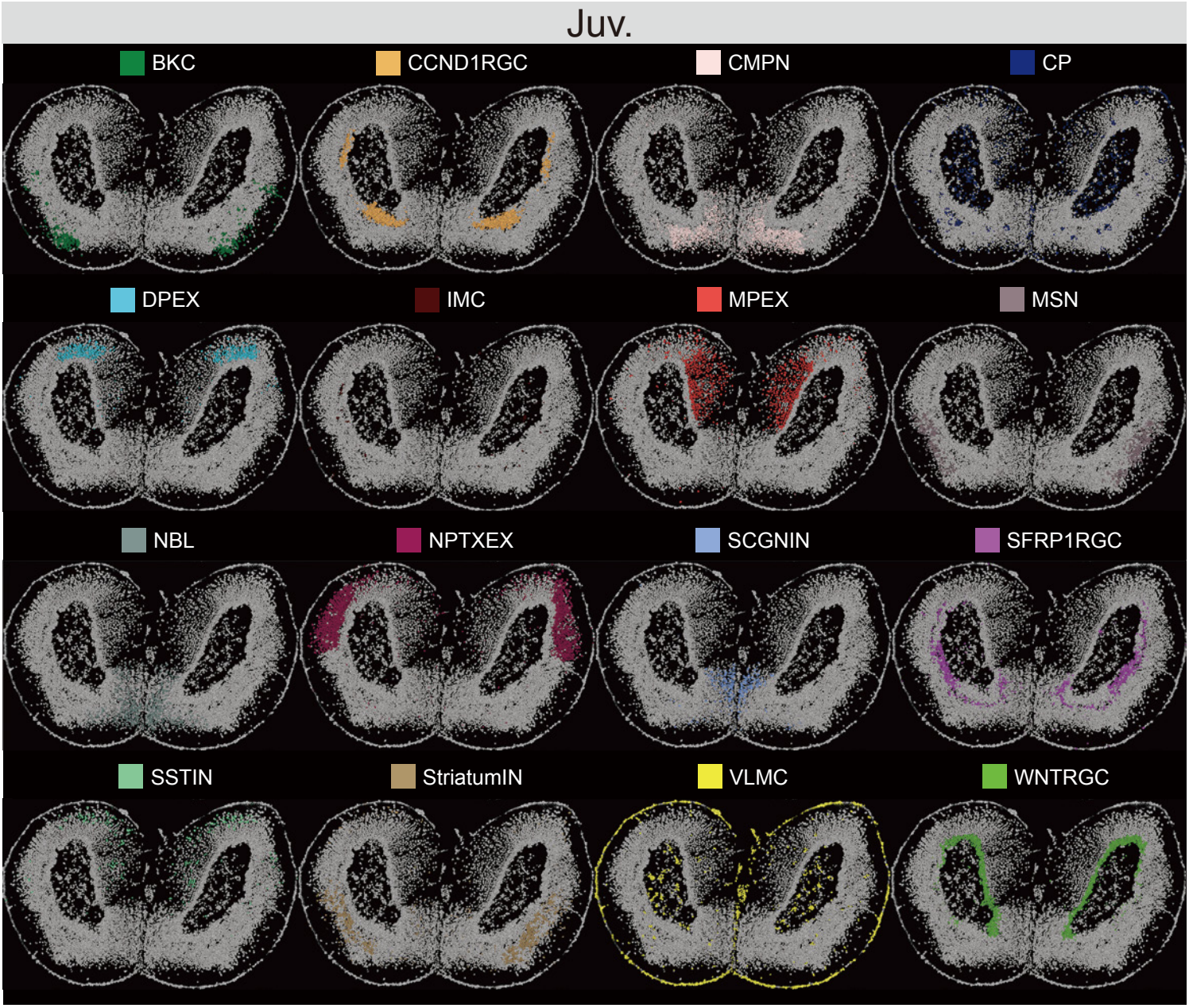
Juv.
BKC
CCND1RGC
CMPN
CP
DPEX
IMC
MPEX
MSN
NBL
NPTXEX
SCGNIN
SFRP1RGC
SSTIN
StriatumIN
VLMC
WNTRGC

Figure S10

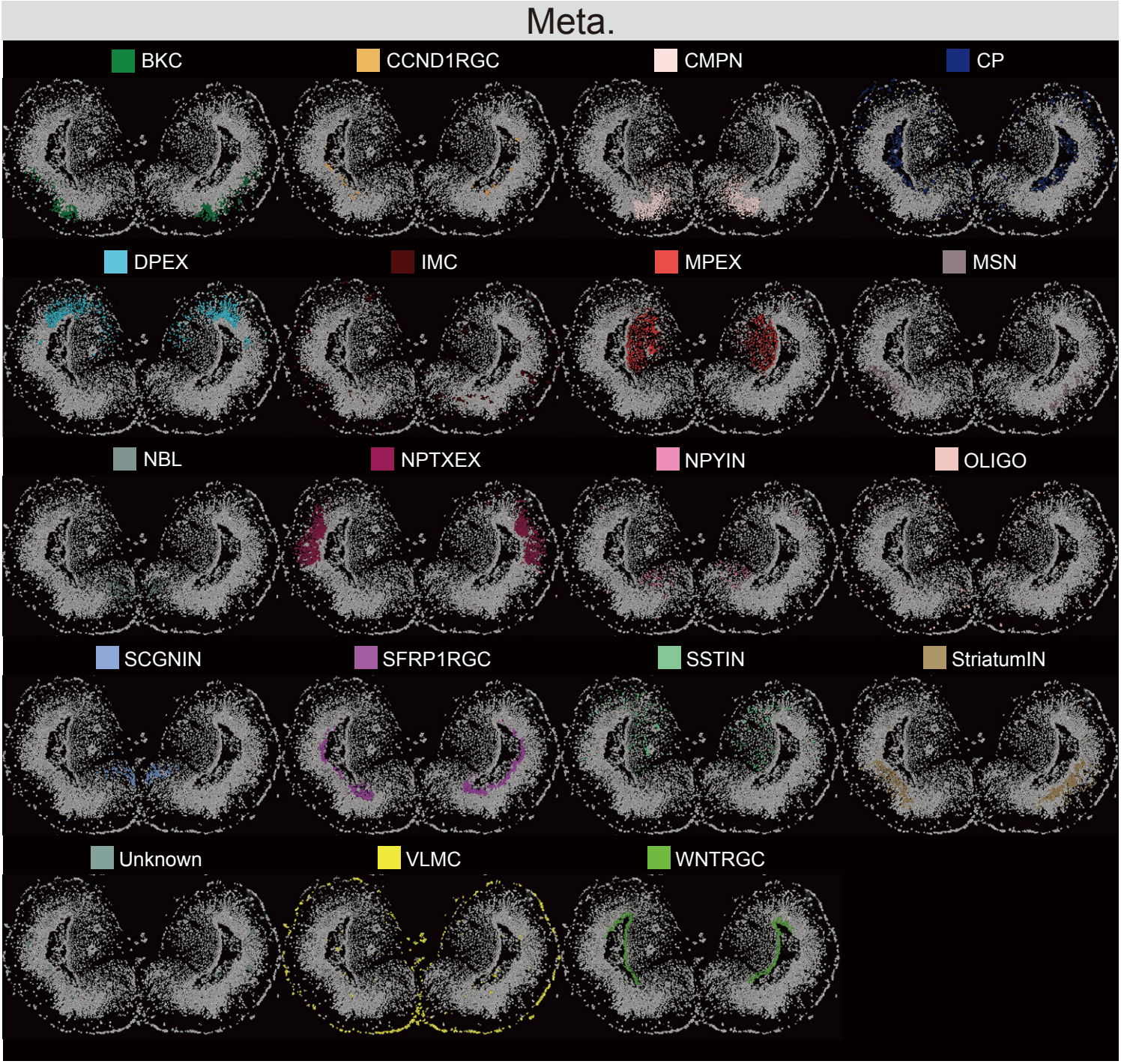
Meta.
BKC
CCND1RGC
CMPN
CP
DPEX
IMC
MPEX
MSN
NBL
NPTXEX
NPYIN
OLIGO
SCGNIN
SFRP1RGC
SSTIN
StriatumIN
Unknown
VLMC
WNTRGC

Figure S11

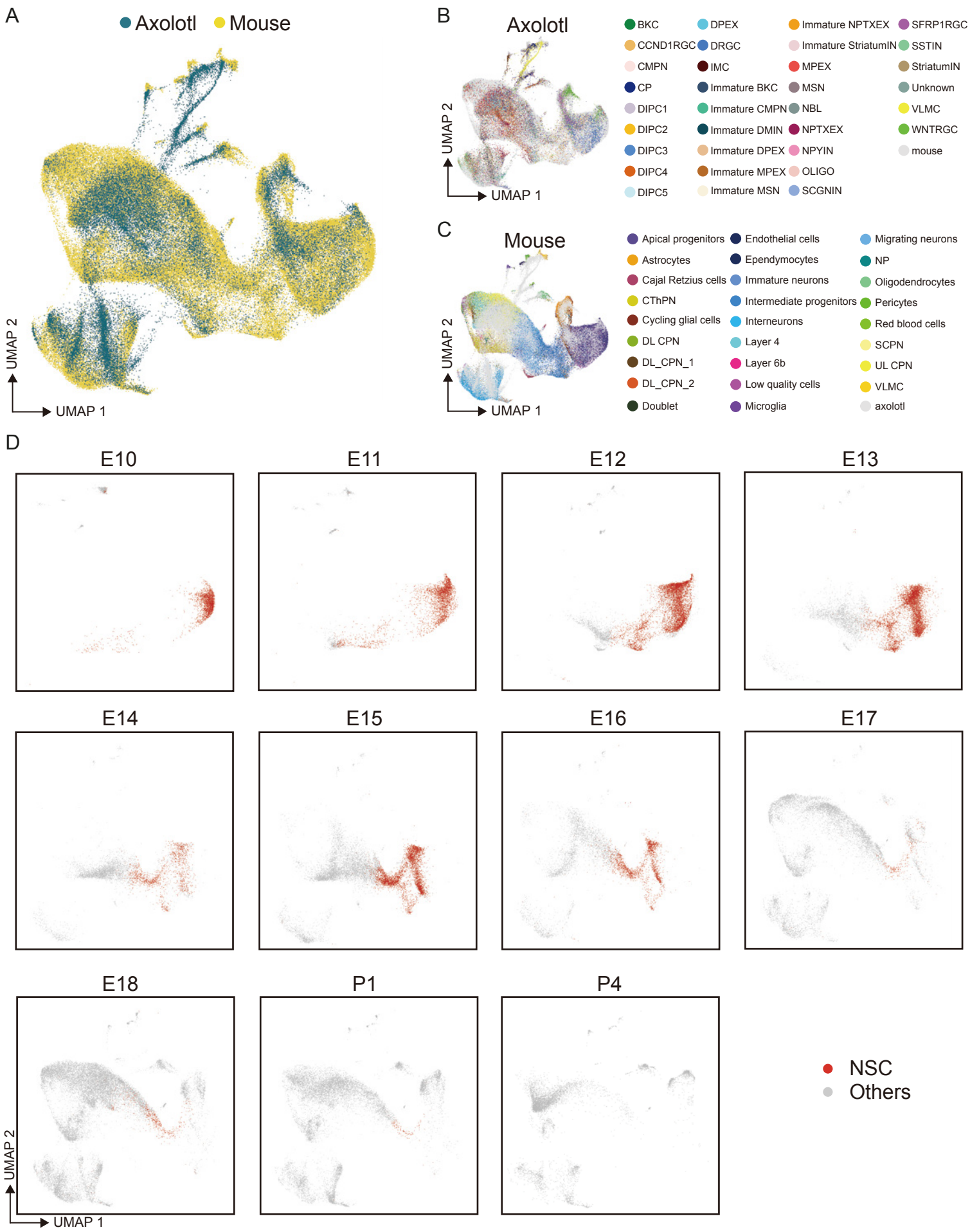
A
Axolotl
Mouse
UMAP 2
UMAP 1
B
Axolotl
UMAP 2
UMAP 1
BKC
CCND1RGC
CMPN
CP
DIPC1
DIPC2
DIPC3
DIPC4
DIPC5
DPEX
DRGC
IMC
Immature BKC
Immature CMPN
Immature DMIN
Immature DPEX
Immature MPEX
Immature MSN
Immature NPTXEX
Immature StriatumIN
MPEX
MSN
NBL
NPTXEX
NPYIN
OLIGO
SCGNIN
SFRP1RGC
SSTIN
StriatumIN
Unknown
VLMC
WNTRGC
mouse
C
Mouse
UMAP 2
UMAP 1
Apical progenitors
Astrocytes
Cajal Retzius cells
CThPN
Cycling glial cells
DL CPN
DL_CPN_1
DL_CPN_2
Doublet
Endothelial cells
Ependymocytes
Immature neurons
Intermediate progenitors
Interneurons
Layer 4
Layer 6b
Low quality cells
Microglia
Migrating neurons
NP
Oligodendrocytes
Pericytes
Red blood cells
SCPN
UL CPN
VLMC
axolotl
D
E10
E11
E12
E13
E14
E15
E16
E17
E18
P1
P4
UMAP 2
UMAP 1
NSC
Others

Figure S12

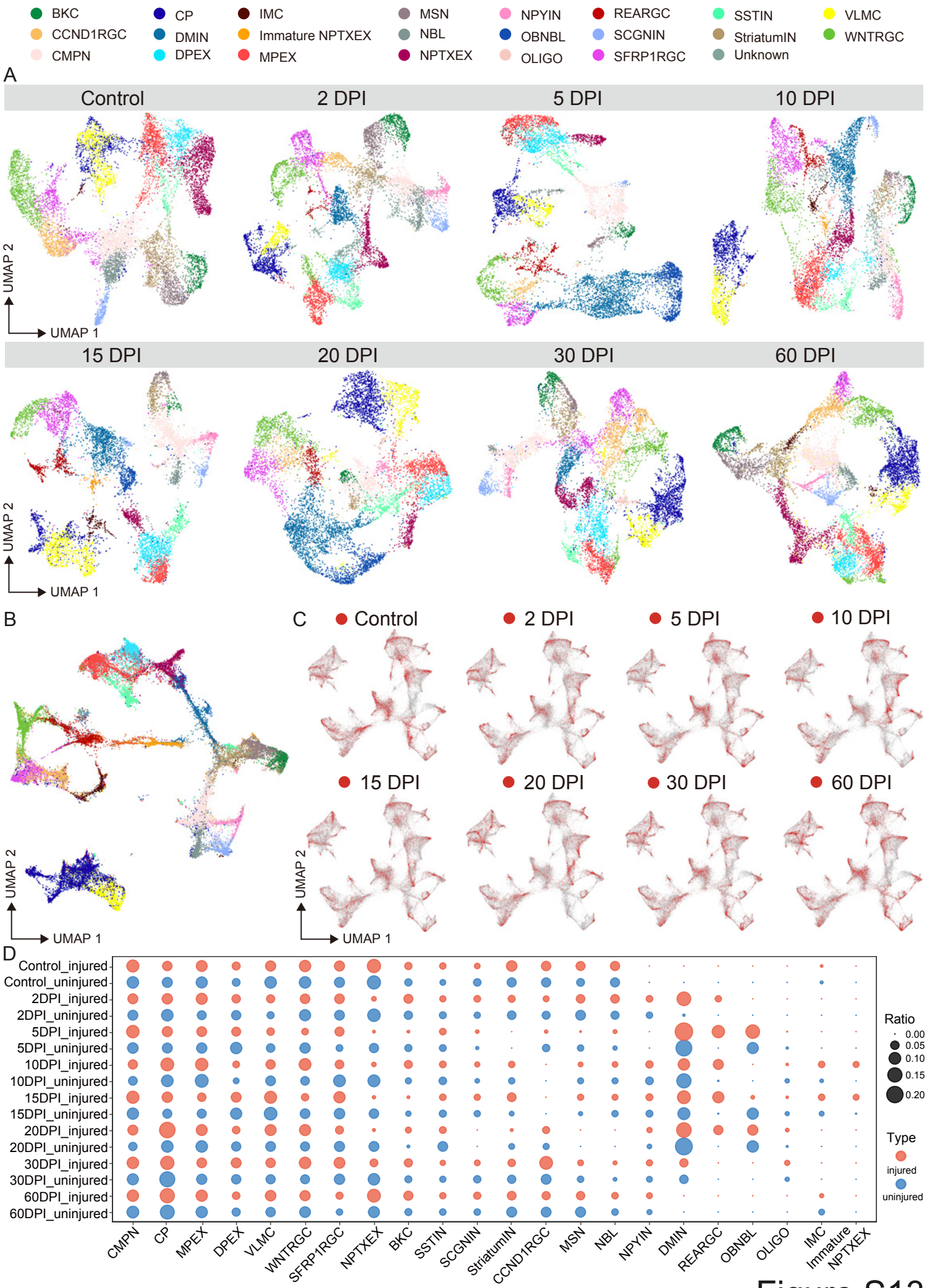
BKC
CCND1RGC
CMPN
CP
DMIN
DPEX
IMC
Immature NPTXEX
MPEX
MSN
NBL
NPTXEX
NPYIN
OBNBL
OLIGO
REARGC
SCGNIN
SFRP1RGC
SSTIN
StriatumIN
Unknown
VLMC
WNTRGC
A
Control
2 DPI
5 DPI
10 DPI
15 DPI
20 DPI
30 DPI
60 DPI
UMAP 2
UMAP 1
B
C
D
Control_injured
Control_uninjured
2DPI_injured
2DPI_uninjured
5DPI_injured
5DPI_uninjured
10DPI_injured
10DPI_uninjured
15DPI_injured
15DPI_uninjured
20DPI_injured
20DPI_uninjured
30DPI_injured
30DPI_uninjured
60DPI_injured
60DPI_uninjured
Ratio
0.00
0.05
0.10
0.15
0.20
Type
injured
uninjured

Figure S13

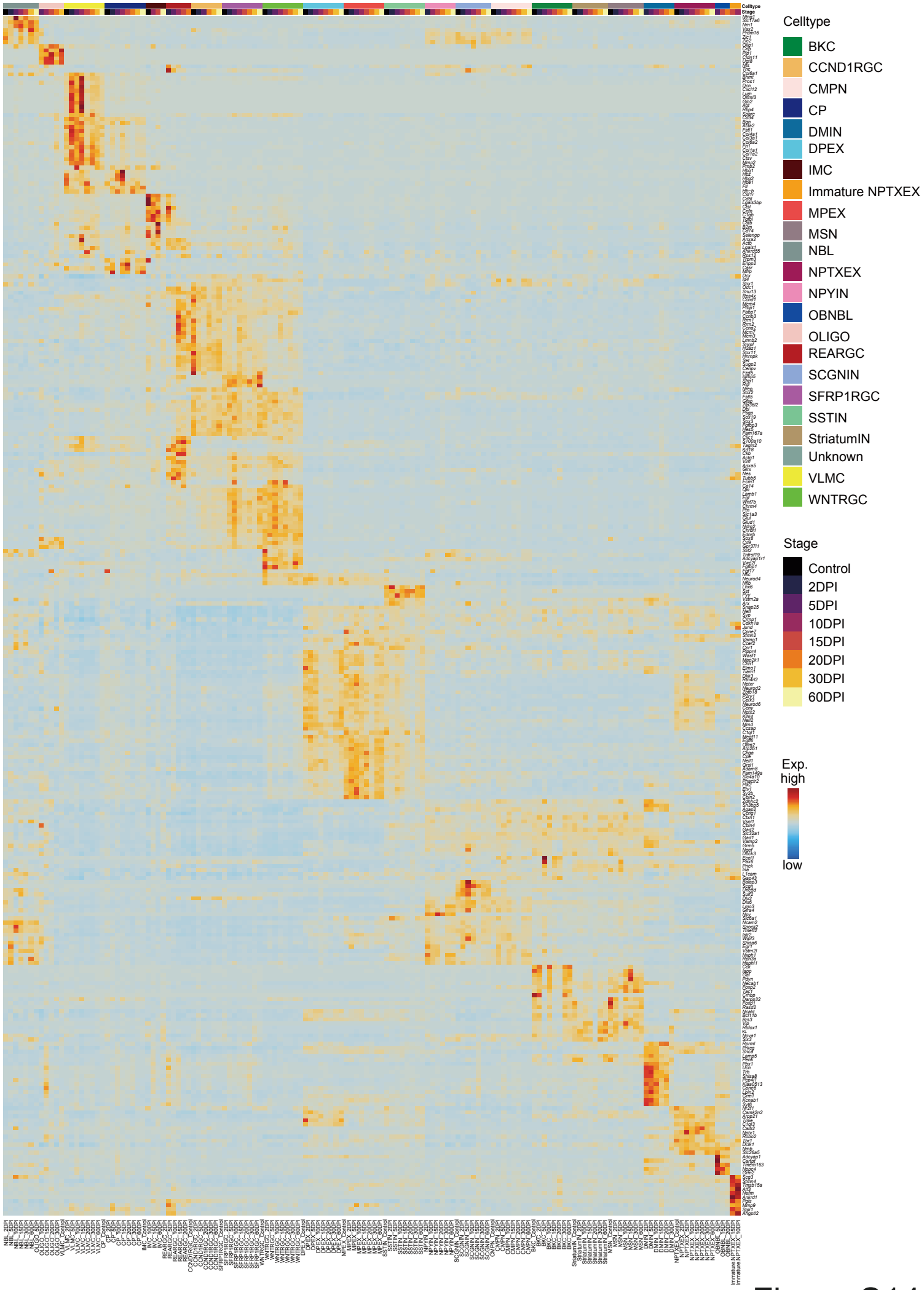
Celltype
BKC
CCND1RGC
CMPN
CP
DMIN
DPEX
IMC
Immature NPTXEX
MPEX
MSN
NBL
NPTXEX
NPYIN
OBNBL
OLIGO
REARGC
SCGNIN
SFRP1RGC
SSTIN
StriatumIN
Unknown
VLMC
WNTRGC
Stage
Control
2DPI
5DPI
10DPI
15DPI
20DPI
30DPI
60DPI
Exp.
high
low

Figure S14

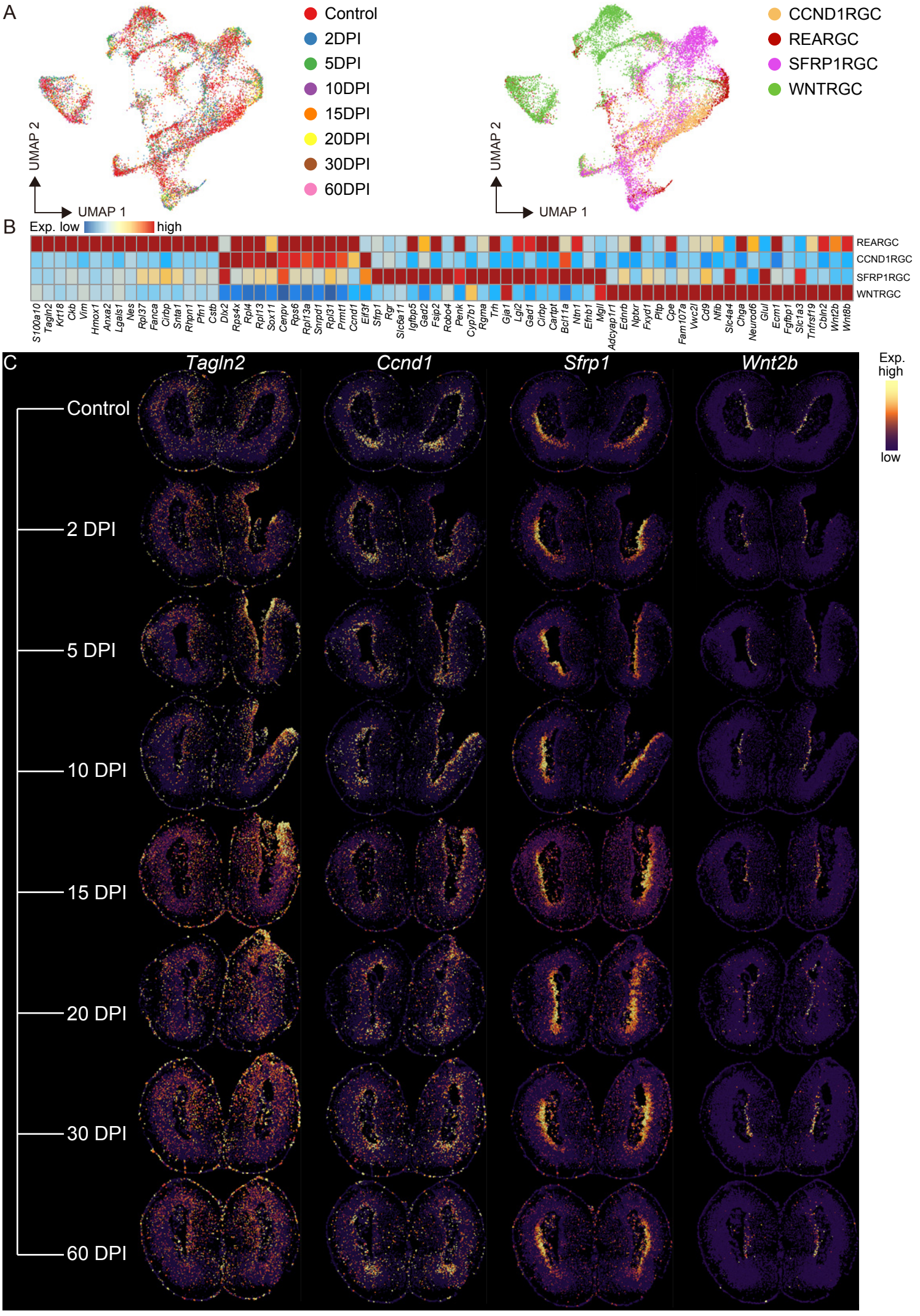
A
Control
2DPI
5DPI
10DPI
15DPI
20DPI
30DPI
60DPI
UMAP 2
UMAP 1
CCND1RGC
REARGC
SFRP1RGC
WNTRGC
B
Exp. low
high
REARGC
CCND1RGC
SFRP1RGC
WNTRGC
S100a10 Tagln2 Krt18 Ckb Vim Hmox1 Anxa2 Lgals1 Nes Rpl37 Fanca Cirbp Snta1 Rhpn1 Pfn1 Cstb Dlx2 Rps4x Rpl4 Rpl13 Sox11 Cenpv Rps6 Rpl13a Snrpd1 Rpl31 Prmt1 Ccnd1 Eif3f Sfrp1 Rgr Slc6a11 Igfbp5 Gad2 Fsip2 Robo4 Penk Cyp7b1 Rgma Trh Gja1 Lgi2 Gad1 Cirbp Cartpt Bcl11a Ntn1 Efnb1 Mgll Adcyap1r1 Ednrb Nptxr Fxyd1 Pltp Cpe Fam107a Vwc2l Cd9 Nfib Slc4a4 Chga Neurod6 Glul Ecm1 Fgfbp1 Slc1a3 Tnfrsf19 Cbln2 Wnt2b Wnt8b
C
Tagln2
Ccnd1
Sfrp1
Wnt2b
Control
2 DPI
5 DPI
10 DPI
15 DPI
20 DPI
30 DPI
60 DPI
Exp.
high
low

Figure S15

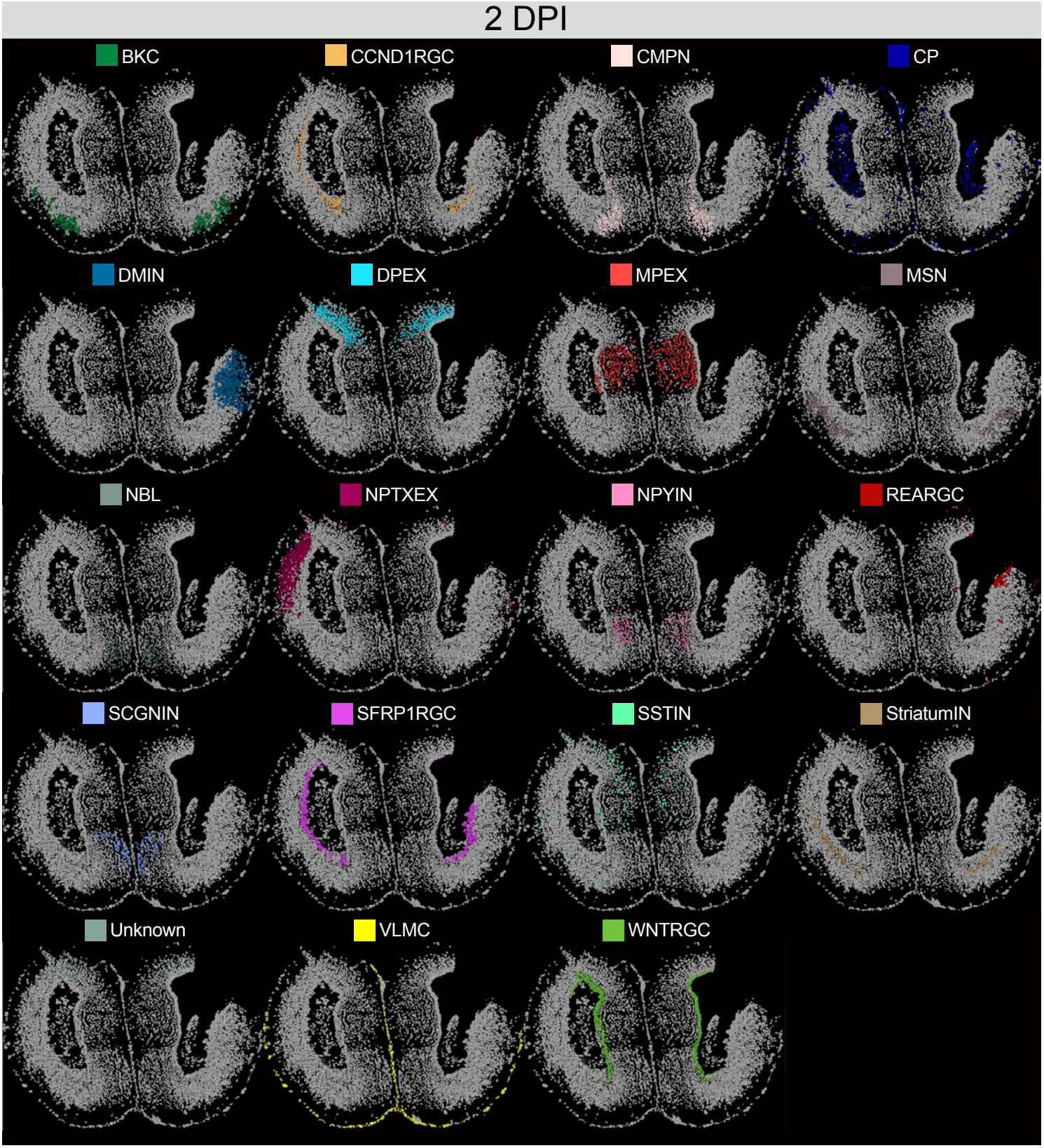
2 DPI
BKC
CCND1RGC
CMPN
CP
DMIN
DPEX
MPEX
MSN
NBL
NPTXEX
NPYIN
REARGC
SCGNIN
SFRP1RGC
SSTIN
StriatumIN
Unknown
VLMC
WNTRGC

Figure S16

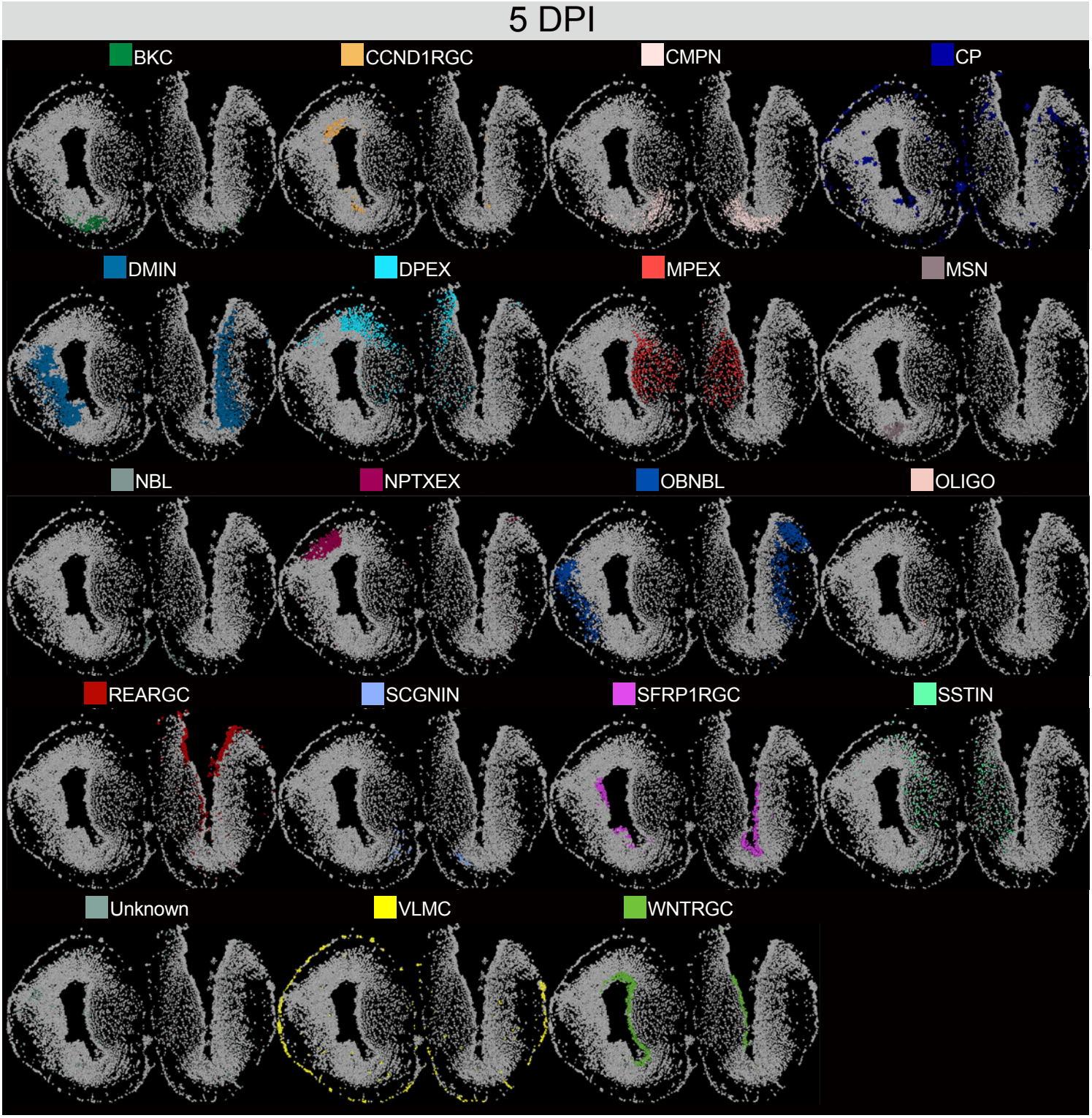
5 DPI
BKC
CCND1RGC
CMPN
CP
DMIN
DPEX
MPEX
MSN
NBL
NPTXEX
OBNBL
OLIGO
REARGC
SCGNIN
SFRP1RGC
SSTIN
Unknown
VLMC
WNTRGC

Figure S17

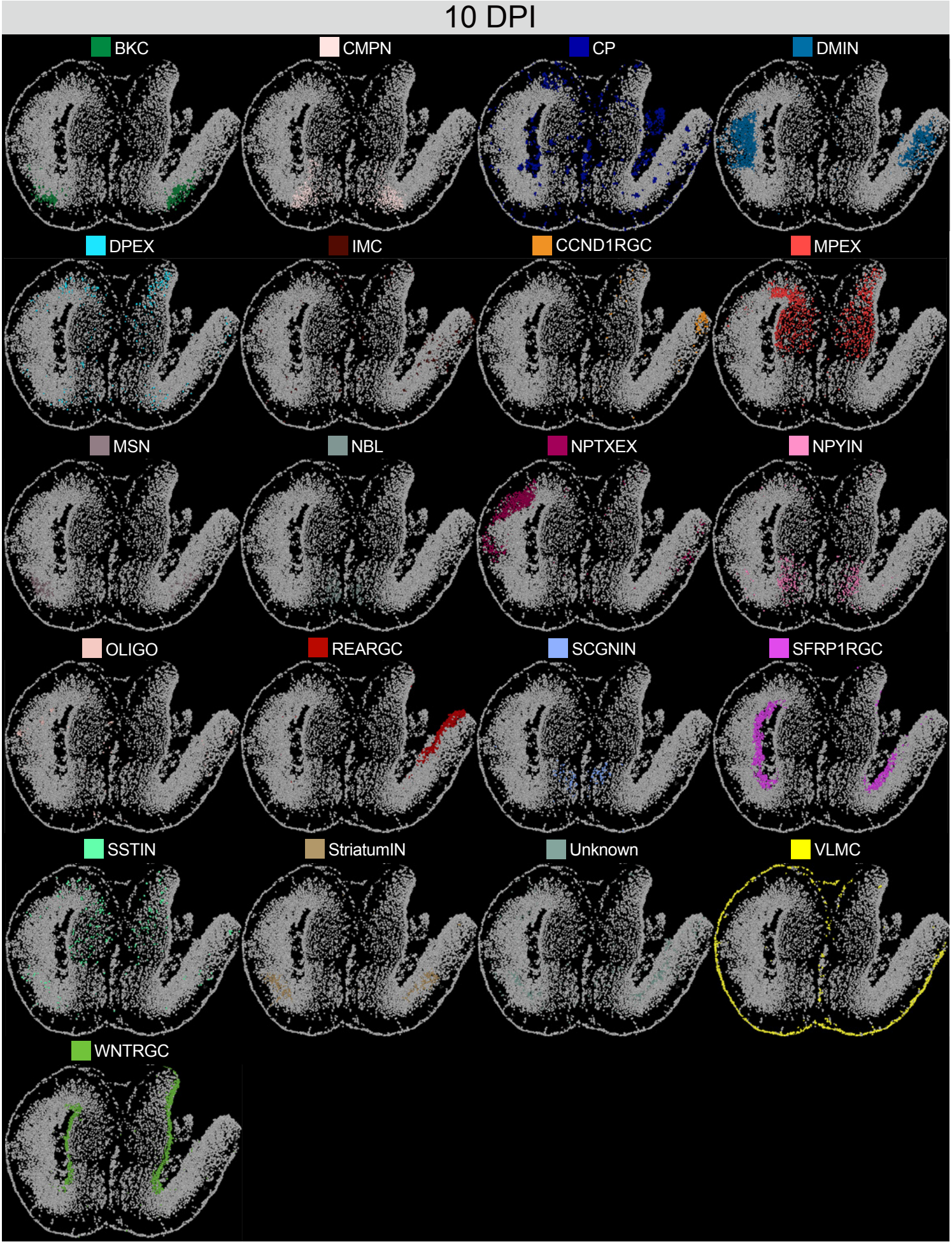
10 DPI
BKC
CMPN
CP
DMIN
DPEX
IMC
CCND1RGC
MPEX
MSN
NBL
NPTXEX
NPYIN
OLIGO
REARGC
SCGNIN
SFRP1RGC
SSTIN
StriatumIN
Unknown
VLMC
WNTRGC

Figure S18

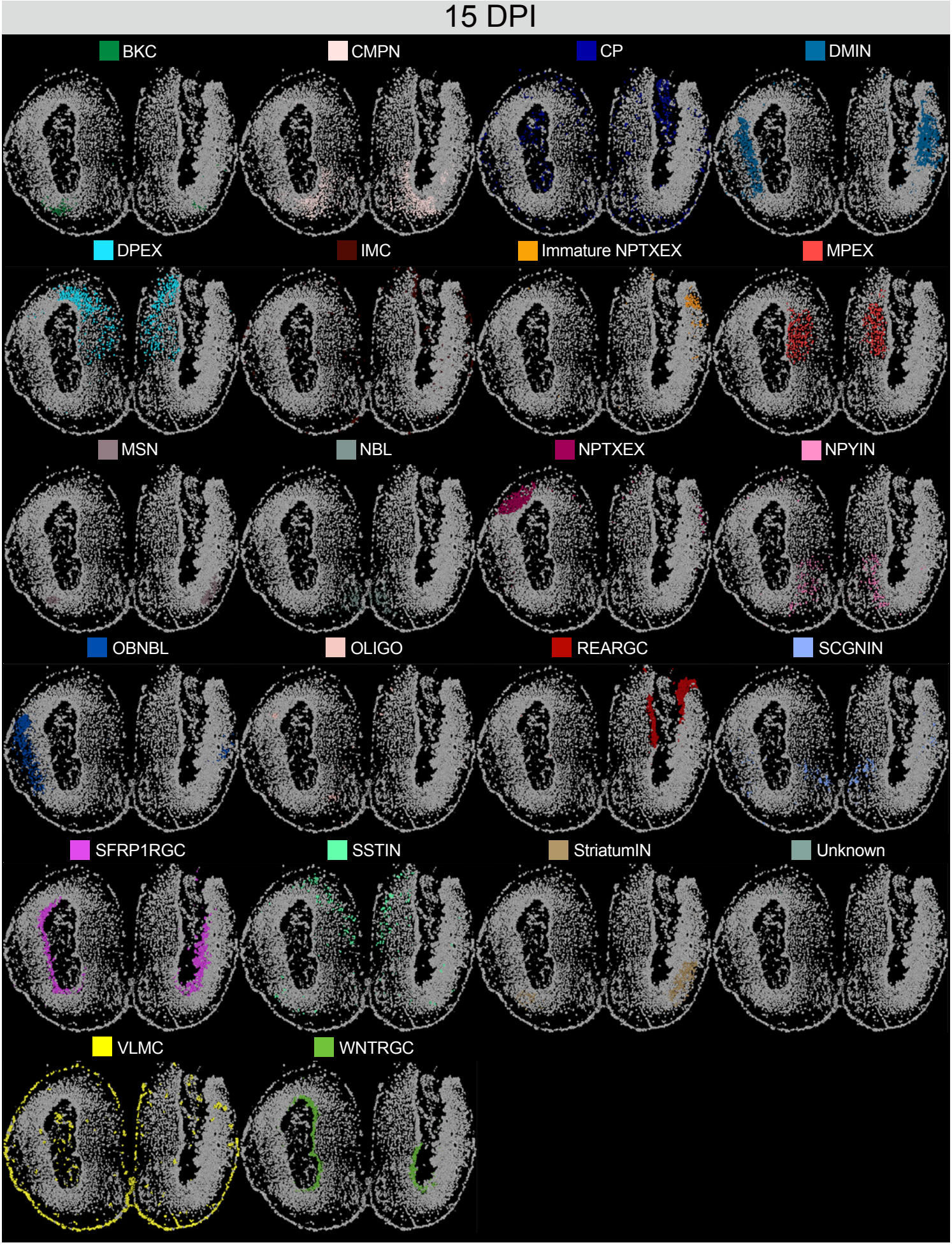
15 DPI
BKC
CMPN
CP
DMIN
DPEX
IMC
Immature NPTXEX
MPEX
MSN
NBL
NPTXEX
NPYIN
OBNBL
OLIGO
REARGC
SCGNIN
SFRP1RGC
SSTIN
StriatumIN
Unknown
VLMC
WNTRGC

Figure S19

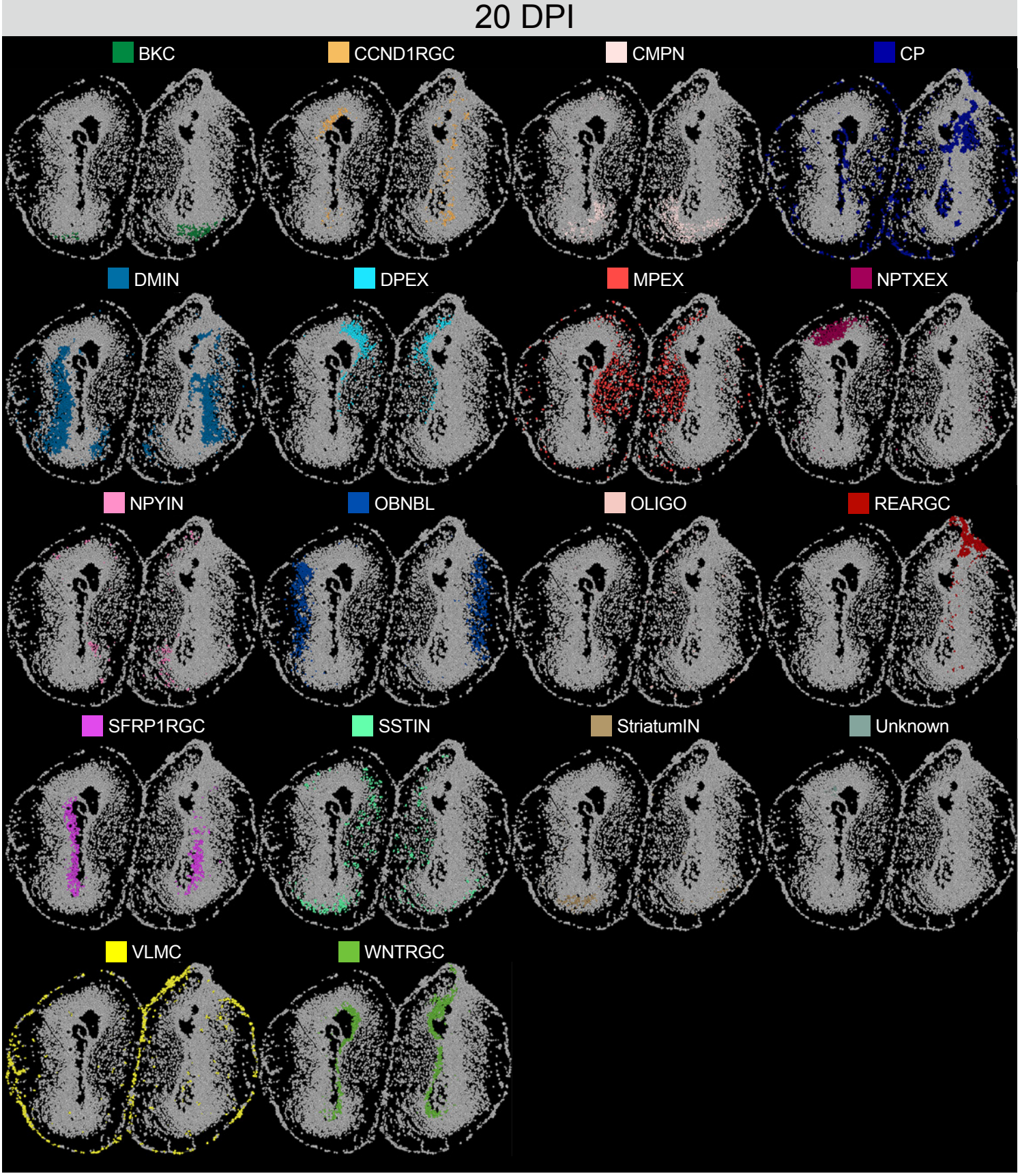
20 DPI
BKC
CCND1RGC
CMPN
CP
DMIN
DPEX
MPEX
NPTXEX
NPYIN
OBNBL
OLIGO
REARGC
SFRP1RGC
SSTIN
StriatumIN
Unknown
VLMC
WNTRGC

Figure 3-S20

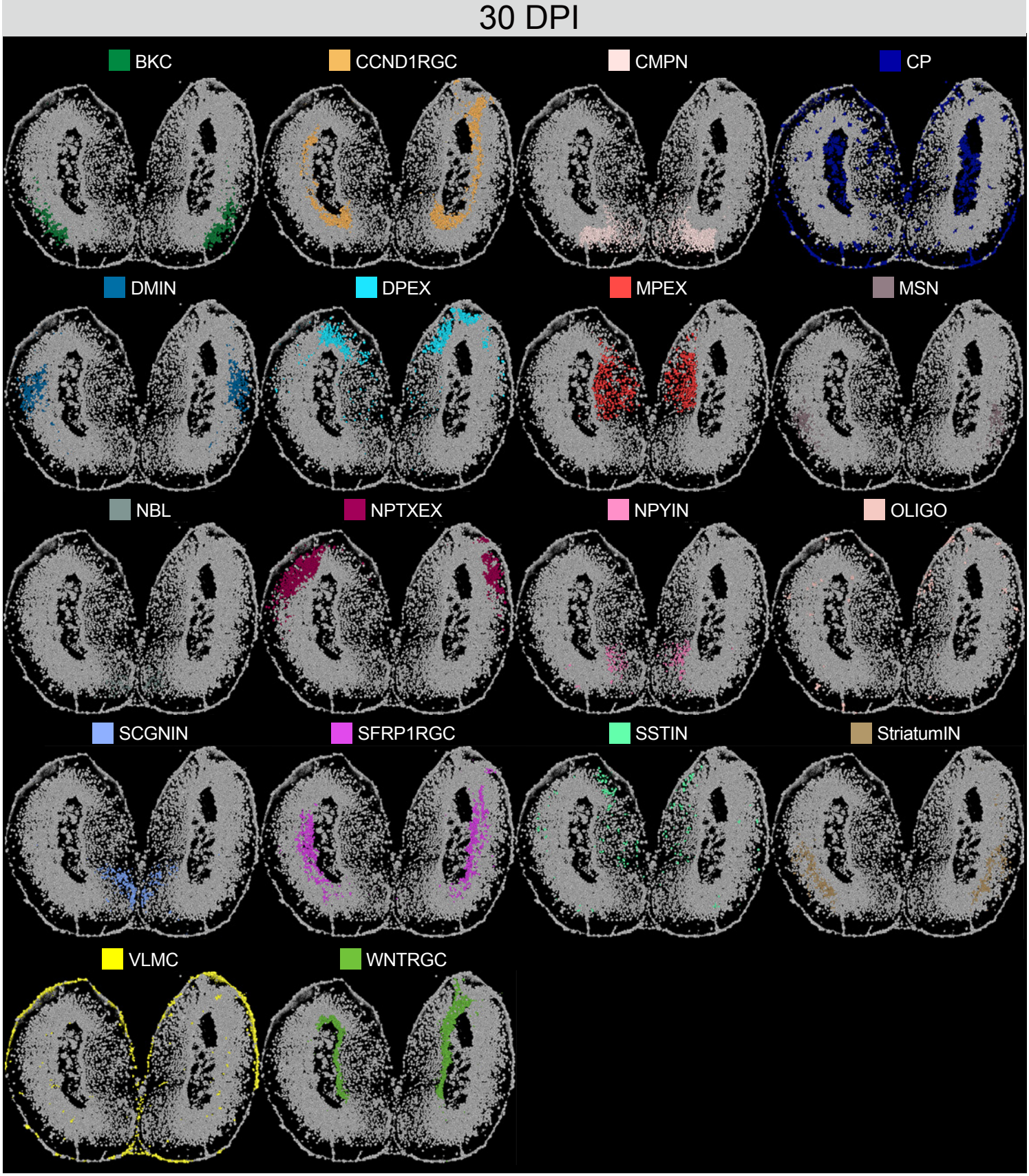
30 DPI
BKC
CCND1RGC
CMPN
CP
DMIN
DPEX
MPEX
MSN
NBL
NPTXEX
NPYIN
OLIGO
SCGNIN
SFRP1RGC
SSTIN
StriatumIN
VLMC
WNTRGC

Figure S21

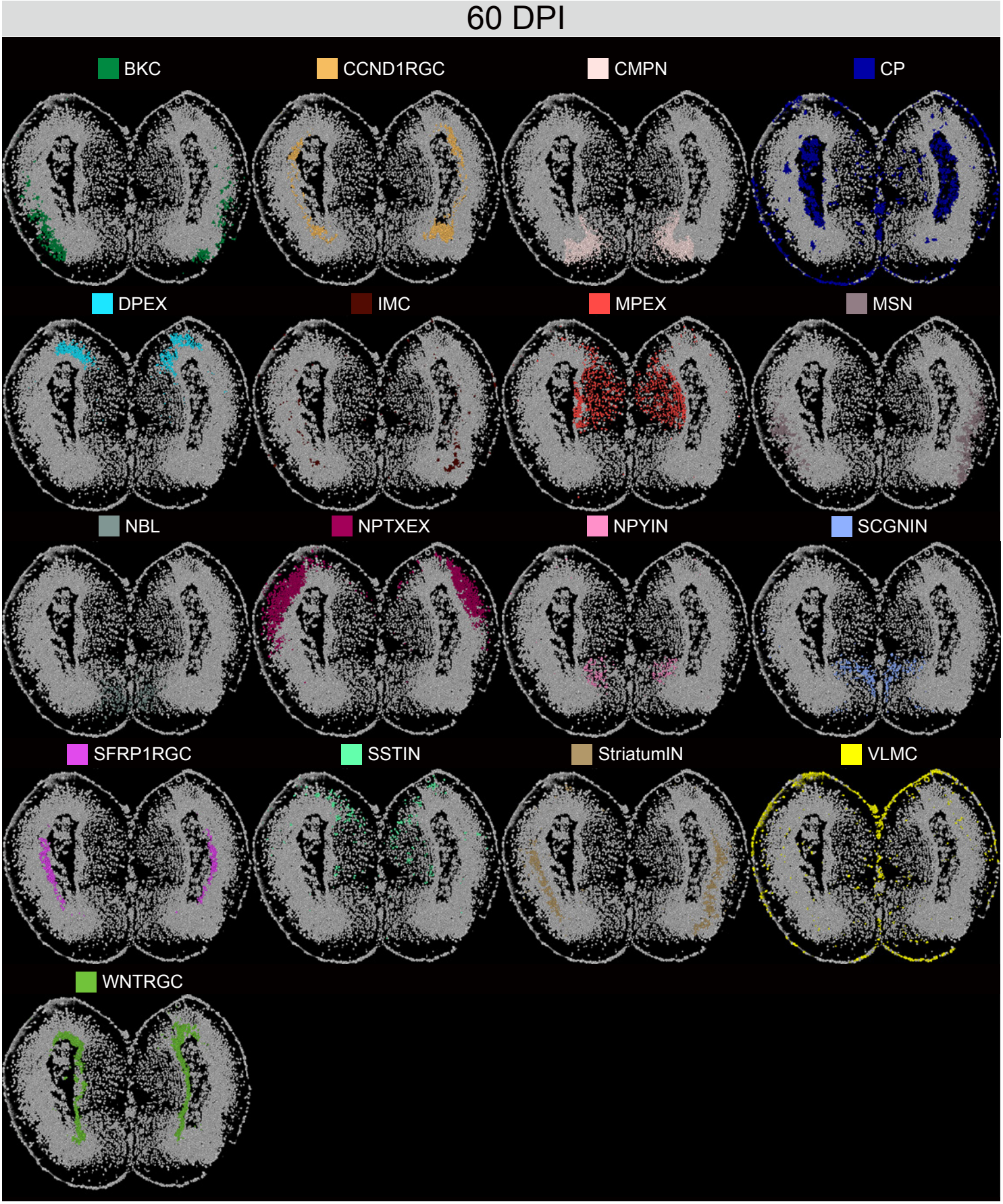
60 DPI
BKC
CCND1RGC
CMPN
CP
DPEX
IMC
MPEX
MSN
NBL
NPTXEX
NPYIN
SCGNIN
SFRP1RGC
SSTIN
StriatumIN
VLMC
WNTRGC

Figure S22

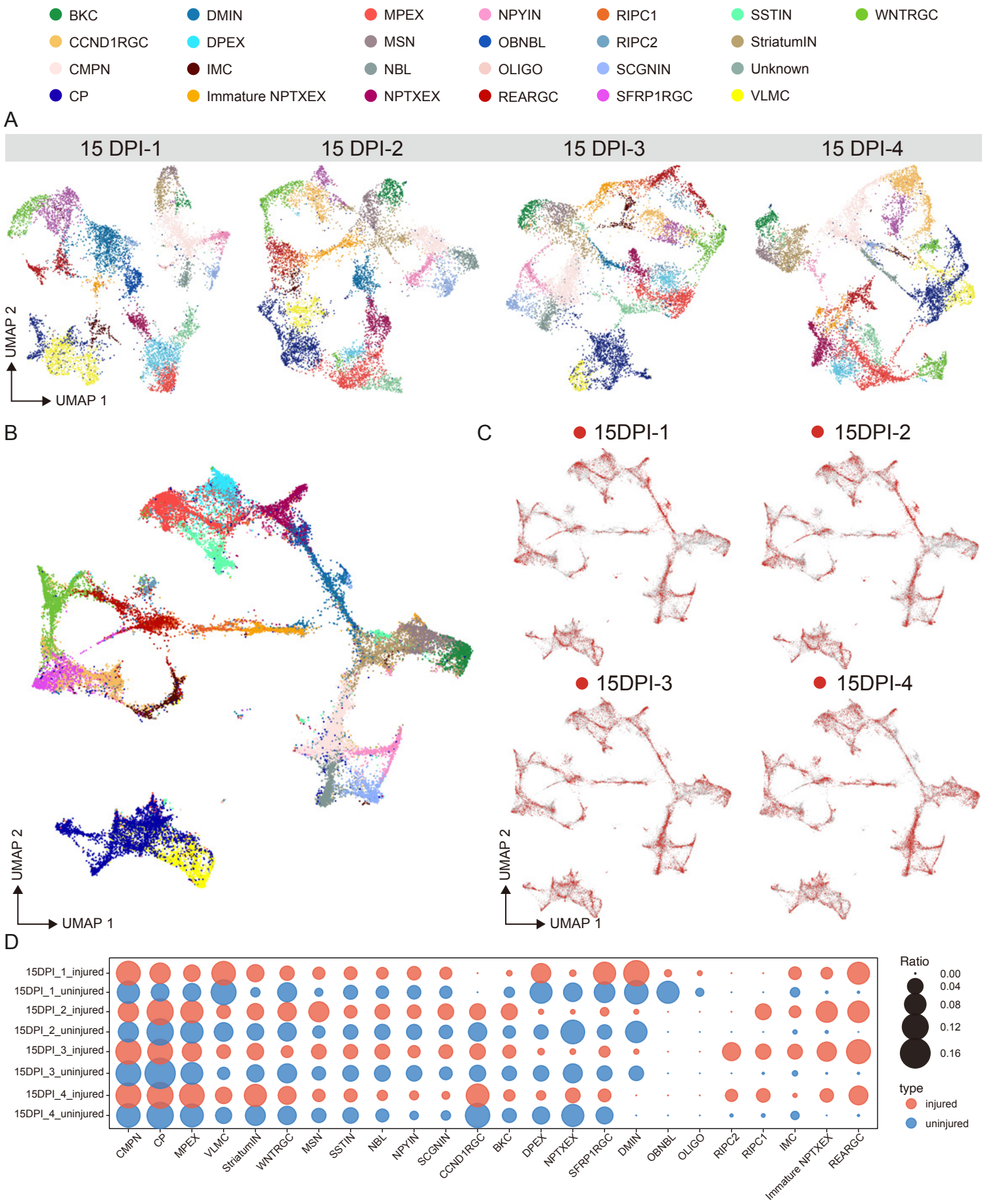
BKC
CCND1RGC
CMPN
CP
DMIN
DPEX
IMC
Immature NPTXEX
MPEX
MSN
NBL
NPTXEX
NPYIN
OBNBL
OLIGO
REARGC
RIPC1
RIPC2
SCGNIN
SFRP1RGC
SSTIN
StriatumIN
Unknown
VLMC
WNTRGC
A
15 DPI-1
15 DPI-2
15 DPI-3
15 DPI-4
UMAP 2
UMAP 1
B
UMAP 2
UMAP 1
C
15DPI-1
15DPI-2
15DPI-3
15DPI-4
UMAP 2
UMAP 1
D
15DPI_1_injured
15DPI_1_uninjured
15DPI_2_injured
15DPI_2_uninjured
15DPI_3_injured
15DPI_3_uninjured
15DPI_4_injured
15DPI_4_uninjured
CMPN
CP
MPEX
VLMC
StriatumIN
WNTRGC
MSN
SSTIN
NBL
NPYIN
SCGNIN
CCND1RGC
BKC
DPEX
NPTXEX
SFRP1RGC
DMIN
OBNBL
OLIGO
RIPC2
RIPC1
IMC
Immature NPTXEX
REARGC
Ratio
0.00
0.04
0.08
0.12
0.16
type
injured
uninjured

Figure S23

Celltype
Stage
Celltype
BKC
CCND1RGC
CMPN
CP
DMIN
DPEX
IMC
Immature NPTXEX
MPEX
MSN
NBL
NPTXEX
NPYIN
OBNBL
OLIGO
REARGC
RIPC1
RIPC2
SCGNIN
SFRP1RGC
SSTIN
StriatumIN
Unknown
VLMC
WNTRGC
Stage
15DPI-1
15DPI-2
15DPI-3
15DPI-4
Exp.
high
low

Figure S24

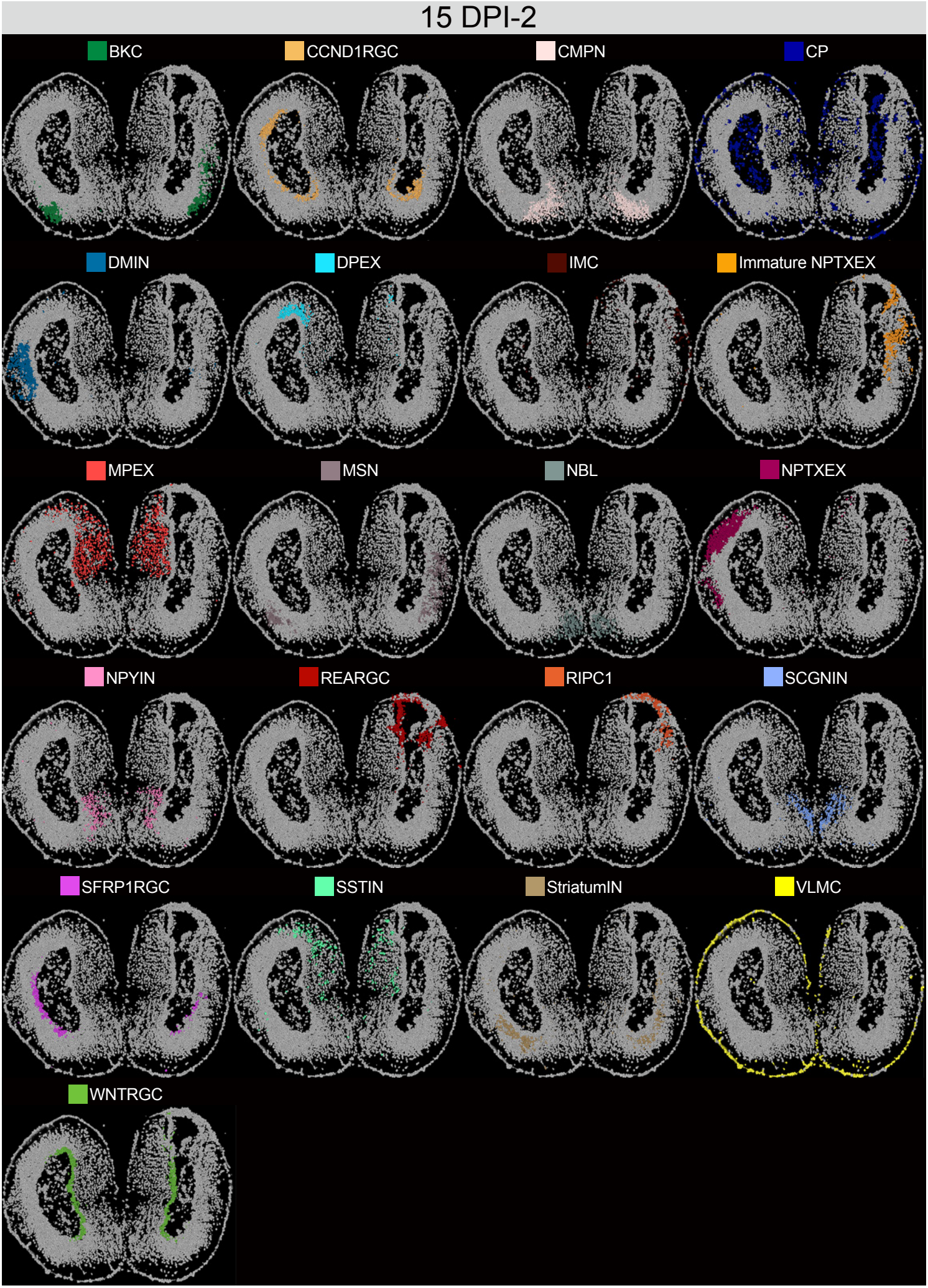
15 DPI-2
BKC
CCND1RGC
CMPN
CP
DMIN
DPEX
IMC
Immature NPTXEX
MPEX
MSN
NBL
NPTXEX
NPYIN
REARGC
RIPC1
SCGNIN
SFRP1RGC
SSTIN
StriatumIN
VLMC
WNTRGC

Figure S25

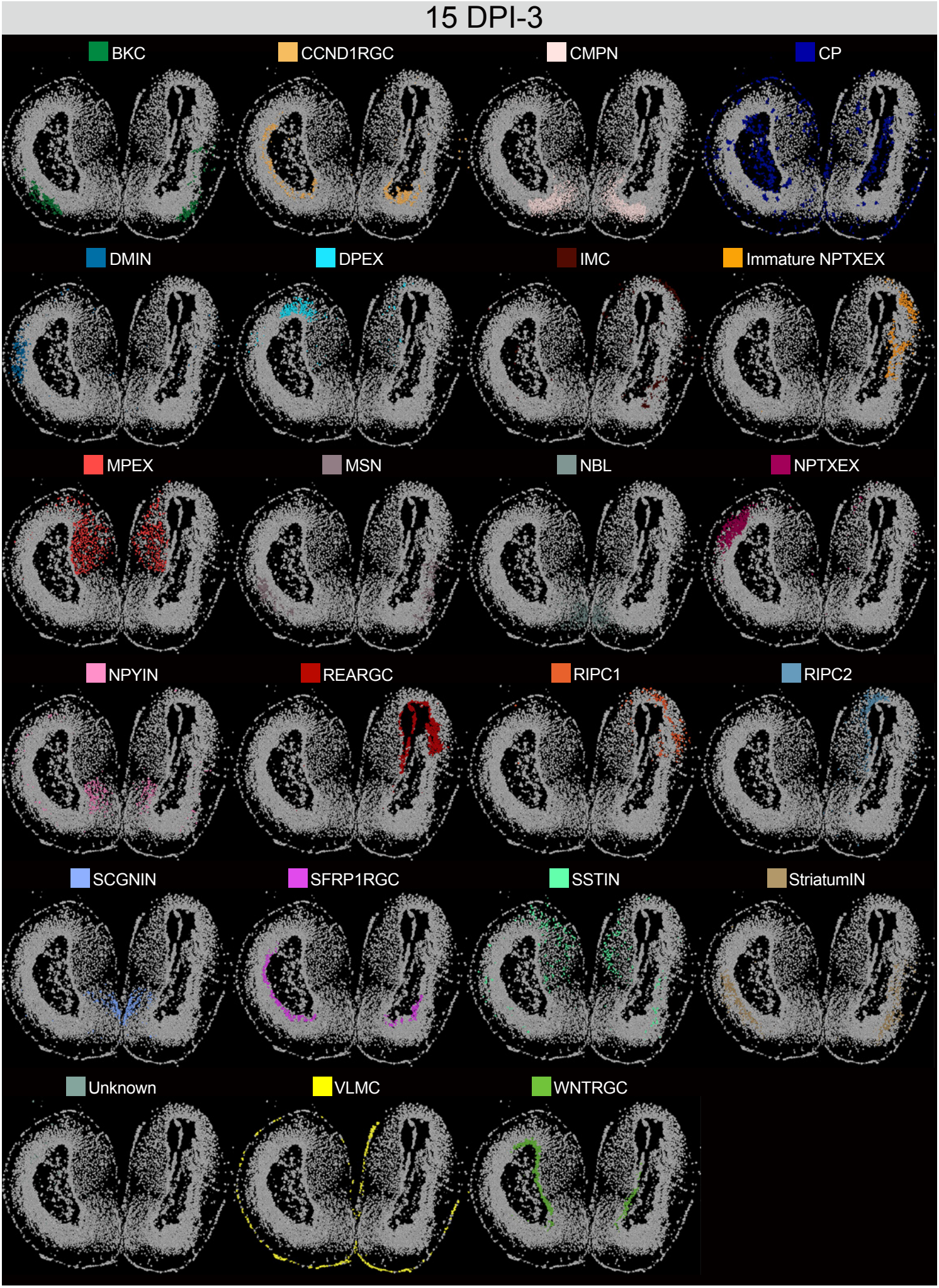
15 DPI-3
BKC
CCND1RGC
CMPN
CP
DMIN
DPEX
IMC
Immature NPTXEX
MPEX
MSN
NBL
NPTXEX
NPYIN
REARGC
RIPC1
RIPC2
SCGNIN
SFRP1RGC
SSTIN
StriatumIN
Unknown
VLMC
WNTRGC

Figure S26

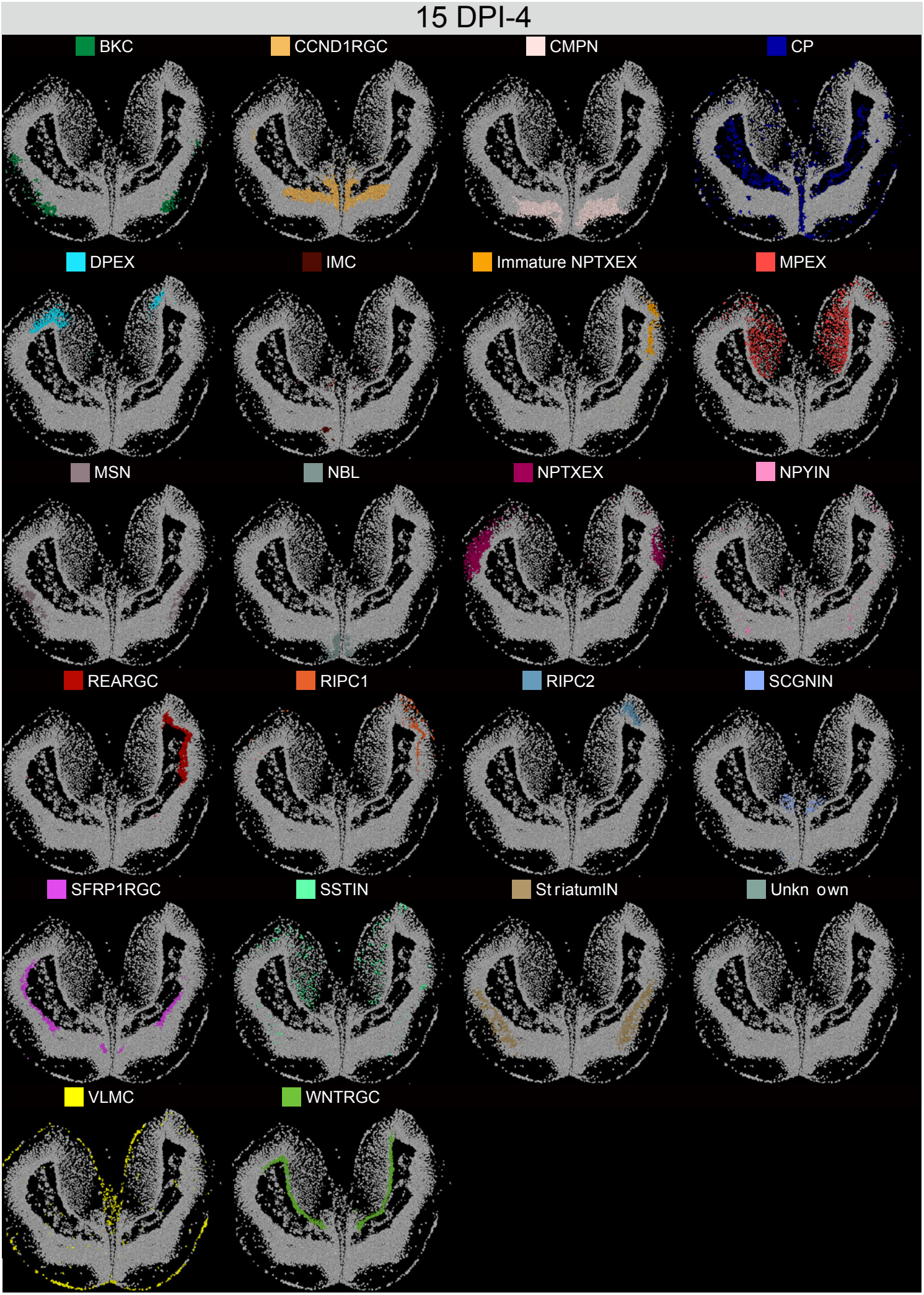
15 DPI-4
BKC
CCND1RGC
CMPN
CP
DPEX
IMC
Immature NPTXEX
MPEX
MSN
NBL
NPTXEX
NPYIN
REARGC
RIPC1
RIPC2
SCGNIN
SFRP1RGC
SSTIN
StriatumIN
Unknown
VLMC
WNTRGC

Figure S27

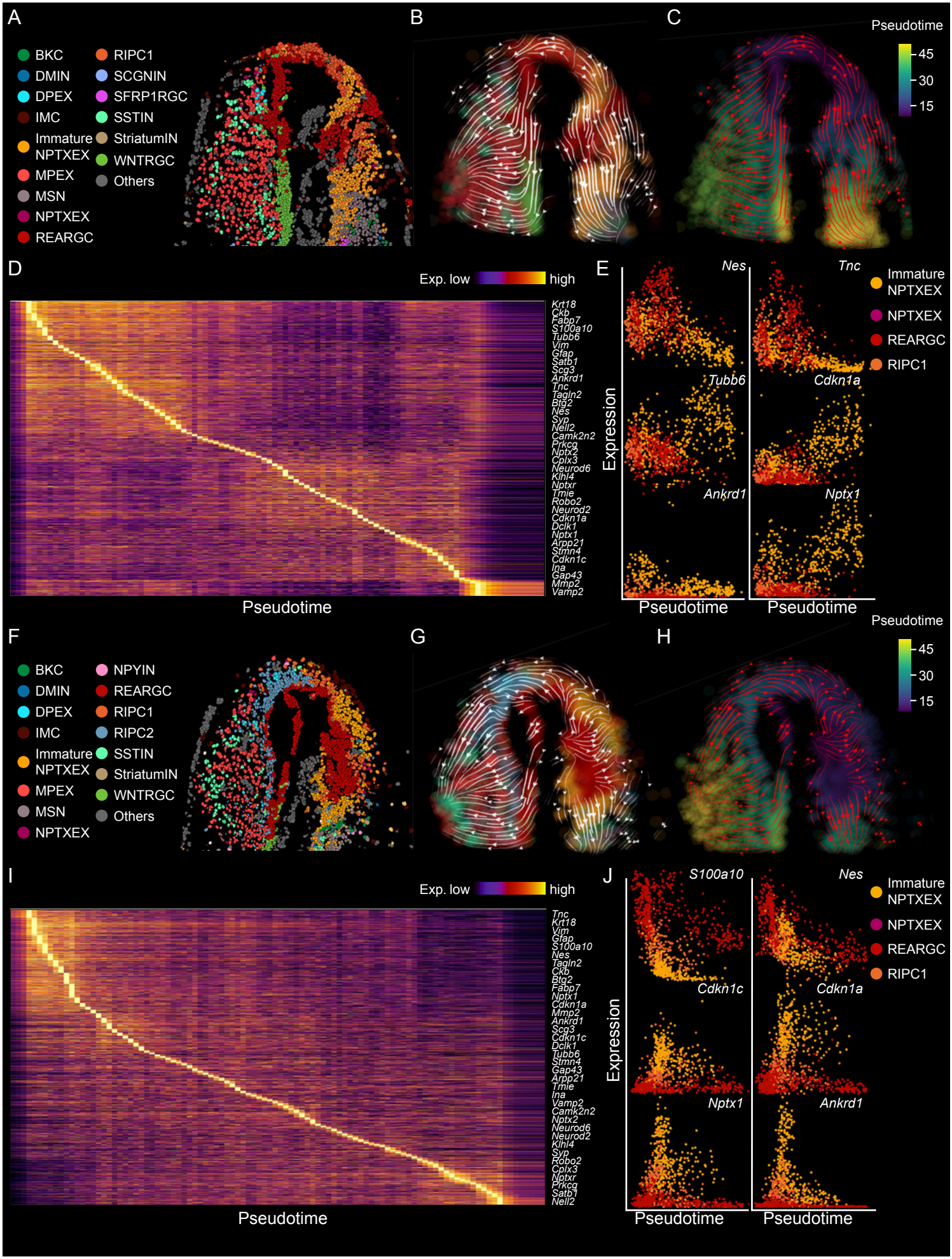
A
BKC
DMIN
DPEX
IMC
Immature NPTXEX
MPEX
MSN
NPTXEX
REARGC
RIPC1
SCGNIN
SFRP1RGC
SSTIN
StriatumIN
WNTRGC
Others
B
C
Pseudotime
45
30
15
D
Exp. low
high
Krt18
Ckb
Fabp7
S100a10
Tubb6
Vim
Gfap
Satb1
Scg3
Ankrd1
Tnc
Tagln2
Btg2
Nes
Syp
Nell2
Camk2n2
Prkcg
Nptx2
Cplx3
Neurod6
Klhl4
Nptxr
Tmie
Robo2
Neurod2
Cdkn1a
Dclk1
Nptx1
Arpp21
Stmn4
Cdkn1c
Ina
Gap43
Mmp2
Vamp2
Pseudotime
E
Nes
Tnc
Tubb6
Cdkn1a
Ankrd1
Nptx1
Expression
Pseudotime
Pseudotime
Immature NPTXEX
NPTXEX
REARGC
RIPC1
F
BKC
DMIN
DPEX
IMC
Immature NPTXEX
MPEX
MSN
NPTXEX
NPYIN
REARGC
RIPC1
RIPC2
SSTIN
StriatumIN
WNTRGC
Others
G
H
Pseudotime
45
30
15
I
Exp. low
high
Tnc
Krt18
Vim
Gfap
S100a10
Nes
Tagln2
Ckb
Btg2
Fabp7
Nptx1
Cdkn1a
Mmp2
Ankrd1
Scg3
Cdkn1c
Dclk1
Tubb6
Stmn4
Gap43
Arpp21
Tmie
Ina
Vamp2
Camk2n2
Nptx2
Neurod6
Neurod2
Klhl4
Syp
Robo2
Cplx3
Nptxr
Prkcg
Satb1
Nell2
Pseudotime
J
S100a10
Nes
Cdkn1c
Cdkn1a
Nptx1
Ankrd1
Expression
Pseudotime
Pseudotime
Immature NPTXEX
NPTXEX
REARGC
RIPC1

Figure S28

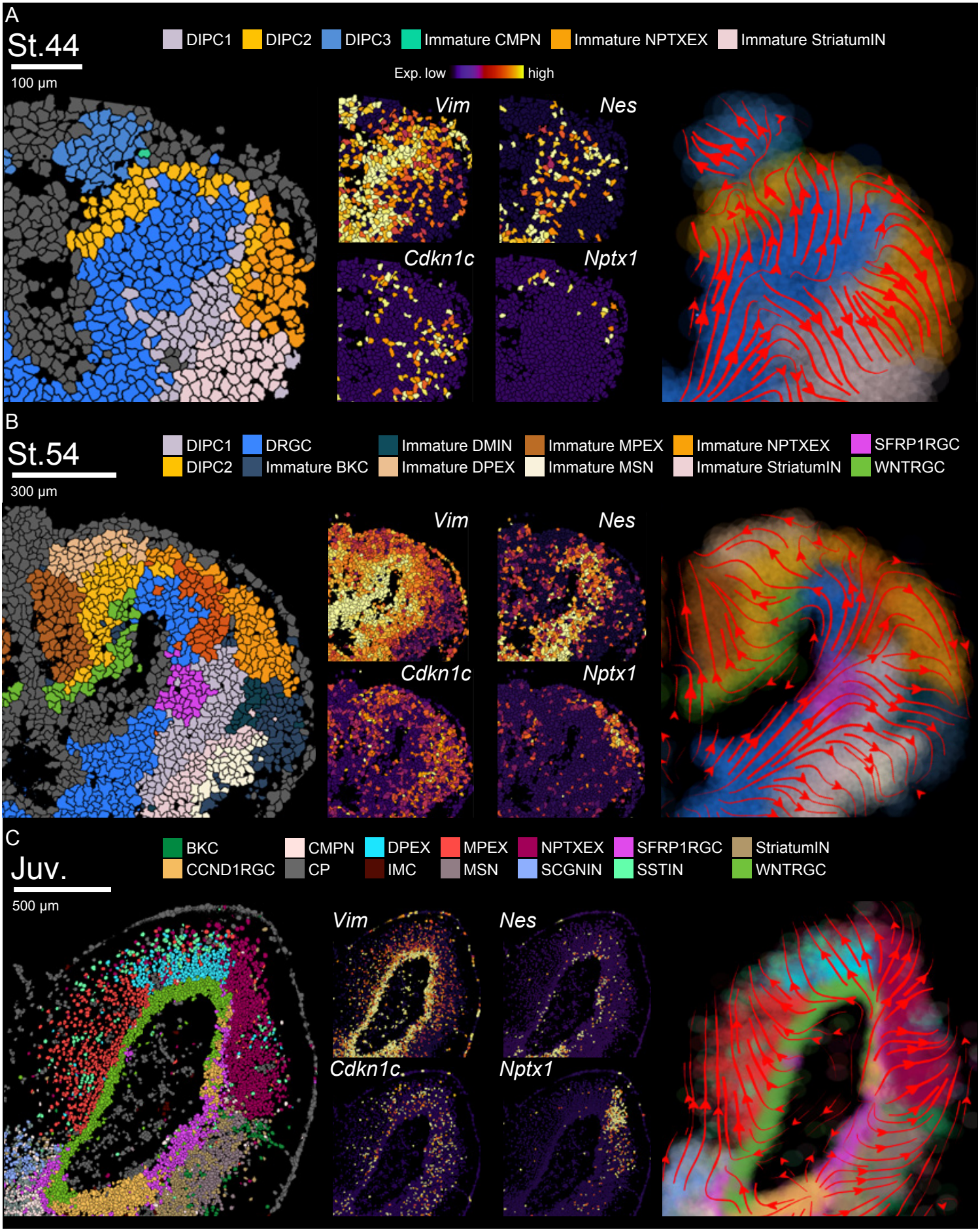
A
St.44
100 µm
DIPC1
DIPC2
DIPC3
Immature CMPN
Immature NPTXEX
Immature StriatumIN
Exp. low
high
Vim
Nes
Cdkn1c
Nptx1
B
St.54
300 µm
DIPC1
DIPC2
DRGC
Immature BKC
Immature DMIN
Immature DPEX
Immature MPEX
Immature MSN
Immature NPTXEX
Immature StriatumIN
SFRP1RGC
WNTRGC
Vim
Nes
Cdkn1c
Nptx1
C
Juv.
500 µm
BKC
CCND1RGC
CMPN
CP
DPEX
IMC
MPEX
MSN
NPTXEX
SCGNIN
SFRP1RGC
SSTIN
StriatumIN
WNTRGC
Vim
Nes
Cdkn1c.
Nptx1

Figure S29

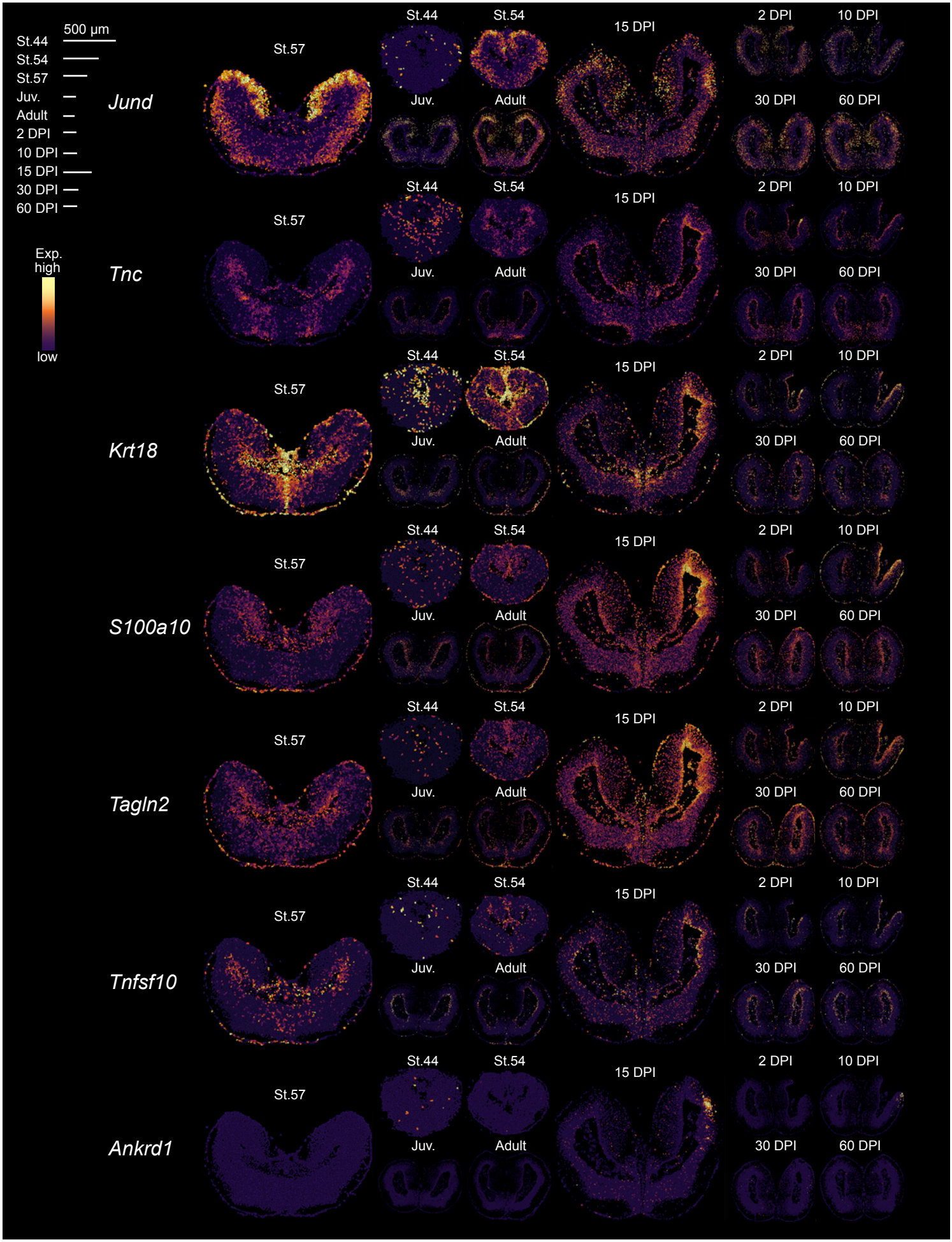
500 µm
St.44
St.54
St.57
Juv.
Adult
2 DPI
10 DPI
15 DPI
30 DPI
60 DPI
Exp.
high
low
Jund
Tnc
Krt18
S100a10
Tagln2
Tnfsf10
Ankrd1

Figure S30